

NORTHWESTERN UNIVERSITY

Towards the Precision Spectroscopy of a Single Molecular Ion

A DISSERTATION

SUBMITTED TO THE GRADUATE SCHOOL
IN PARTIAL FULFILLMENT OF THE REQUIREMENTS

for the degree

DOCTOR OF PHILOSOPHY

Field of Physics

By

Yen-Wei Lin

EVANSTON, ILLINOIS

December 2016

© Copyright by Yen-Wei Lin 2016

All Rights Reserved

ABSTRACT

Towards the Precision Spectroscopy of a Single Molecular Ion

Yen-Wei Lin

This dissertation presents some development of the single molecular ion precision spectroscopy experiment including construction of the project, spectroscopy state readout, and production of ultracold molecules. Such molecular ion spectroscopy aims at testing fundamental physics such as probing the time variation of electron-proton mass ratio.

The theories and characterization of ion traps are first discussed along with information regarding building the ion trapping systems. Then, routines in this project such as loading ions, Doppler laser cooling, excessive micromotion compensation, secular motion detection, and fluorescence imaging are deliberated.

In the state readout experiment, the coherent motion of a single trapped barium ion (Ba^+) resonantly driving by a radiation pressure is studied. By scattering of order only one hundred photons, the radiation pressure is able to seed a laser-cooled ion with a secular oscillation that is detectable by the Doppler velocimetry technique after proper

motional amplification. This seeding method provides a mapping between the ion's internal configuration and its secular motion and can be used to read out the spectroscopy results from a single non-fluorescing ion with a partially-closed cycling transition.

The work of ultracold molecule production is done with silicon monoxide ions (SiO^+), which has a strong vibration-conserved spontaneous decay branching. Therefore, by optically pumping the rotational cooling transitions in SiO^+ with a broadband radiation, the population can be efficiently driven into the ground rotational state before falling into other manifolds. To avoid the rotational heating transition, the broadband source, derived from a femtosecond pulsed laser, is spectrally filtered using an ultrashort pulse shaper.

Acknowledgements

This dissertation is a compilation of a few years of my experimental works in the laboratory and I would not be able to make most of it without many people's help.

I would like to first express my great gratitude to my advisor Prof. Brian Odom for the continuous support in all dimensions. He recruited me into his group to start building the project from scratch and coached me during the course. Prof. Odom's knowledge and techniques, research experience, and scientific perspective certainly had a strong impact on my professional development.

Helps from members of the Odom group were significant as well. People in the group have all kinds of expertise and there are a lot I can learn from them no matter how long I have been in the business.

Support from outside the group was equally important. The experience I received from Prof. Ite Yu and Prof. Jow-Tsong Shy's training and mentoring at National Tsing Hua University, Hsinchu, Taiwan quite contributed to my dissertation work in the early stage. Also, a special thank goes to Ms. Vicki Eckstein from the department's business office, who helped us deal with endless purchasing issues.

I was, fortunately, to be accompanied by my wife, Yu-Han Jao, when completing my doctoral dissertation. She has been sharing a lot of the stress coming from my work and helping me stay positive.

Finally, thanks to my wonderful parents for everything they have done for me.

Table of Contents

ABSTRACT	3
Acknowledgements	5
List of Tables	9
List of Figures	11
Chapter 1. Introduction	19
Chapter 2. Ion Trapping	24
2.1. Ion Trap Basics	24
2.2. Trap Potential Simulation	29
Chapter 3. Apparatus for the Single Ion Trap	41
3.1. The Single Ion Trap	41
3.2. Trap Electrical	48
3.3. Barium Oven	55
3.4. Laser Systems	56
3.5. Laser Stabilization	58
3.6. Fluorescence Detection	60
Chapter 4. Single Ion Experiments	63

	7
4.1. Loading an Ion	64
4.2. Laser Interaction with the Barium Ion	65
4.3. Laser Cooling	72
4.4. Photon Counting - Time Correlation	74
4.5. Micromotion compensation	77
4.6. Secular Oscillation	80
Chapter 5. Coherent Motion Single Ion State Readout	84
5.1. Motivation	84
5.2. Pulse-Driven Oscillator	85
5.3. Experimental Setup	91
5.4. Coherent Motion Amplification	93
5.5. Experiment Results	94
5.6. Spectroscopy Application	96
5.7. Error Sources and Improvement	98
5.8. Outlook	100
Chapter 6. Apparatus for the Molecular Ion Trap	102
6.1. The Molecular Ion Trap	102
6.2. Lasers	106
6.3. Fluorescence Detection	107
Chapter 7. The Molecular Ion Trap	112
7.1. Trapping Barium Ions	112
7.2. Loading SiO^+	114

7.3. Mass Spectrometry: Q-Scan	117
Chapter 8. SiO ⁺ Experiments	122
8.1. Level Structure	123
8.2. Transitions in SiO ⁺	126
8.3. Internal State Cooling	131
8.4. Relaxation and Decoherence	141
8.5. On the Horizon	147
Chapter 9. Spectral Filtering	152
9.1. Introduction	152
9.2. The Spectral Filtering Setup	155
9.3. Setup	157
9.4. Evaluation and Calibration	163
9.5. Improvement	170
References	172
Appendix A. Fluorescence from a Three-level System	180
Appendix B. Finite Element Analysis of the Trap Potential	186
Appendix C. Drawings	203

List of Tables

2.1	The visualizations and the representations of Φ_l^m for $l \leq 8$.	36
2.2	The coefficients of the multipole expansion in Eq. (2.18) with a cutoff at $l = 8$. In B1, RF electrodes in the (+x,+y) and (-x,-y) quadrants are held at 1 while all other boundaries are at zero. In B2, RF electrodes in the (-x,+y) and (+x,-y) quadrants are charged. In B3, the endcap electrodes are charged. In this simulation and analysis, the length unit is mm. Only those points within $\sqrt{x^2 + y^2} < 0.2$ mm and $ z < 0.8$ mm are included in the fitting.	39
3.1	Skin depth and AC resistance	44
4.1	Frequency response	83
5.1	Modeled contribution of various noise sources to the distribution width of the modulation amplitude, for $n_\gamma = 150$ yielding $\bar{h} = 0.20$. Data is integrated over N excitation/detection cycles, with initial ion temperature 360 μ K, $t_s = 40$ μ s, $t_a = 10$ ms, and $g_a = 2.5$. For $N = 1$, consider only the noise intrinsic to ideal single-shot excitation, say, for perfect fluorescence collection or for sustained oscillation during detection. For $N = 40$, there are 1000 fluorescence photon counts	

	spread over 20 timing bins. The last line represents the quadrature addition of all sources.	99
8.1	Spectroscopic constants of the X , A , and B state in the SiO^+	125
8.2	Decay rates of some relevant decay channels in SiO^+ . These rates were calculated in-house.	128
B.1	Fitting region $\{(x, y, z) \mid \sqrt{x^2 + y^2} < 1.5, z < 5\}$	197
B.2	Fitting region $\{(x, y, z) \mid \sqrt{x^2 + y^2} < 1.6, z < 9\}$	202

List of Figures

2.1	Trap RF electrodes configuration	25
2.2	Stability diagram	28
2.3	A sample basis function in the two dimensions.	32
2.4	The trap geometry set up for the FEM simulation. Top: input geometry. Bottom: the mesh.	34
3.1	Single ion trap outline	43
3.2	Tungsten wire electropolishing	45
3.3	Trap assembly	47
3.4	Outline of a helical resonator. (From Macalpine and Schildknecht (1959, Fig. 2))	49
3.5	Helical resonator design chart. (From (Macalpine and Schildknecht, 1959, Fig. 4))	50
3.6	The helical resonator used to drive the single ion trap.	51
3.7	RF resonant circuit with a helical resonator	52
3.8	RF voltage calibration	53
3.9	High voltage regulator	54

3.10	The DC low-pass filtering circuit. V: DC voltage supply. C: 22 μF capacitor. R: 50 $\text{k}\Omega$ resistor. EC: endcap electrode. RF-trap: nearby RF electrodes. The box indicates the filter box.	55
3.11	(a) Alumina tubing with tungsten coil as the barium oven. (b) The apertures for the oven output.	56
3.12	Drift of the wavelength meter locking mechanism.	59
3.13	Imaging optics for the single ion experiment.	61
4.1	A trapped single Ba^+ was first observed in the single ion trap at around 2pm on September 2, 2011.	63
4.2	Stability region for V_{rf} and V_{ec} .	64
4.3	Partial level diagram of Ba^+ .	66
4.4	CPT resonance observed by the laser-induced spectroscopy of Ba^+ .	71
4.5	Detect micromotion by autocorrelation.	79
4.6	Micromotion amplitude as a function of bias DC	80
4.7	Tickling on end cap	81
4.8	Autocorrelation function of the oscillating ion.	82
5.1	Modeled response of the Ba^+ oscillator to a pulsed drive with 10% duty cycle (gray band), with realistic drive parameter $\eta = 2.67 \text{ nm}$, and initial conditions $\phi_0 = -122^\circ$ and $A_0 = 34 \text{ nm}$ ($V_0 = 0.2 \text{ m/s}$), typical of Doppler cooling. Results from the simulation (points)	

	deviate from the model of Eq. (5.20) (lines) because of noise in photon scattering.	91
5.2	Experimental timing sequence.	92
5.3	Fluorescence modulation. (a) The ion is bright to the seeding laser. (b) The ion is dark to the seeding laser.	94
5.4	Measured modulation amplitude mean (points) and standard deviation (bars) versus seeding duty cycle, with seeding time varied to maintain $D \times t_s = 4 \mu\text{s}$; data were collected over 30 trials. Averaging Eq. (5.20) over initial phases and fitting for amplification-stage gain yields the solid curve.	95
5.5	Modulation amplitude versus seeding time, when the seeding pulses excite an S-state ion (red), and when the ion is shelved in the D-state (blue). Each point is the average of 30 measurements, with the vertical bars showing the distribution standard deviation (rather than the error on the mean). The predicted response (black curve) is from Eq. (5.20), fitting for amplification-stage gain.	96
5.6	Distribution of the modulation amplitudes, measured after seeding the motion for $40 \mu\text{s}$ (red histogram) and for an unseeded ion (blue histogram). The simulation (solid curves) accounts for noise in ion dynamics and shot noise in detection. Amplification gain is the single fit parameter.	97

5.7	Determination of modulation index from data with 30 average counts per bin.	98
6.1	Molecular ion trap outline	103
6.2	RF source with toroidal inductor.	104
6.3	Imaging system for the molecular ion trap. (1) Single ion source, N.A. = 0.22. (2) Vacuum viewport; fused silica, about 10 mm thick. (3) f=100 mm achromatic doublet. (4) f=200 mm achromatic doublet. (5) f=50 mm achromatic doublet. (6) Dichroic mirror transmits 493 nm and reflects 385 nm. (7)(8) f=125 mm achromatic doublet.	108
6.4	TRA of imaging system	110
6.5	Some images of ions with optical aberration	111
6.6	Efficiency vs ROI size	111
7.1	laser cooled barium ions	114
7.2	The mass spectrometry of the ablation product on RGA.	115
7.3	Potential energy curves in the neutral SiO. From Oddershede and Elander (1976).	117
7.4	SiO REMPI spectrum.	118
7.5	SiO ⁺ dark core.	118
7.6	Stability region and the q-scan.	119
7.7	trap and cem	121
7.8	The q-scan data	121

		15
8.1	Potential energy curves of SiO ⁺ .	125
8.2	reference spectroscopy signal	131
8.3	SiO ⁺ laser-induced fluorescence spectrum in $X-B, (00)$.	132
8.4	Population distribution in the rotational states of SiO ⁺ at 300 K (green) and 1000 K (magenta). The P-branch (purple) and R-branch (blue) rotational transitions in the $B-X, (00)$ band are shown as well.	133
8.5	Rotational cooling illustrated.	134
8.6	Vibrational repumping	137
8.7	Data of cooling AlH ⁺ . Figure reproduced from Lien <i>et al.</i> (2014). Dark red: AlH ⁺ 's rotational levels are thermally populated up to $N = 7$ at the room temperature. Green: Cooling on the P-branch but the P(1) transition results in population in the $N=0$ and $N=1$. Blue: Further driving the P(1) transition causes the parity flipping via the relaxation through $X, v=1$ and put the population completely in $N=0$.	140
8.8	Relaxation time due to the spontaneous decay and the BBR-induced transition.	144
8.9	Zeeman effect	147
8.10	SiO ⁺ dissociation cross-sections from $B^2\Sigma$ to $(2)^2\Pi$ and $(3)^2\Sigma$.	150
9.1	Rotational cooling with spectral-filtered broadband source. In this example, relevant transitions from $A^2\Pi_{1/2}, v'=0 \leftarrow X^2\Sigma_{1/2}, v''=0$ band in the AlH ⁺ are shown as vertical bars at the bottom. P-branch	

is the rotational cooling transitions, while Q- and R-branch are the opposite. An unfiltered UV femtosecond laser (spectrum shown as dashed line) drives all transitions thus provides no cooling effect. A filtered source (spectrum shown as solid line) drives only cooling transitions and hence slows down the molecule's rotation. 153

9.2 Schematic of our spectral filtering setup. fs-laser: mode-locked femtosecond laser; WP: half-wave plate; XTAL: BBO SHG crystal; L1-4: lens; M1-3: mirrors (M3 is concave). G1 and G2 are reflective diffraction gratings; C: fiber coupler. See text for detailed discussion. 156

9.3 Microscope images of three samples of razor blades used in this experiment. While we image the blades (gray area) in front of a dark background, the boundary between two areas is due to the blade edge. It is easy to see the fuzziness of the blade edge is around $1\ \mu\text{m}$, smaller than the focal spot size ($\sim 10\ \mu\text{m}$) in our setup. 160

9.4 Some possible scenarios regarding dispersion in the 4-f line. The red and the blue lines represent the propagation path of two different spectral components. (a) is an ideal case where the input beam is dispersion-free and $G1=G2$ and $L2=L3$. In (b), the alignment of some components is off, and hence the output beam derives dispersion. In general, as in (c), the source of dispersion can come from the input beam and errors from components and alignment. However, dispersion can be compensated by properly aligning the location and the diffraction angle of the grating G2. 162

- 9.5 Schematic of our spectrometer. C: fiber output coupler; L5-6: collimation lens; G3: diffraction grating; L7: focusing lens; CCD: linear camera. 164
- 9.6 Intensity profile on the focusing plane of a narrowband laser, recorded by a line camera. A large input beam size $w_i = 12.1$ mm is used in the right panel, and causes the focal spot to be less compact. While in the left, a permissible beam size $w_i = 6.8$ mm is used, and the focal spot profile is fairly close to Gaussian. 165
- 9.7 (a) Consistency of spectrometer resolution over its measurement range. In this test, we simulate different narrowband laser wavelengths by rotating the grating, as if the diffraction angle is changed due to another wavelength. (b) Spot profiles for data #1 (left-most), #5 (middle), and #9 (right-most) from the data sequence in (a). The horizontal axis is the pixel number on the linear camera. The spots in the upper row are focused by the doublet lens and those in the bottom row are focused by the singlet lens. The width of each plot is 30 pixels. 167
- 9.8 Spectrum of the original and filtered light. 169
- 9.9 Cutoff resolution versus mask longitudinal position. 169
- 9.10 cutoff resolution versus different cutoff frequency. 170

A.1	(Upper plot) F_c versus laser intensity Ω_c/Γ_c . (Lower plot) Excitation state population versus laser intensity Ω_c/Γ_c . $\Delta_b = 0$ and $\Delta_c = 0$ in both plots.	183
C.1	Macro stand for RF electrodes - sheet 1	204
C.2	Macro stand - sheet 2	205
C.3	Macro stand for endcap electrodes	206
C.4	Trap base plate	207
C.5	Single ion trap assembly - sheet 1	208
C.6	Single ion trap assembly - sheet 2	209
C.7	Single ion trap assembly - sheet 3	210
C.8	Single ion trap assembly - sheet 4	211
C.9	Trap stand	212
C.10	6CF flange	213
C.11	Doubler - sheet 1	214
C.12	Doubler - sheet 2	215
C.13	Doubler - sheet 3	216
C.14	Doubler - sheet 4	217
C.15	Cover for the doubler	218
C.16	Crystal holder	219

CHAPTER 1

Introduction

Ultracold molecule is the new frontier in many fields. In the researches of quantum information processing, the interaction between quantum bits can be realized by the large dipole moment from the molecules. With the ability of quantum control of atoms and molecules, chemistry can be studied with specific initial states in contrast to the thermal population distribution. Molecules also provide additional advantages for spectroscopy experiments of searching the permanent dipole moment and other testings of the fundamental physics, which is one of the focus in this research group.

Proton-to-Electron Mass Ratio

The proton-to-electron mass ratio $m_p/m_e \equiv \mu$ is one of the fundamental constants that describes the structure of matters. Its current value is 1836.152 673 771(7) (Sturm *et al.*, 2014). Theories of time-varying proton-to-electron mass ratio involve physics beyond the Standard Model, which were reviewed in, e.g., Uzan (2011); Ubachs *et al.* (2016). Here, I only briefly summarize from the experimental aspect.

The drift of μ can be probed by measuring the change of transition frequency in an atomic or a molecular system. However, only the drift of a dimensionless quantity can be reliably used to infer a time variation. Hence, to find the drift of μ , one must compare the change among different transitions.

In the atomic system, the dependence on μ shows up in the transition between two hyperfine states along with the fine structure constant α . However, hyperfine transitions also have state-dependent components such that the ratio between two hyperfine transitions is not solely a function of μ . The determination of these other factors heavily relies on the theories. Therefore, the time variation of μ measured in an atomic system is oftentimes strongly model-dependent. The measurement is, however, model-independent in a molecular transition as the ratio between rotational or vibrational transitions has a pure dependence on the mass ratio: $\mu^{-1/2}$ for the vibrational transitions and μ^{-1} for the rotational transitions (Flambaum and Tedesco, 2006). Thus, probing a drifting μ in a molecular system is an advantage.

The major approach for measuring μ'/μ is by the astronomical observations. In some measurements where the emission of H_2 from the early Universe is compared to the laboratory spectroscopy results. $|\delta\mu/\mu|$ is bounded by 5×10^{-6} over the 10^{10} -year timespan, or $|\mu'/\mu| < 10^{-16}$ per year, according to those measurements (see Ubachs *et al.* (2016) for an overview). Yet, probing such tiny variation within a much shorter timeframe by a tabletop experiment has recently become feasible due to the development of high precision atomic clock. For example, a Yb^+ clock experiment has constrained the fractional variation to be less than $10^{-16}/\text{yr}$ as well (Godun *et al.*, 2014). In a different experiment, Shelkownikov *et al.* (2008) performed precision spectroscopy with SF_6 molecular beam and obtained $10^{-14}/\text{yr}$ fractional drift, which is one of the first measurements in a molecular system. The measurement sensitivity will be advanced once we applied the precision ion clock technique to a molecular ion.

Precision Spectroscopy

Single ion precision spectroscopy is the primary goal of our laboratory. We choose to work with ionic species for the extreme long holding time in an ion trap. Besides, minimization of the systematic errors is much easier for a localized single ion, which makes the coherence time much longer than that of a cloud.

One of the challenges in the single ion spectroscopy is collecting the signal. Precision laser spectroscopy usually involves detecting the fluorescence, which is an efficient and least destructive state readout approach. However, most of the molecular species do not have a closed transitions to generate a strong fluorescence signal. This obstacle can be overcome by co-trapping the spectroscopy species with an additional ion, often called the logic ion, that has good cycling transitions. Through their mutual Coulomb interaction, the two ions share the common motional modes. First of all, the motion of the spectroscopic ion can be therefore cooled by laser cooling the logic ion, known as the sympathetic cooling. Furthermore, by driving transitions that couples the internal state of the spectroscopic ion and the motional mode, the information of the internal degree of freedom is mapped to the logic ion, which can be probed easily.

High precision single ion spectroscopy utilizing this scheme has been demonstrated in Schmidt *et al.* (2005); Rosenband *et al.* (2008); Chou *et al.* (2010), for instance. In these experiments, the spectroscopy of a single Al^+ displayed a 10^{-18} fractional uncertainty. If the technology can be applied to the molecular ion spectroscopy to reach a similar or better performance, this tabletop spectroscopy experiment will be able to perform some of the stringent tests of the fundamental physics.

Cooling of Molecules

Another key towards the precision spectroscopy is to prepare the sample into a single quantum state. Getting an atomic species into a single state by optical pumping is usually easy due to the simple structure. However, optical pumping of a molecule is quite trickier due to the additional vibrational and rotational degrees of freedom. First, the molecule often populates multiple states originally and thus all those states need to be addressed in the cooling scheme. Additionally, there is usually no specific selection rules governing the vibrational transitions and thus population could easily gain extra randomness during the spontaneous decay which is part of the essential process during the optical pumping. That is, a compact closed transition system for efficient internal state cooling does not always exist in a molecule.

In this work as well as our laboratory, we have been working with diatomic molecular ions which have fairly diagonal vibrational transitions. Explicitly, these molecules preserve their vibrational quantum state during spontaneous decays for most of the time. While this dissertation considers the silicon monoxide ion, or SiO^+ , the aluminum monohydride ion, or AlH^+ , is yet another species we have been investigating. We have developed efficient, all-optical cooling scheme for these molecules by using a broadband radiation to pump the population into the ground state.

Structure of this Dissertation

The molecular ion precision spectroscopy experiment is a giant project. Ingredients of a typical spectroscopy experiment include source production, trapping and cooling the translational, motion, internal state initiation, spectroscopy excitation, and spectroscopy state readout. My work has been focused on building the hardware, the manipulation of

a single ion for the state readout, and the control of the molecular ion's internal states. This dissertation presents some of the early-stage development towards this goal and is structured mainly into two parts: the single ion project and the molecular ion project.

In Chapter 2, I briefly review the ion trapping fundamentals as well as the properties of linear Paul traps. Additionally, modeling of the trap electric field by the finite element method is present in Section 2.2.

The single ion project is covered in Chapters 3 to 5. The goal of this single ion experiment is to develop a spectroscopy state readout method. The experimental hardware including the trap, the vacuum, the lasers, etc. are described in Chapter 3. In Chapter 4, I discuss the routines in this experiment such as loading and cooling of a single barium ion. The motional state readout approach is explored in Chapter 5.

The molecular ion project is covered in Chapters 6 to 9. While the experimental system is different from the one used in the single ion experiment, Chapter 6 augments to Chapter 3 with information specific to apparatus for this project. Chapter 7 discusses the general practice of working with SiO^+ , which is one of the perspective molecular ions for our spectroscopy experiment. This molecular ion is introduced in Chapter 8.

Also in Chapter 8, I present the scheme for cooling the internal degrees of freedom in SiO^+ in detail. Other properties regarding the dynamics of the molecule's internal state are discussed in this chapter too. The setup of spectral filtering, the key technique of our rotational cooling method, is investigated in Chapter 9.

CHAPTER 2

Ion Trapping

Trapping charged particles is relatively easy as there exists the strong interaction between the particles and an electric field. In my experiment as well as the whole laboratory, we trap several ionic species (barium, silicon monoxide, aluminum hydride, etc.) in radio frequency Paul traps. The theories of ion trapping can be found in many references and I would point the readers to, for instance, Ghosh (1995) and Wineland *et al.* (1997) for comprehensive discussions of the ion trapping technology. I will first briefly summarize the theory and some properties of a linear Paul trap. In the second half of this chapter, I will introduce trap potential simulation with by finite element method.

2.1. Ion Trap Basics

A linear Paul trap is a derivative of a quadrupole mass filter with additional end-cap electrodes to provide three-dimensional confinement of charged particles. The radial trapping field is usually produced by four elongated electrodes surrounding the trapping region. Figure 2.1(a) shows a typical infinite Paul trap configuration where the electrodes have hyperbolic cross-sections and the distance from the trap center to each vertex is r_0 . One pair of the electrodes is held at $V_0/2$ while the other pair is at $-V_0/2$. The electric potential $V(x, y, z)$ generated by this configuration is

$$V(x, y, z) = \frac{V_0}{2} \left(\frac{x^2 - y^2}{r_0^2} \right). \quad (2.1)$$

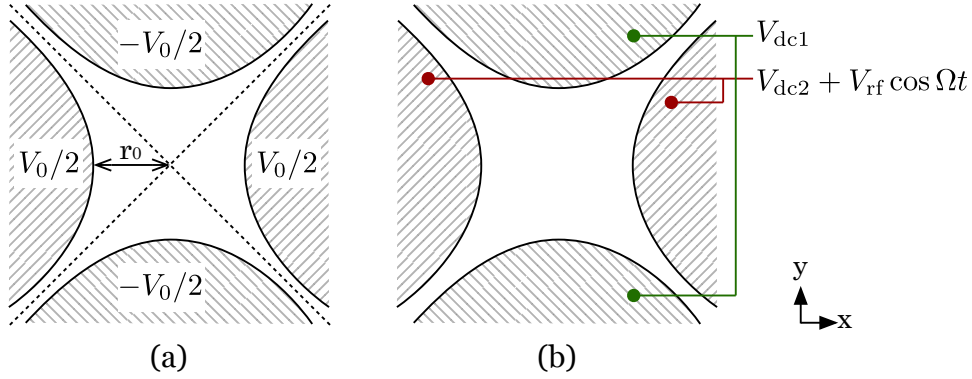


Figure 2.1. Trap RF electrodes configuration

For a positive charge particle, the above potential is trapping in the x-direction but anti-trapping in the y direction, which results in an unstable stationary line along $z = 0$ where $\nabla V = \vec{E} = 0$. The electric potential cannot have any stable stationary point in free space as it obeys the Laplace equation. The stationary point can be made stable when one alternates the field polarity at an adequate frequency. Namely

$$V(x, y, z, t) = \frac{V_0 \cos \Omega t}{2} \left(\frac{x^2 - y^2}{r_0^2} \right)$$

is mechanically stable near $z = 0$ for properly chosen voltage amplitude V_0 and oscillating frequency Ω . The parameter space of the AC field for stable trapping will be discussed shortly. In practice, for trapping atomic or light molecular ions, the frequency of the AC field falls into the radio frequency band while voltage up to 1000 V can be generated by a fairly simple circuitry.

Figure 2.1(b) shows the configuration commonly used in the lab where only one pair of the electrodes is driven with the RF voltage V_{rf} . In addition, each pair of the electrodes can be biased at a DC voltage V_{dc1} and V_{dc2} . From Eq. (2.1) it is straightforward to find

the potential for this setup being

$$\begin{aligned} V_r &= \frac{V_{\text{dc1}}}{2} \left(1 - \frac{x^2 - y^2}{r_0^2} \right) + \frac{V_{\text{dc2}} + V_{\text{rf}} \cos \Omega t}{2} \left(1 + \frac{x^2 - y^2}{r_0^2} \right) \\ &= \frac{V_{\text{dc}} + V_{\text{rf}} \cos \Omega t}{2} \left(\frac{x^2 - y^2}{r_0^2} \right) + V_0 \end{aligned} \quad (2.2)$$

where $V_{\text{dc}} = V_{\text{dc2}} - V_{\text{dc1}}$ and $V_0 = (V_{\text{dc1}} + V_{\text{dc2}} + V_{\text{rf}} \cos \Omega t)/2$. It is worth pointing out that a none zero V_{dc} is necessary to break the degeneracy of radial motion.

The four-electrode setup does not confine particle axially. The axial, z-directional, confinement is achieved by adding a pair of endcap electrodes to cap both ends of the Paul trap. The endcaps produce the following potential:

$$V_z = V_{\text{ec}} \left(\frac{2z^2 - x^2 - y^2}{4z_0^2} \right) \quad (2.3)$$

when the endcaps are separated by $2z_0$ and supplied at V_{ec} .

The total potential of the trap is the sum of the fields due to all electrodes:

$$V = V_r + V_z = V_0 + V_x x^2 + V_y y^2 + V_z z^2 \quad (2.4a)$$

where

$$V_x = - \left(\frac{V_{\text{ec}}}{4z_0^2} - \frac{V_{\text{dc}}}{2r_0^2} \right) + \frac{V_{\text{rf}}}{2r_0^2} \cos \Omega t \quad (2.4b)$$

$$V_y = - \left(\frac{V_{\text{ec}}}{4z_0^2} + \frac{V_{\text{dc}}}{2r_0^2} \right) - \frac{V_{\text{rf}}}{2r_0^2} \cos \Omega t \quad (2.4c)$$

$$V_z = \frac{V_{\text{ec}}}{2z_0^2}. \quad (2.4d)$$

Note that Eq. (2.4) is only an approximation because V_r and V_z fulfill different boundary conditions (as different electrodes are considered). In principle, one should solve the Laplace equation with complete boundary conditions to obtain the total trapping field. Numerical simulation of the trapping field will be discussed in the next section and Appendix B.

Mathieu Equation

The motion of a particle of mass m and charge e in an electric field is governed by $m\ddot{\vec{r}} = e\vec{E}(\vec{r}) = -e\nabla V(\vec{r})$. With the potential in Eq. (2.4), the equation of motion in each direction is a Mathieu differential equation:

$$\frac{d^2x}{d\zeta^2} + (a_x - 2q_x \cos 2\zeta)x = 0 \quad (2.5a)$$

$$\frac{d^2y}{d\zeta^2} + (a_y - 2q_y \cos 2\zeta)y = 0 \quad (2.5b)$$

$$\frac{d^2z}{d\zeta^2} + (a_z - 2q_z \cos 2\zeta)z = 0 \quad (2.5c)$$

with $\zeta = \Omega t/2$ being the canonical time and

$$a_x = -\frac{2eV_{\text{ec}}}{mz_0^2\Omega^2} + \frac{4eV_{\text{dc}}}{mr_0^2\Omega^2}, \quad q_x = -\frac{2eV_{\text{rf}}}{mr_0^2\Omega^2}, \quad (2.6a)$$

$$a_y = -\frac{2eV_{\text{ec}}}{mz_0^2\Omega^2} - \frac{4eV_{\text{dc}}}{mr_0^2\Omega^2}, \quad q_y = \frac{2eV_{\text{rf}}}{mr_0^2\Omega^2}, \quad (2.6b)$$

$$a_z = \frac{4eV_{\text{ec}}}{mz_0^2\Omega^2}, \quad q_z = 0. \quad (2.6c)$$

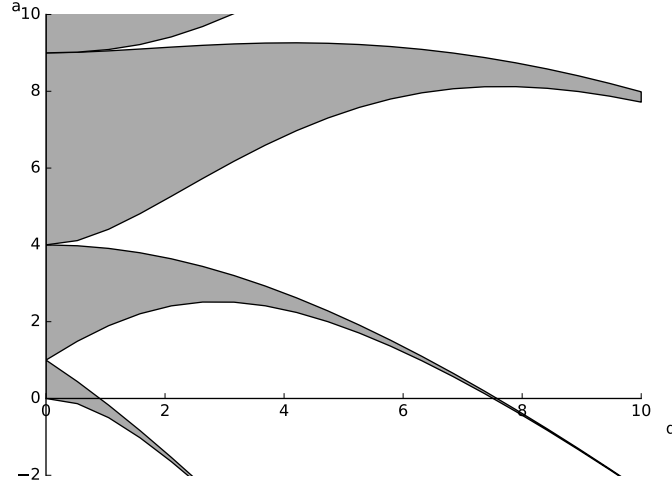


Figure 2.2. Stability diagram

Stability for One Ion

The Mathieu equation has either stable or unstable trajectories depending on the values of the a and q parameters. Figure 2.2 shows the region where (a, q) exhibits stable trajectories. Although there are multiple stable regions, usually an ion trap is operated in the first stable region with $a < q^2 \ll 1$.

The trap must be stable in all directions in order to trap an ion. Therefore, for a given species, one must pick the RF voltage and frequency and the DC voltages carefully to have the (a, q) pairs in the x, y, and z directions all falling into stable regions.

Motion of a Single Ion

In the z direction where $q = 0$ and $a > 0$, the trapped ion is a harmonic oscillator

$$z(t) = A_z \cos(\omega_z t + \phi_z) \quad (2.7)$$

where

$$\omega_z = \sqrt{a_z} \frac{\Omega}{2} = \sqrt{\frac{eV_{ec}}{mz_0^2}} \quad (2.8)$$

and A_z and ϕ_z are constants determined by the initial conditions.

For small, nonzero q , as in the radial direction, the solution to the Mathieu equation is approximately

$$u(t) = A \cos(\omega t + \phi) \times \left(1 - \frac{q}{2} \cos \Omega t\right). \quad (2.9)$$

In the above equation, the $\cos \omega t$ term represents the secular oscillation at frequency

$$\omega = \sqrt{a + \frac{q^2}{2}} \times \frac{\Omega}{2} \quad (2.10)$$

while the $\cos \Omega t$ term represents the so-called micromotion, which is the driven oscillation due to the RF electric field. The micromotion amplitude is proportional to the secular amplitude, and therefore, micromotion is vanished only if an ion has no secular motion.

In other words, micromotion always presents in thermal ions.

2.2. Trap Potential Simulation

A real life ion trap has complex geometry and thus would not produce an electric potential as simple as Eqs. (2.1) and (2.3). Therefore, to understand the field provided a practical trap, simulation is required. A common way to analyze an ion trap is by simulating the dynamics of charged particles in the trap. For example, Tabor *et al.* (2012) used SIMION to compute the ion trajectories in the traps and then extracted some trap characteristics. On the other hand, the trap can be investigated by directly solving the electric field according to the configuration.

The electric potential V of an ion trap is obtained by solving the Laplace's equation

$$\nabla^2 V(\vec{r}, t) = 0 \quad (2.11)$$

with proper boundary conditions. The potential is time dependent since we are running a radio frequency trap. However, the frequency is low enough such that the corresponding propagation distance is much greater than the characteristic trap size; in other words, we do not have to consider field retardation in an ion trap such that we can safely formulate the problem as solving electrostatic potential. Assuming there are n boundaries $\Gamma = \Gamma_1 \dots \Gamma_n$ (electrodes and all other conductors) in the trap, the potential can be written as

$$V(\vec{r}, t) = \sum_{i=1}^n \epsilon_i V_i(\vec{r}) \quad (2.12)$$

where ϵ_i is the voltage supplied to each boundary i and can be either static or varying at the radio frequency; V_i is the solution of the Laplace's equation with boundary i held at unity and zero for all others:

$$\nabla^2 V_i(\vec{r}) = 0 \quad (2.13a)$$

$$V_i(\vec{r}) = 1, \vec{r} \in \Gamma_i \quad (2.13b)$$

$$V_i(\vec{r}) = 0, \vec{r} \in \Gamma - \Gamma_i. \quad (2.13c)$$

I obtained the numerical solutions of each V_i by the finite element method (FEM). There are other numerical approaches developed exactly for the above problem, but the discussion and comparison of other methods are beyond the scope of this work. Here, I just point out that finite element method is more able to handle complex geometry than other

approaches such as finite difference. Besides, there are some open source FEM packages available, which makes this task more accessible.

Short Introduction to FEM

Regardless the mathematical framework, the idea of the finite element method is actually simple. The physical domain of the problem is first discretized into smaller regions, usually tetrahedrals in the three dimensions and triangles in the two dimensions. Then we can construct a basis function set $\{\phi_i\}$ over the domain. Among many fancy choices, the basis function can simply be a piecewise linear function where it has unity value on one vertex and zero elsewhere. These basis functions are called elements. Figure 2.3 shows an example of the basis function in two dimensions. Any function f defined over the domain can be approximated by

$$f(\vec{r}) = \sum_i c_i \phi_i(\vec{r}) \quad (2.14)$$

where c_i are coefficients that solve the Laplace equation $\nabla^2 f = 0$. In the finite element method, the differential equations are solved in their weak form, i.e., if f is the solution, then

$$\int (\nabla^2 f) g \, d\vec{r} = 0 \quad (2.15)$$

or

$$\int \nabla f \cdot \nabla g \, d\vec{r} = 0 \quad (2.16)$$

must be true for any test function g . From Eq. (2.15) to Eq. (2.16), I have applied the rule of integration by parts. The required number of test functions g to completely define the differential equation in its weak form is exactly equal to the number of coefficients c_i to be determined; that is the number of elements as well. Therefore, a natural choice of a

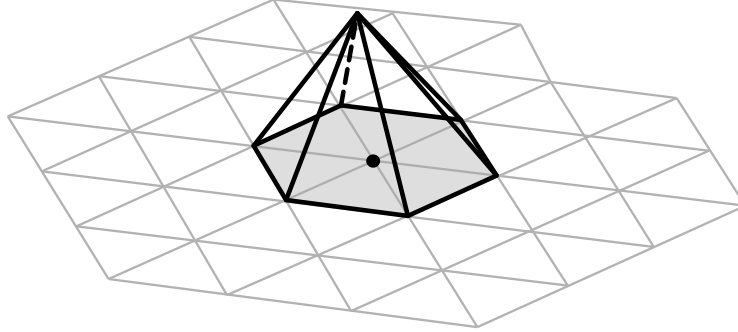


Figure 2.3. A sample basis function in the two dimensions.

set of g is the basis function set $\{\phi_i\}$. For each $g = \phi_j$, Eq. (2.16) yields a linear equation of $\{c_i\}$:

$$\sum_i c_i \int \nabla \phi_i \cdot \nabla \phi_j d\vec{r} = 0 \quad (2.17)$$

as each $\int \nabla \phi_i \cdot \nabla \phi_j d\vec{r} \equiv \langle \nabla \phi_i, \nabla \phi_j \rangle$ pair can be evaluated beforehand. Note that some of the c_i in each linear equation are pre-determined by the boundary conditions and therefore the number of unknown variables are reduced. Finally, the Laplace equation is formulated into a large system of linear equations. It is worth pointing out that, as ϕ_i is compact, $\langle \nabla \phi_i, \nabla \phi_j \rangle$ is zero when i is far from j , and therefore the linear system is sparse. There are many numerical methods for solving sparse linear systems in quick and accurate ways, which makes finite element analysis powerful for a large domain size. Here, I however will not discuss the actual numerical schemes used in my simulation since it is beyond the scope of this thesis.

Implementation

In my work, the discretization of the trap geometry was done with Gmsh (v2.12), and the finite element analysis was done with Freefem++ (v3.42). One should refer to

the manuals for software usage, but the scripts for this work will be provided later in Appendix B.

Here I present the simulation result for the single ion trap as an example. The full design of the trap will be described in Section 3.1, but in the simulation, it is simplified to four long rods for the RF and two short pins for end caps. The setup is enclosed in a cylindrical grounding can for the computational purpose. The size of the enclosure should be large enough so its boundary effect does not significantly alter the simulation result in the trap region. The upper two drawings in Fig. 2.4 show the configuration rendered in Gmsh viewing along the z- and the x-axis; so are the bottom two, with the surfaces of the electrodes meshed. In this example, the free space region for the electric potential is split into 7.6×10^5 tetrahedrons, and all the surfaces of the electrodes are discretized into 9.7×10^4 triangles. This mesh ensemble is formed by 1.4×10^5 vertices, which are the variables for solving the Laplace equation.

After the trap geometry has been meshed, I used Freefem++ to solve the Laplace equation. As mentioned earlier, the solver is invoked several times for various boundary conditions settings. In this example, boundaries are divided into four groups: (1) one diagonal pair of the RF rods, (2) the other diagonal pair of the RF rods, (3) the endcap electrodes, and (4) the grounding cylinder. Solutions to the cases where (1), (2), and (3) each being held at unity voltage were computed. With these simulation results, the electric potential produced by this trap can be reconstructed with the basis function set.

Post-processing

Because the domain can not be discretized based on a regular grid, the simulation result is in fact a list of scattered data points. To better understand the result, the

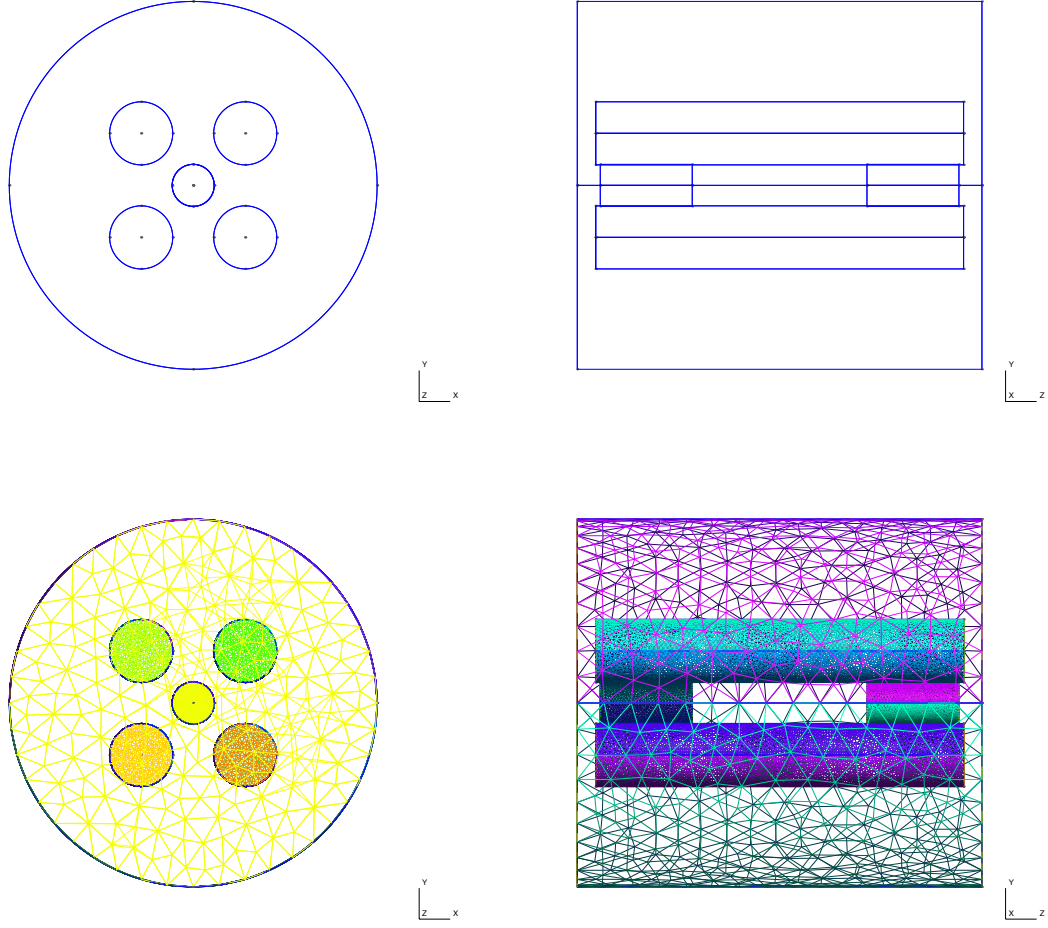


Figure 2.4. The trap geometry set up for the FEM simulation. Top: input geometry. Bottom: the mesh.

multipole expansion is applied to the simulated field:

$$\begin{aligned}
 V(\vec{r}) = V(r, \theta, \phi) &= \sum_l \sum_m C_{lm} \Phi_l^m(r, \theta, \phi) \\
 &= \sum_l \sum_m C_{lm} r^l P_l^m(\cos \theta) \times \begin{cases} \cos(m\phi) & \text{for } m \geq 0 \\ \sin(m\phi) & \text{for } m < 0 \end{cases}
 \end{aligned} \tag{2.18}$$

where P_l^m is the associated Legendre polynomial, commonly used in solving the Laplace equation with a cylindrical symmetry. Note that in the above expansion, all the odd l and odd m terms are automatically dropped due to additional symmetry set by the boundary conditions. In contrast, one should include all terms if no specific symmetry condition exists.

The lowest order ($l = 0$ and $m = 0$) in the expansion represents a constant potential.

There are three terms for $l = 2$:

$$\Phi_2^0 = r^2 P_2^0(\cos \theta) = \frac{1}{2}(3 \cos^2 \theta - 1) = \frac{1}{2}(-x^2 - y^2 + 2z^2) \quad \text{for } m = 0, \quad (2.19a)$$

$$\Phi_2^2 = r^2 P_2^2(\cos \theta) \cos(2\phi) = 3(\cos^2 \theta - 1) \cos(2\phi) = 3(x^2 - y^2) \quad \text{for } m = 2, \quad (2.19b)$$

and

$$\Phi_2^{-2} = r^2 P_2^{-2}(\cos \theta) \sin(-2\phi) = \frac{-1}{8}(\cos^2 \theta - 1) \sin(2\phi) = \frac{1}{4}xy \quad \text{for } m = -2. \quad (2.19c)$$

These potential forms represent the three mutually different quadratic fields. In fact, Eq. (2.19a) is the lowest order harmonic potential from the end caps. Equation (2.19b) is the potential for ideal the infinit linear quadruple Paul trap; so is Eq. (2.19c) but with the trap rotated by 45 degrees. Refer to previous section. See Table 2.1 for the visualization of the potential fields in Eq. (2.19) as well as those up to $l = 8$.

Table 2.1. The visualizations and the representations of Φ_l^m for $l \leq 8$.

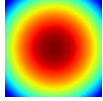
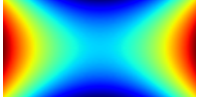
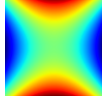
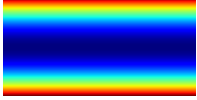
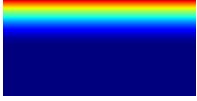
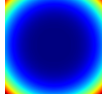
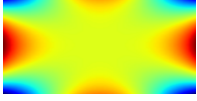
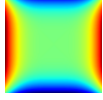
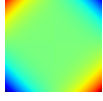
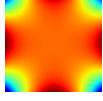
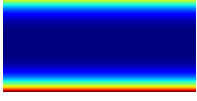
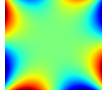
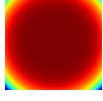
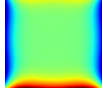
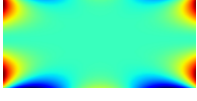
l	m	xy ($z = 0$)	xz ($y = 0$)	Φ_l^m
0	0			1
2	0			$\frac{1}{2}(-x^2 - y^2 + 2z^2)$
2	2			$3(x^2 - y^2)$
2	-2			$\frac{1}{4}xy$
4	0			$\frac{1}{8}(3r^4 - 30r^2z^2 + 35z^4)$
4	2			$-\frac{5}{2}(r^2 - 7z^2) \times \Phi_2^2$
4	-2			$\frac{1}{6}(7z^2 - r^2) \times \Phi_2^{-2}$
4	4			$105(x^4 - 6x^2y^2 + y^4)$
4	-4			$\frac{1}{96}xy(y^2 - x^2)$
6	0			$\frac{1}{16}(-5r^6 + 105r^4z^2 - 315r^2z^4 + 231z^6)$
6	2			$\frac{35}{8}(r^4 - 18r^2z^2 + 33z^4) \times \Phi_2^2$

Table 2.1 (continued)

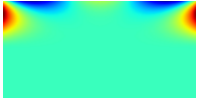
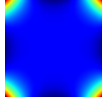
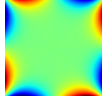
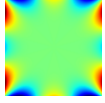
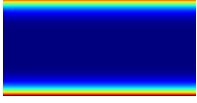
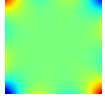
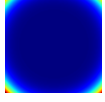
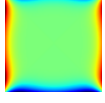
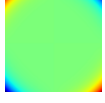
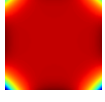
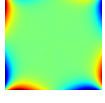
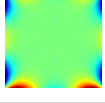
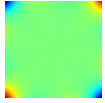
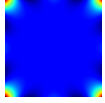
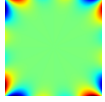
l	m	xy ($z = 0$)	xz ($y = 0$)	Φ_l^m
6	-2			$\frac{1}{16} (r^4 - 18r^2z^2 + 33z^4) \times \Phi_2^{-2}$
6	4			$-\frac{9}{2} (r^2 - 11z^2) \times \Phi_4^4$
6	-4			$\frac{1}{10} (11z^2 - r^2) \times \Phi_4^{-4}$
6	6			$10395 (x^6 - 15x^4y^2 + 15x^2y^4 - y^6)$
6	-6			$\frac{1}{23040} (-3x^5y + 10x^3y^3 - 3xy^5)$
8	0			$\frac{1}{128} (35r^8 - 1260r^6z^2 + 6930r^4z^4 - 12012r^2z^6 + 6435z^8)$
8	2			$-\frac{105}{16} (r^6 - 33r^4z^2 + 143r^2z^4 - 143z^6) \times \Phi_2^2$
8	-2			$\frac{1}{32} (-r^6 + 33r^4z^2 - 143r^2z^4 + 143z^6) \times \Phi_2^{-2}$
8	4			$\frac{99}{8} (r^4 - 26r^2z^2 + 65z^4) \times \Phi_4^4$
8	-4			$\frac{1}{40} (r^4 - 26r^2z^2 + 65z^4) \times \Phi_4^{-4}$
8	6			$-\frac{13}{2} (r^2 - 15z^2) \times \Phi_6^6$

Table 2.1 (continued)

l	m	xy ($z = 0$)	xz ($y = 0$)	Φ_l^m
8	-6			$\frac{1}{14} (15z^2 - r^2) \times \Phi_6^{-6}$
8	8			$2027025 (x^8 - 28x^6y^2 + 70x^4y^4 - 28x^2y^6 + y^8)$
8	-8			$\frac{1}{1290240} (-x^7y + 7x^5y^3 - 7x^3y^5 + xy^7)$

The expansion coefficients are obtained by fitting the simulation data to Eq. (2.18) with a cutoff l_{max} . Because the nature of this expansion is a linear combination of orthogonal functions, the least square fitting will work nicely. Refer to Appendix B for the python implementation. Table 2.2 summarizes the fitting result for the single ion trap.

Geometric Factor

The geometric factor is used to compare the $l = 2$ quadrupole field produced by a practical trap design to the one of the ideal design with the same electrode spacing. For instance, from Eq. (2.1), the potential field in an ideal linear Paul trap has the following form

$$\frac{V_0}{2} \frac{x^2 - y^2}{r_0^2},$$

where V_0 is the voltage applied to the electrodes and r_0 is the shortest distance from the trap center to the electrodes. The geometric factor κ_r is then obtained by comparing the above equation (with $V_0 = 1$) to the corresponding $(l, m) = (2, 2)$ term from the

expansion:

$$\frac{\kappa_r}{2r_0^2} (x^2 - y^2) = C_2^2 \Phi_2^2 = C_2^2 \times 3 (x^2 - y^2). \quad (2.20)$$

Table 2.2. The coefficients of the multipole expansion in Eq. (2.18) with a cutoff at $l = 8$. In B1, RF electrodes in the (+x,+y) and (-x,-y) quadrants are held at 1 while all other boundaries are at zero. In B2, RF electrodes in the (-x,+y) and (+x,-y) quadrants are charged. In B3, the endcap electrodes are charged. In this simulation and analysis, the length unit is mm. Only those points within $\sqrt{x^2 + y^2} < 0.2$ mm and $|z| < 0.8$ mm are included in the fitting.

l	m	B1: RF-1	B2: RF-2	B3: Endcaps
0	0	4.83×10^{-1}	4.83×10^{-1}	2.87×10^{-2}
2	0	-1.50×10^{-1}	-1.49×10^{-1}	3.01×10^{-1}
2	2	-1.35×10^{-4}	4.05×10^{-5}	1.17×10^{-4}
2	-2	-1.86×10^1	1.86×10^1	6.04×10^{-3}
4	0	-2.17×10^{-1}	-2.24×10^{-1}	4.43×10^{-1}
4	2	-2.81×10^{-4}	5.15×10^{-4}	-2.45×10^{-4}
4	-2	1.69	-1.46	-2.29×10^{-1}
4	4	-1.07×10^{-3}	-1.22×10^{-3}	8.97×10^{-4}
4	-4	-2.45×10^{-1}	-1.07	1.60
6	0	-2.92×10^{-1}	-2.80×10^{-1}	5.75×10^{-1}
6	2	3.53×10^{-4}	-5.37×10^{-4}	1.89×10^{-4}
6	-2	-1.19×10^1	1.08×10^1	1.12
6	4	-1.58×10^{-4}	-3.26×10^{-4}	4.83×10^{-4}
6	-4	9.96×10^1	-5.62×10^1	-4.41×10^1
6	6	-3.73×10^{-5}	3.64×10^{-5}	8.50×10^{-7}
6	-6	1.12×10^5	-1.02×10^5	-1.06×10^4
8	0	4.97×10^{-3}	-2.65×10^{-3}	-2.28×10^{-3}
8	2	-1.44×10^{-4}	2.04×10^{-4}	-6.06×10^{-5}
8	-2	2.79×10^1	-2.65×10^1	-1.40
8	4	-1.10×10^{-5}	2.35×10^{-5}	-1.23×10^{-5}
8	-4	-2.53×10^2	9.28×10^1	1.61×10^2
8	6	2.26×10^{-6}	-2.95×10^{-6}	6.68×10^{-7}
8	-6	-1.30×10^5	1.52×10^5	-2.14×10^4
8	8	5.75×10^{-6}	-1.48×10^{-5}	8.90×10^{-6}
8	-8	3.48×10^8	-2.66×10^8	-8.13×10^7

Hence, the geometric factor for the RF electrodes is

$$\kappa_r = 6r_0^2 C_2^2 \text{ or } \kappa_r = \frac{r_0^2 C_2^{-2}}{16} \quad (2.21)$$

and, similarly, the geometric factor for the endcap electrodes is

$$\kappa_z = 2z_0^2 C_2^0. \quad (2.22)$$

Note that the choices of r_0 and z_0 can be somewhat arbitrary; however, it is usually the shortest distance from the trap center to the electrodes.

For the RF field in the single ion trap, $r_0 = 0.457$ mm and $C_2^{-2} = 18.6$, and therefore $\kappa_r = 0.24$. For the endcap DC field, $z_0 = 0.95$ mm and $C_2^0 = 0.301$, and therefore $\kappa_z = 0.54$.

In most cases, the geometric factor is less than unity, implying the real electric field is less effective than a pure quadrupole field. However, it does not necessarily imply less trapping.

CHAPTER 3

Apparatus for the Single Ion Trap

The single ion trap is the house for the single ion precision spectroscopy experiment. This chapter introduces the apparatus for the experiment with a single trapped barium ion.

3.1. The Single Ion Trap

This trap is designed to trap ions in the Lamb-Dicke regime such that we can drive sideband transitions to perform motional quantum state manipulation such as ground state cooling. Typically, the value of the Lamb-Dicke parameter is set to about 0.1. To build a trap for a single $^{138}\text{Ba}^+$ in this regime, we first determine the secular frequency needed. The Lamb-Dicke parameter is the ratio between the ground state wavefunction extent a_0 and the transition wavelength λ . For $\eta \approx 0.1$ and $\lambda \approx 1000\text{ nm}$ for a typical optical transition, the wavefunction spread a_0 is of order 30 nm. As $a_0 = (2\hbar/m\omega)^{1/2}$, the trap secular frequency ω is then of order $2\pi \times 1\text{ MHz}$ for the barium ion.

The motional quantum state manipulation is usually performed in the axial mode along which micromotion is minimal. From Eq. (2.8) we have

$$\frac{V_{\text{ec}}}{z_0^2} = \frac{\omega_z^2 m}{e\kappa_z} = 2.8 \times 10^2 [\text{V}/\text{mm}^2]$$

for $\omega_z = 2\pi \times 1\text{ MHz}$ and assuming $\kappa_z = 0.2$. Therefore, if we supply up to 1000 V to the endcaps, the separation between the two electrodes is of order millimeters.

The radial part of the trap is designed in a similar manner. Assuming there is no DC field in the radial direction, from Eq. (2.10) the radial secular frequency is then $\omega_r = q_r \Omega / 2\sqrt{2}$ where Ω is the RF drive frequency and q_r is either q_x or q_y . That is

$$\frac{V_{\text{rf}}}{r_0^2 \Omega} = \frac{\sqrt{2} m \omega_r}{e}$$

when the radial geometric factor is unity. We would like to keep the radial secular frequencies higher than the axial secular frequency so the axial secular motion is less likely to resonant, either directly or parametrically, with the radial modes. Also, in the single ion precision spectroscopy experiment, where a spectroscopy ion is co-trapped with a logic ion, the two-ion ensemble can be kept aligned to the axis to minimize RF micromotions. We chose the radial secular frequency to be twice of the axial one. Since the secular motion approximation in Eq. (2.9) is valid when the RF drive frequency is much higher than the secular frequency, we set the RF frequency Ω to be at least 10 times of the radial frequency. For example, with $\omega_r = 2\pi \times 2$ MHz, $\Omega = 2\pi \times 20$ MHz, and V_{rf} up to several hundred volts, the trap's radial size r_0 is 1 mm or so.

Geometry

The outline of the single ion trap is illustrated in Fig. 3.1. The RF field is provided by four rod electrodes, and the axial confinement is provided by two endcap pins installed on the trap axis. Due to the RF circuit configuration (see page 48), the RF electrodes can not be DC biased individually. Therefore, there are additional four rod electrodes surrounding the trap, similar to the RF electrodes, to provide DC electric field in the radial direction.

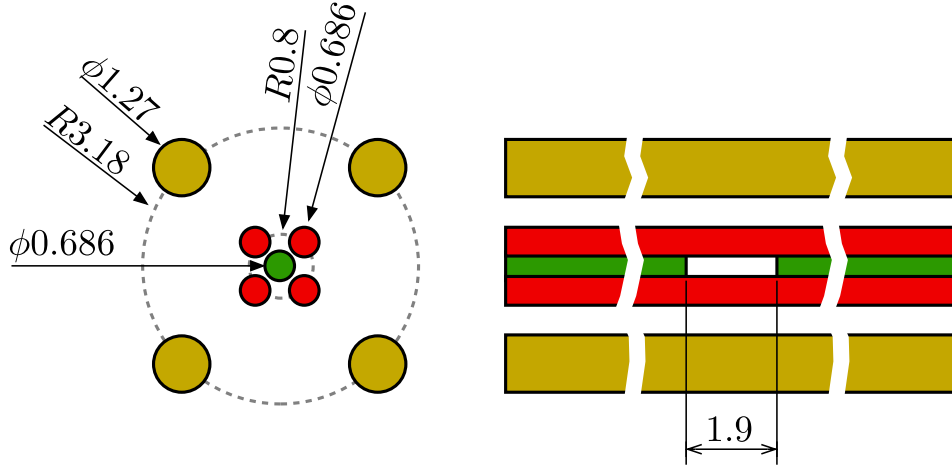


Figure 3.1. Single ion trap outline

The RF electrodes have a 0.686 mm diameter and are made of tungsten. They are evenly distributed over a circle of 0.8 mm radius; r_0 is 0.457 mm. The DC bias electrodes have a 1.27 mm diameter and are made of stainless steel. They are located on a circle of 3.18 mm radius, directly behind the RF electrodes. The endcap electrodes are made of the 0.686 mm tungsten wire as well. The two endcaps are separated by $2z_0 = 1.9$ mm. This configuration is simulated and analyzed by the procedure in Section 2.2, from which the geometric factors $\kappa_r = 0.24$ and $\kappa_z = 0.54$ are obtained.

Trap Electrodes

Although an ion trap acts like a capacitor and there is no current flowing between the electrodes via free space, charges are constantly redistributing on the electrode surfaces when the trap is driven with RF signal. Known as the skin effect, the AC field propagates near the surface in a conductor. Therefore the AC conductivity can be significantly worse than the DC conductivity, and the area around the trap electrodes can accumulate lots of heat as heat dissipation is extremely slow in the vacuum. The skin depth δ of a conductor

Table 3.1. Skin depth and AC resistance

Material	Resistivity ρ (Ω m)	Relt. permeability $\mu_r = \mu/\mu_0$	Skin depth δ (μm)		
			1 MHz	3 MHz	10 MHz
Aluminum	2.65×10^{-8}	1	81.9	47.3	25.9
Copper	1.69×10^{-8}	1	65.4	37.8	20.7
Nickel	6.9×10^{-8}	200	9.3	5.4	3.0
numlver	1.63×10^{-8}	1	64.3	37.1	20.3
Stainless steel 300	$\approx 7 \times 10^{-7}$	≈ 1	421	243	133
Tungsten	5.4×10^{-8}	1	117	68	37

is approximately

$$\delta = \sqrt{2\rho\Omega\mu} \quad (3.1)$$

where ρ is the DC resistivity, μ is the permeability, and Ω is the AC angular frequency.

For a rod electrode of radius r , the AC resistance per axial unit length is

$$R_\Omega \approx \frac{\rho}{2\pi r\delta} \quad (3.2)$$

when the rod thickness is much greater than the skin depth. Table 3.1 lists the skin depth for some common materials. In particular, when driven at around 20 MHz, the skin depth of the tungsten electrodes is around 25 μm , fraction of the physical radius. Hence, the conduction of charges on the electrodes is limited by the skin effect but not the physical cross-section of the rod.

Tungsten is chosen over stainless steel because of its better AC conductivity. As aluminum and copper are softer than tungsten, building a millimeter scale ion trap with tungsten may be easier. Silver has the best conductivity among the common materials in Table 3.1; in the future, one can consider plating the electrode with silver to further reduce the resistance.

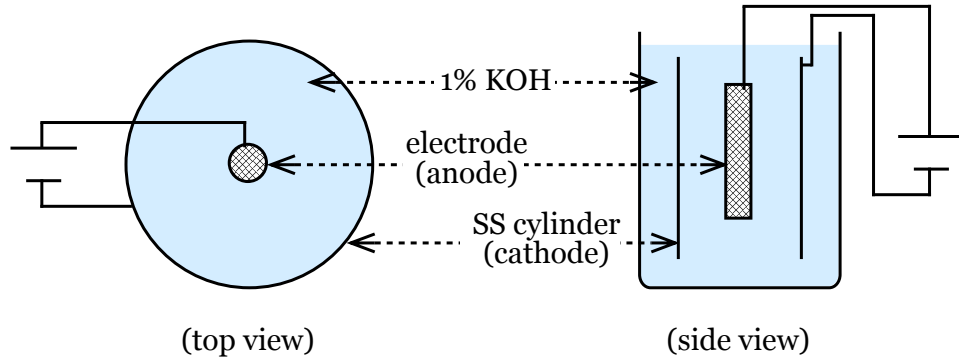


Figure 3.2. Tungsten wire electropolishing

All the electrodes were fabricated from stocked materials. They were trimmed, etched, and polished in house. For small diameter, both stainless steel rods and tungsten rods are fairly easy to handle in the laboratory. These electrodes were first cut off from a longer raw piece. They were trimmed to the desired length with Dremel cutting and grinding discs. Oxygen-free copper (OFHC) wires were bonded to each electrode by silver brazing for connecting to the external DC/RF circuitries. Lastly, the electrodes were electropolished before assembled with other parts.

Electropolishing

Electropolishing is a polishing process utilizing electrolysis. It uses ions in the aqueous solution to remove roughness on a conducting surface, where field emission is more likely to take place when driving at a higher voltage. There were also studies showing a polished trap has a lower motional heating rate, which is crucial for motional quantum state manipulation.

Different metals require different recipes for electropolishing. For tungsten, I followed the instruction by Latawiec and Lockwood (1966); Hunt (1976). As illustrated in Fig. 3.2, the tungsten rod electrode (anode) and a stainless steel tube (cathode) are set up coaxially

in the 1% potassium hydroxide (KOH) solution. One of the keys to successful electropolishing is to have a uniform electric field density. For cylindrical objects, this is achieved by using a cathode tube which has a large inner diameter and is longer than the rod to be polished. The inner diameter of the tube I used is around 50 mm. Good electropolishing also requires right current density as well as the application time. The reference provided a suggestion to the voltage and the reaction time as a starting point; however, these parameters require further experiment. Usually, the tungsten parts are found grayish before any surface treatment. While electropolishing removes the surface roughness as well as contamination, polished tungsten part shows a shining surface. Unfortunately, we did not have any equipment to further exam the surface. Empirically, I found insufficient and rushed electropolishing would both result in a fuzzy and darkish surface, and usually optimizing the electrolysis voltage would make an improvement.

For parts with complicated geometry, professional electropolishing services such as Abel Electropolishing (Chicago, IL) should be considered.

Macro Electrode Mount

The trap electrodes are held by four macro stands, see Fig. 3.3. Macro is a machinable ceramic material; it is compatible with the ultra-high vacuum. The DC resistivity is $10^{17} \Omega \text{ cm}$. While high voltages are supplied to the trap, it is necessary to check for Macro's dielectric breakdown. The DC threshold is 129 kV/mm, and the AC threshold is 45 kV/mm. In this trap, the gap between the RF electrodes to the endcap electrodes is the smallest, approximately 0.11 mm. Assuming the voltage difference between electrodes is 1000 V, the electric field is then approximately 9 kV/mm, which is well below both the AC and DC breakdown threshold.

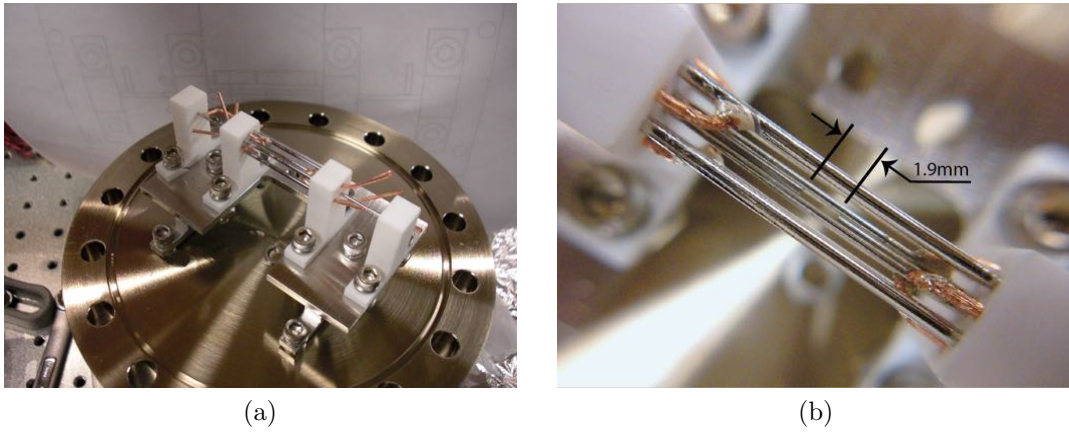


Figure 3.3. Trap assembly

The outline of the macro stands are shown in Figs. C.1 to C.3.

Trap Assembly

The trap was assembled onto a base plate first, and then the whole assembly was mounted inside a 6" octagon vacuum chamber (Kimball Physics MCF600-SphOct-F2C8). Electrical connections are established by bare oxygen-free copper wires as mentioned earlier. Both the pushpin connectors and the barrel connectors (both from Kurt J. Lesker) were used to join wires to the feedthroughs. Each diagonal pair of the RF electrodes were internally connected, thus there are two lines for the RF; they are connected to an RF feedthrough. All the other DC electrodes (two endcaps and four biasing electrodes) are connected to another vacuum electrical feedthrough.

The partially assembled trap is shown in Fig. 3.3. After other trap accessories such as the oven are installed inside, the vacuum chamber is evacuated and sealed.

3.2. Trap Electrical

RF Source

The operation of an ion trap requires several hundred volts on the RF electrodes to keep a single barium ion with sufficiently radial confinement. Such high RF voltage is usually achieved by using a resonator with a high quality-factor. Most ion trapping laboratories use a coaxial resonator for this purpose.

The idea of using a coaxial resonator to produce the high RF voltage is to have a quarter-wave resonance and the load that requires a high RF voltage is attached to the anti-node (at the quarter-wave location). In a coaxial resonator, one end of the core is short to the ground while the other end remains open and is connected to the RF electrodes. This configuration forms a quarter-wave resonance because, when on resonance, the RF electromagnetic field across the resonator is exactly 1/4 of the wavelength (Viz-muller, 1995). The simplest form of a coaxial resonator is a straight inner conductor inside a cylindrical shell ground and the length of the resonator is quarter wavelength. This design is then unpractical for 25 MHz RF as the wavelength is 12 m. However, by introducing a helical inner conductor, the group velocity of the electromagnetic wave is much slower and hence significantly reduces the resonator's dimensions (Zverev, 1967).

Some empirical design equations for helical resonators can be found in Macalpine and Schildknecht (1959) and was employed when building the resonator for this single ion trap. Refer to Fig. 3.4 for the outline of the helical resonator. Although there are several dimensions in the resonator, one only needs to choose the resonance frequency f_e and the diameter of the shield D . Other parameters such as resonator length B , wire gauge d_0 ,

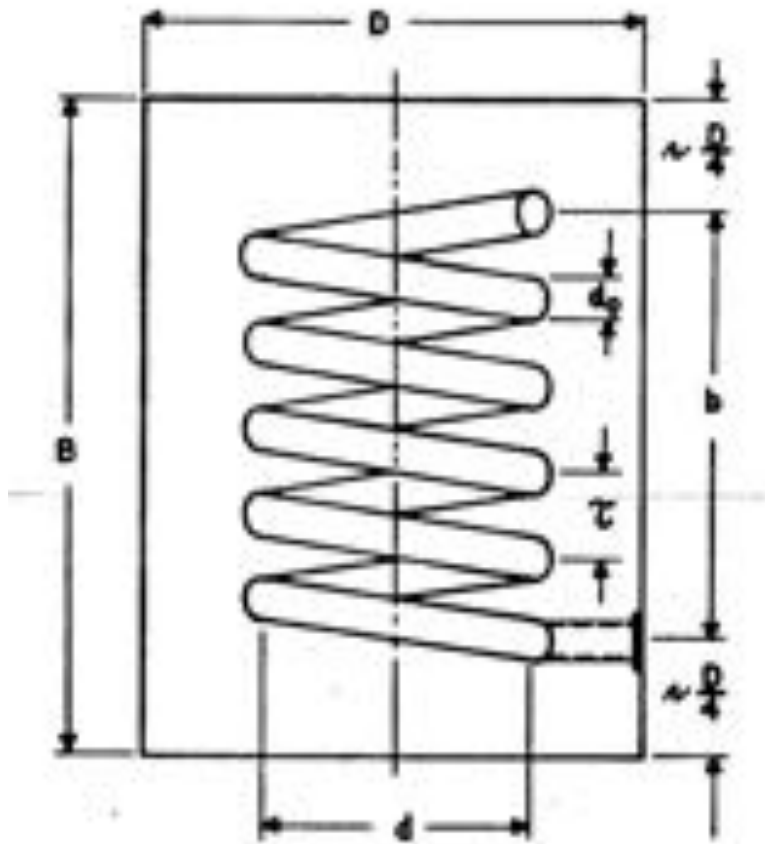


Figure 3.4. Outline of a helical resonator. (From Macalpine and Schildknecht (1959, Fig. 2))

helix radius d and pitch τ are determined automatically by either physics laws or optimized conditions found empirically. However, note that the resonance of a helical resonator will be shifted when an additional capacitance is loaded. In practice, one anticipates 5 to 10 pF each from the trap and other circuit components such as cables and connectors; the capacitance of our helical resonator is estimated to be around 5 pF. Therefore, the loaded resonant frequency is expected to lower by about 1/2 as the resonance goes inversely as the square root of capacitance.

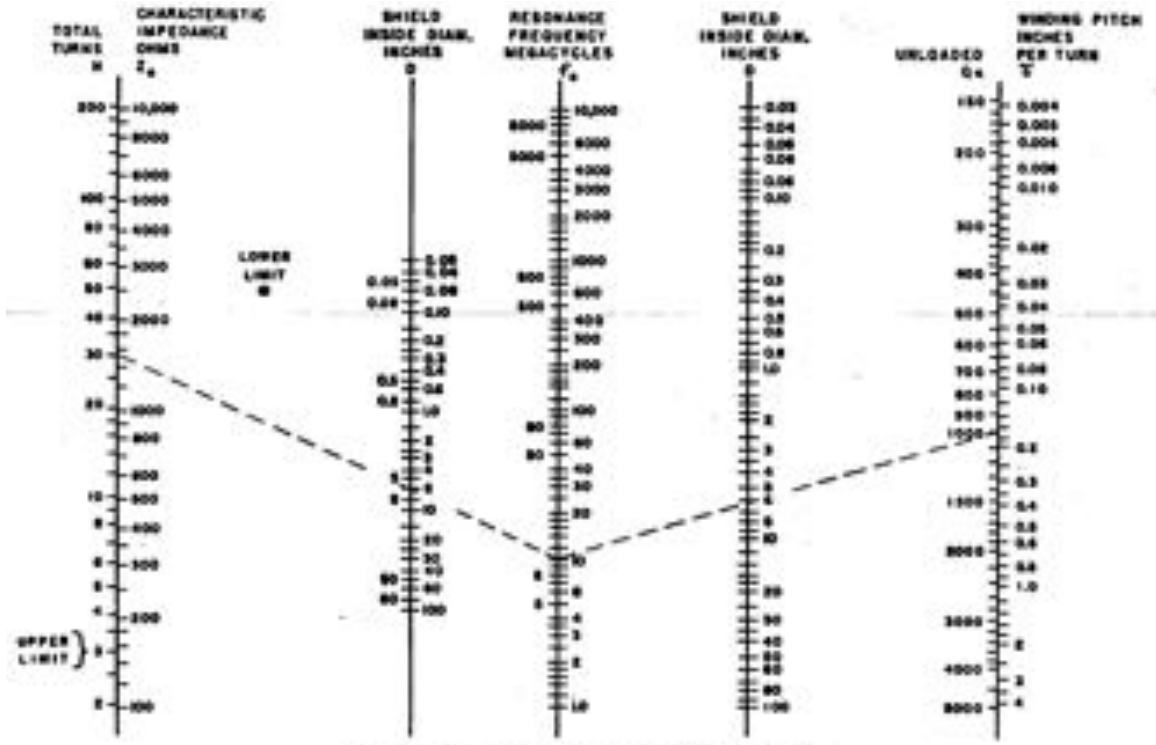


Figure 3.5. Helical resonator design chart. (From (Macalpine and Schildknecht, 1959, Fig. 4))

In light of the shift, I designed this helical resonator to have unloaded resonant frequency $f_e = 50$ MHz with a 109.2 mm inner diameter ground shield. By using the chart in Fig. 3.5, the helical coil is found to have $N = 9$ turns with $\tau = 9.4$ mm pitch. The coil diameter d is 61 mm based on the optimized condition $d/D = 0.55$. The wire gauge d_0 is $1/8''$ (3.175 mm), much greater than the skin depth (around $10 \mu\text{m}$ in 10 to 100 MHz) of the RF electric field to have low loss. Both the coil and the shield are oxygen-free copper. Note that the design of the helical resonator is not unique, but is constrained by practical issues. For instance, we constructed the coil from a 72''-long (~ 1.8 m) copper rod. This rod was the longest piece we could easily obtain and was just long enough to build the

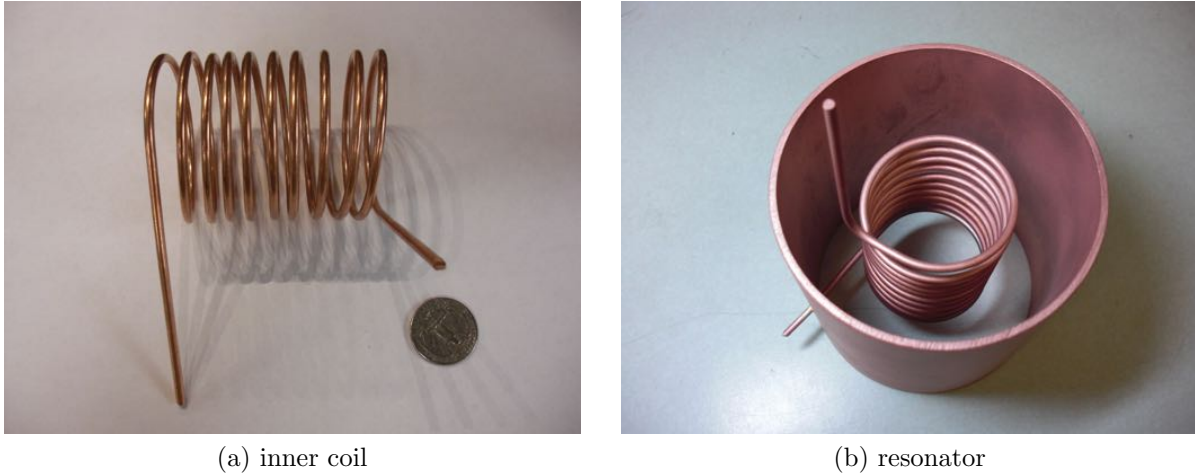
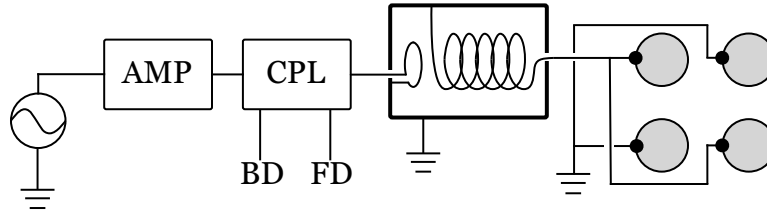


Figure 3.6. The helical resonator used to drive the single ion trap.

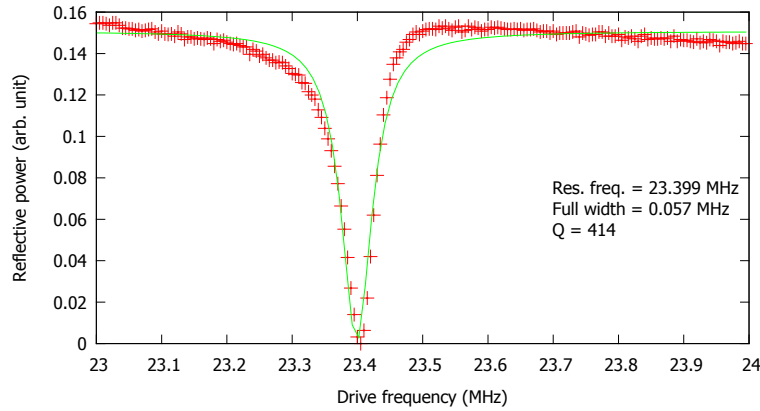
coil. In terms of the rod diameter, a thicker rod is harder to wind into a coil; a thinner rod will result in a springy coil which hurts the resonator's stability.

Additional two copper end caps are added to the ground can to better shield the RF field in the resonator. The open end of the core conductor is directly attached to the vacuum feedthrough to delivery RF to the trap. I found that using extra cables and common RF connectors adversely degrades the resonance quality factor and stability. Proper grounding of the resonator is crucial to the stability as well. I used a stainless steel grounding braid to connect the ground can to the optical table.

The energy is coupled into the circuit by magnetic induction; see Fig. 3.7 for the schematic. The coupling coil is a single loop magnet wire of which the diameter is slightly smaller than the one of the resonator's helical coil. The loop is aligned to the resonator's coil coaxially; the location was adjusted for optimal coupling. The primary circuit (i.e., the coupling loop) has a bi-directional coupler that samples 20 dB of the RF power traveling forward and backward. The RF traveling forward carries the power pumping the



(a) circuit



(b) resonance

Figure 3.7. RF resonant circuit with a helical resonator

resonator, and the RF not coupled into the resonator travels backward. The RF resonant circuit is optimized by tuning the drive frequency and the location of the coupling loop such that the reflective RF is minimized. Figure 3.7(b) is a typical spectrum of the loaded resonator. A resonance is found at 23.5 MHz with a linewidth of 60 kHz. The Q factor is 400, while the unloaded Q factor is around 1500.

The pump source is generated by a signal generator followed by an RF amplifier with approximately 40 dB gain. The RF source with up to 37 dBm power drives the primary coupling coil directly. Figure 3.8 shows the output voltage at different pump power. The output voltage is measured at the feedthrough conductor, which is the closest test point to the trap electrodes. Although the measurement is done with a high impedance oscilloscope

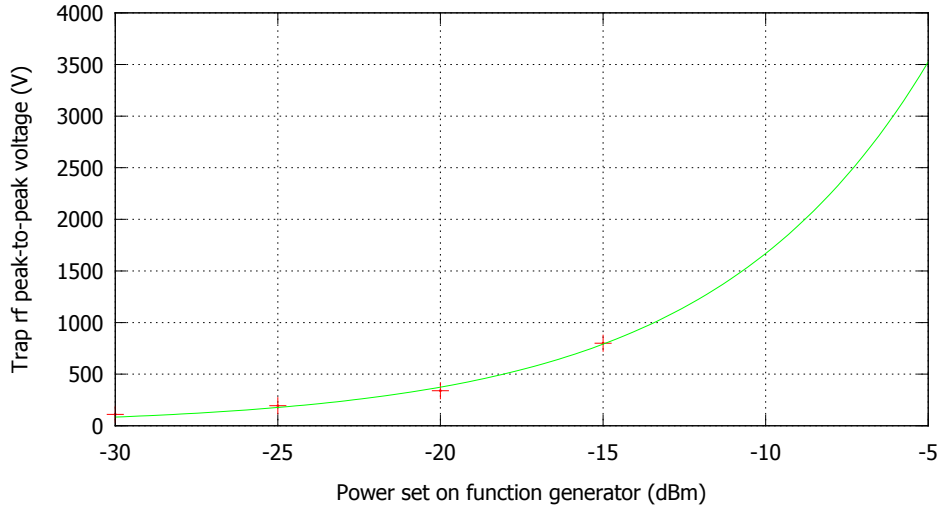


Figure 3.8. RF voltage calibration

probe, the circuit is still perturbed such that the resonance is shifted. However, the quality factor lowers only slightly, thus this calibration should be representative. The peak-to-peak RF voltage is around 3500 V when the circuit is resonantly pumped by 37 dBm.

Note that the above calibrations were performed with the trap in vacuum condition. In particular, when the trap chamber's pressure is of order 1 Torr, the RF electric field generated by this system is able to cause vacuum arc.

In passing, Siverns *et al.* (2012) provides another example of using a helical resonator for driving the ion trap.

DC Controls

The DC voltages for the endcaps and the biasing electrodes are each provided by a high voltage regulation circuit outlined in Fig. 3.9. The circuit uses a two-stage amplification structure: field-effect transition Q1 forms a common source amplifier stage and Q2 forms a common drain stage (Horowitz *et al.*, 1980).

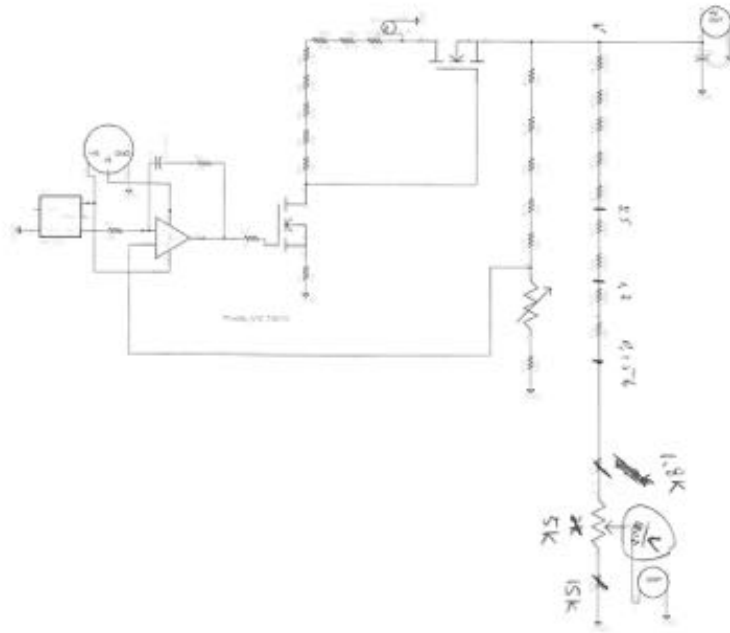


Figure 3.9. High voltage regulator

A low-pass filter is added in between each DC electrode and its voltage source to stabilize the DC voltage on the electrode. As illustrated in Fig. 3.10, the filters also prevent the RF power, capacitively picked up by the DC electrodes, traveling backward and perturbing the DC supplies. The single ion trapping system uses a simple low-pass RC filter. The resistor is $50\text{ k}\Omega$ and the capacitors are $22\text{ }\mu\text{F}$, which results in the 3 dB cutoff frequency to be 0.14 Hz ; at the RF drive frequency $\Omega = 2\pi \times 24\text{ MHz}$, the attenuation is 82 dB.

The resistor in this low-pass filter can be replaced by an inductor. The revised version is called a π -filter, which is commonly used in RF electronics for its low impedance. However, as there is no DC current flowing between the voltage source and the electrodes, one can use either version of the filter circuit.

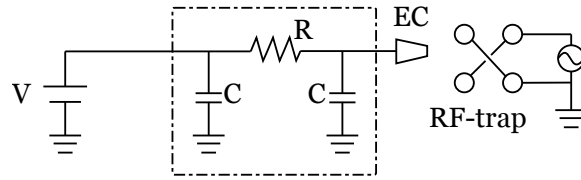


Figure 3.10. The DC low-pass filtering circuit. V: DC voltage supply. C: $22\ \mu\text{F}$ capacitor. R: $50\ \text{k}\Omega$ resistor. EC: endcap electrode. RF-trap: nearby RF electrodes. The box indicates the filter box.

3.3. Barium Oven

barium ions are loaded into the trap by photoionization. A neutral barium flux is generated by the barium oven, and then the neutral barium is ionization inside the trap.

The oven is an alumina tube with one end fused and wrapped by a tungsten heating filament. See Fig. 3.11. It is attached to a vacuum electrical feedthrough directly to form a single assembly. This particular feedthrough is dedicated for the oven for easy transportation. Because the tungsten filament is rigid enough, the oven is only held by the tungsten coil whose two ends were spot-welded onto the feedthrough conductors. However, when heated up, thermal expansion may deform the coil and shifts the oven's position. Therefore, it takes some practice and attempts to build a satisfactory oven assembly.

Inside the chamber, the oven is aligned vertically, about 25 mm directly below the trapping region. While the oven output flux is expected to be quite diverging, I used two apertures to produce a somewhat collimated atomic beam pointing toward the trap. In practice, the two apertures were installed beforehand during the trapping assembling to ensure good alignment, see Fig. 3.11(b).

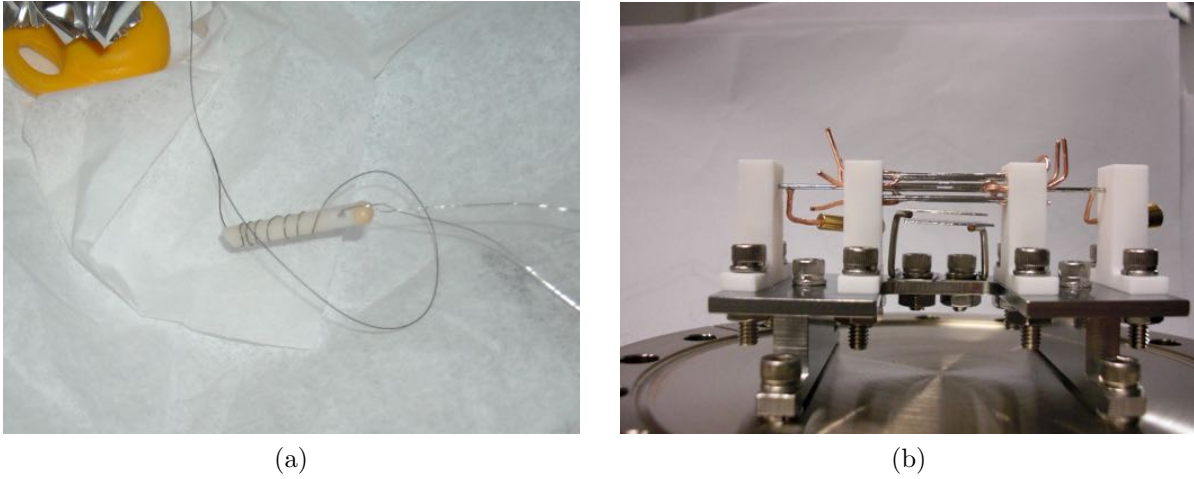


Figure 3.11. (a) Alumina tubing with tungsten coil as the barium oven. (b) The apertures for the oven output.

To fill the oven, barium is chopped into smaller pieces to fit it the tube. Since barium is quite reactive, the oven preparation was done in a nitrogen-filled glove box to slow down oxidization. After the oven was prepared, it was installed onto the vacuum chamber within the shortest possible time; the chamber was pumped down right after the installation.

The heating filament is usually driven at 1.2 A, which would make the tungsten coil glowing.

Photoionization will be discussed in Section 4.1. Ablation loading, a different loading strategy which does not require an oven, will be discussed in Section 7.1.

3.4. Laser Systems

The single ion experiment used four lasers: two (791 nm and 337 nm) for the photoionization loading of barium, and two (493 nm and 650 nm) for the Doppler laser cooling and internal state manipulation.

The 493 nm laser drives the $6S_{1/2} \rightarrow 6P_{1/2}$ transition in Ba^+ . It is an integrated Toptica DL-Pro laser system with an IR laser diode at 987 nm pumping a cavity-enhanced second harmonic generation module. The frequency doubling involves the noncritical phase matching (NCPM) with a potassium niobate ($KNbO_3$) crystal. This SHG process is tuned by the crystal's temperature and is optimized at $\approx 40^\circ C$ with 80 mW output power.

The 650 nm laser, which drives the $5D_{3/2} \rightarrow 6P_{1/2}$ transition in Ba^+ , is a DL-100 module with 20 mW output power. Part of the ECDL output is used to injection lock a slave diode laser, which provides more 650 nm laser power. Injection locking uses the master laser to force the slave laser's cavity resonating at the same mode. This is done by counter-propagating the master laser against the slave laser's output such that the master laser's field is injected into the slave laser's gain medium. In this project, the slave laser diode has an anti-reflection coating such that there is an insufficient reflection to form the laser cavity used to establish stable laser mode internally. In general, non-AR-coated laser diode would work equally fine, but with a smaller capture range for locking. Injection locking is confirmed by inspecting the slave laser's spectrum on a scanning Fabry-Perot interferometer.

The 791 nm laser is a DL-Pro module; it couples the $6s^2\ ^1S_0$ and the $6s6\ ^3P_1$ states in neutral barium atoms as the first step of the photoionization. The nitrogen laser, a pulsed ultra-violet (337 nm) gas laser, further ionizes the excited population to form Ba^+ . The N_2 laser is a Stanford Research System NL100.

3.5. Laser Stabilization

The wavelength of an ECDL is controlled by the driving current, the operating temperature, and the piezo's thickness (which is set by its applied voltage). These parameters are sensitive to the environment's perturbation and thus need to be regulated. Furthermore, the laser's driving parameters are modulated to actively stabilize the output frequency.

Laser frequency stabilization involves frequency (or wavelength) measurement and error-correcting feedback. In the lab, we routinely stabilize lasers through directly wavelength measurement by a wavelength meter. This approach is quick and least involving but has slow feedback bandwidth and less accurate. Detail follows.

Stabilizing lasers by a wavelength meter is straightforward. In the lab, we measure the laser frequency by the HighFines WSU-2 optical wavelength meter which has a 2 MHz short-term resolution. Over a longer time scale, the measurement result is highly correlated to the environmental parameters such as ambient temperature and atmospheric pressure. Therefore, we periodically calibrate our wavelength meter with a stabilized Helium-Neon laser (Research Electro-Optics, Inc.) which provides ± 3 MHz stability over several hours.

In order to stabilize multiple lasers, laser beams are combined via polarizing or dichroic beam splitters before coupling into the wavemeter. As measurement can be performed for only one laser each time, we put each sample beam through an acoustic-optical modulator and program these AOM switches to rotate the measurement. A computer controls the measurement sequences, captures the result, and generates the feedback signals at a National Instruments analog output card. In practice, the repetition time for the feedback is

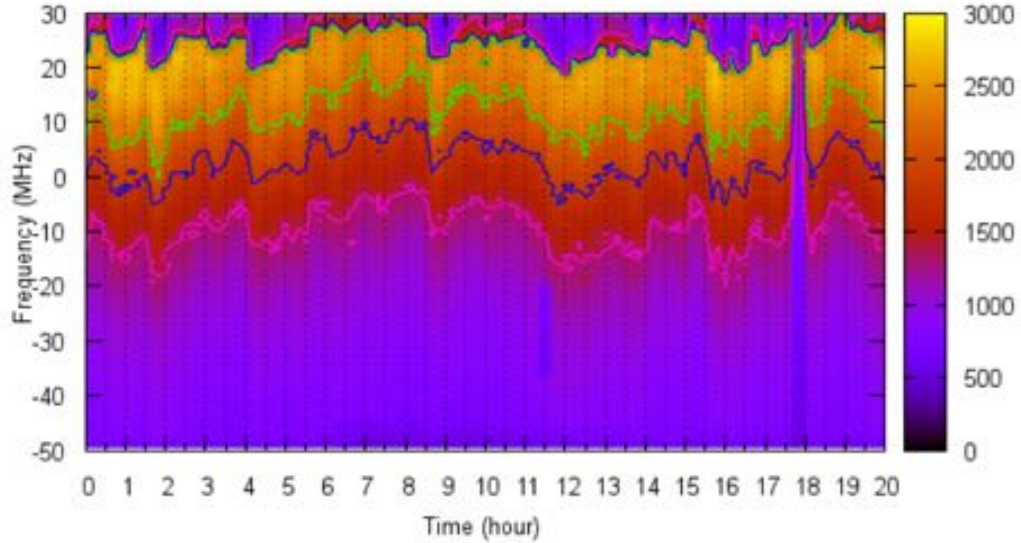


Figure 3.12. Drift of the wavelength meter locking mechanism.

of order 100 ms for each laser. Currently, there are up to 5 lasers locked to the wavemeter and the feedback bandwidth is 2 to 3 Hz.

The performance of our wavemeter locking is tested by performing laser induced fluorescence spectroscopy with Ba^+ . Refer to Section 4.2 for details of Ba^+ spectroscopy; in short, the fluorescence from a single barium ion is monitored for around 20 hours. If the excitation laser frequency changes, then the fluorescence changes as well. In this test, only the relevant lasers, the 493 nm and the 650 nm lasers, are stabilized to the wavelength meter; the wavemeter is calibrated to the stabilized He-Ne laser every 30 minutes. In Fig. 3.12, I plot the fluorescence count at different laser detuning added by an AOM. In the plot, the contour that yields a constant fluorescence count is then a measurement of the laser frequency drift over time. The vertical dashed lines mark the periodic He-Ne

calibration and are often found to coincide big jumps in the drift. Overall speaking, our wavemeter locking mechanism is able to keep lasers stabilized to ± 10 MHz within a day with frequent calibration to the He-Ne laser. Without calibration, the wavemeter can quickly drift away within an hour.

3.6. Fluorescence Detection

We detected the barium ion with its fluorescence. With efficient laser cooling, trapped ions can be highly localized such that the fluorescence is like a point light source, which can be imaged by microscope setup. When Coulomb crystal is formed, the typical spacing between localized ions is of order $10\ \mu\text{m}$. While the size of the camera sensor pixels is also around $10\ \mu\text{m}$, approximately 10 times optical magnification in the imaging system would be sufficient to resolve single ions on the camera.

The outline of the optical system for collecting barium fluorescence is depicted in Fig. 3.13. Like common microscopy design, the imaging system has three major parts: the objective lens, the relay lens, and the tube lens. The objective collects light from the object and the tube lens focuses the light onto the camera sensor for forming the image. While we adopt the infinity corrected configuration where the rays are collimated in between the objective and the tube lens, the separation between these two optics becomes an independent parameter. In addition, a relay lens, which is like a Galilean telescope, can be inserted to provide additional magnification.

In this setup for imaging a single ion, the objective lens is a 2"-diameter aspheric lens with a 40 mm focal length. The relay optical system is a Galilean telescope made of an $f = 100\text{ mm}$ and an $f = 30\text{ mm}$ achromatic doublet lens, which provides 3.33X

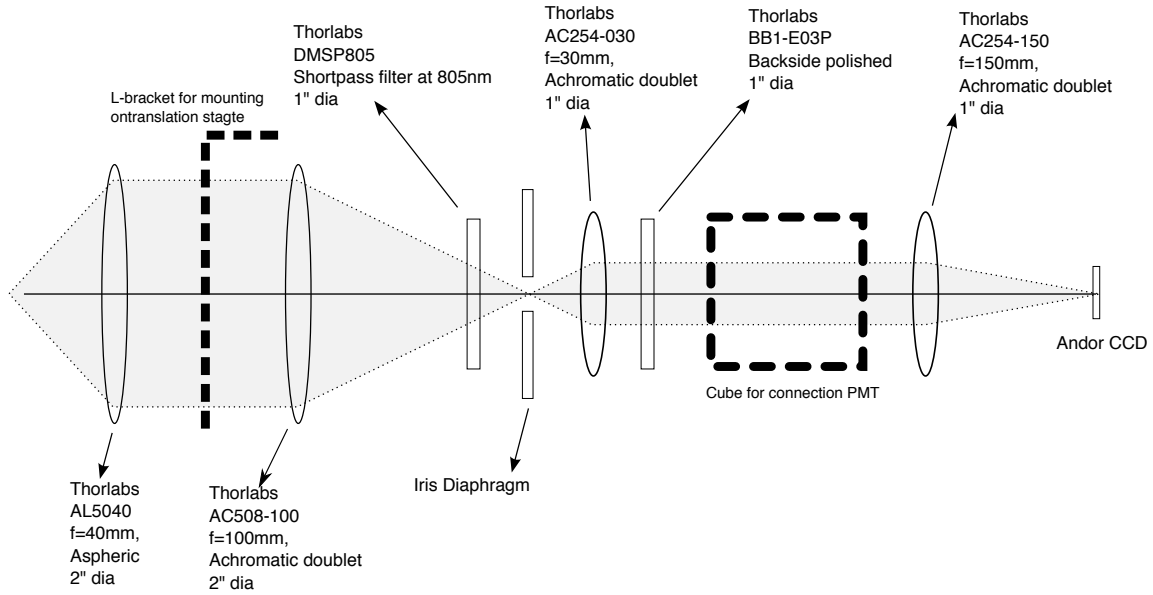


Figure 3.13. Imaging optics for the single ion experiment.

magnification. Inside the relay optics, a small iris is placed at the internal focal plane for blocking stray light. This approach is like setting an entrance pupil at the object and has significantly reduced the level of background scattered light. An optical bandpass filter is attached to the relay lens to transmit photon with a wavelength around 493 nm, corresponding to the $6S_{1/2} \rightarrow 6P_{1/2}$ transition in Ba^+ . The transmission is further split evenly by a non-polarising beam splitter. Half of the light (the reflection of the NPBS) is sent to a photomultiplier tube (PMT) for photon counting purpose; rest of the light (the transmission of the NPBS) is focused by the tube lens, an $f = 150$ mm achromatic doublet lens, to form the image on an electron multiplying CCD (Andor Luca-R EMCCD). The overall magnification of this imaging system is 12.5X.

The trap electrodes partially block the ion's fluorescence. Treat the single ion as a point source, the solid angle of the emission is reduced to 0.56 sr, which is equivalent to

4.4% of the total fluorescence. The objective lens has a 0.98 sr solid angle, greater than the emission solid angle. Rest of the optics in the imaging system all have sufficient aperture sizes for light propagation. By taking the transmission of each optics into account, the collection efficiency is reduced to approximately 1%. However, due to optical aberration, the clear aperture of this system is, in fact, smaller for imaging, which would lower the collection efficiency roughly by 10. See Section 6.3 for more discussion and analysis. Fortunately, photon counting is immune to aberration, thus the efficiency is not affected. The total efficiency, due to the detector, signal amplifier, and the discriminator, is about 10%. Therefore, the overall photon counting efficiency is around 10^{-3} , which is equivalent to a maximum photon flux of 10^5 /s.

CHAPTER 4

Single Ion Experiments



Figure 4.1. A trapped single Ba^+ was first observed in the single ion trap at around 2pm on September 2, 2011.

This chapter discusses the operation of the single ion trap. First, a summary of this trap's physical properties follows.

- $r_0 = 0.457$ mm and $\kappa_r = 0.24$.
- $z_0 = 0.95$ mm and $\kappa_z = 0.54$.
- The trap is driven at $\Omega = 2\pi \times 23.5$ MHz.

Fig. 4.2 shows the theoretical region of the RF voltage V_{rf} and the endcap voltage V_{ec} for stable trapping. It also shows the expected secular frequencies. As mentioned earlier, we operate around $\omega_z = 2\pi \times 1$ MHz and $\omega_{x,y} \geq 2\pi \times 2$ MHz.

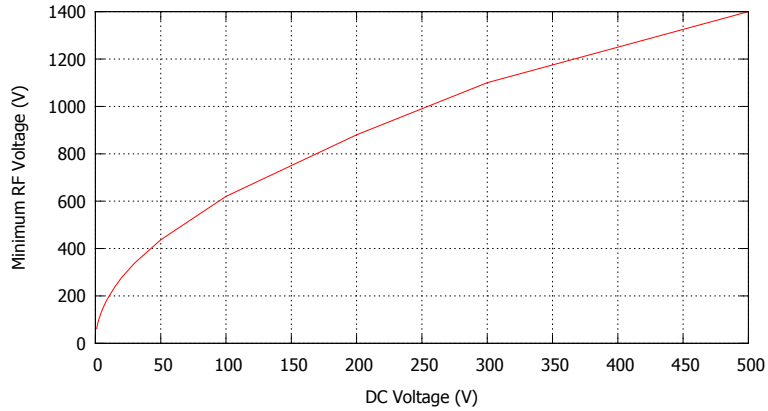


Figure 4.2. Stability region for V_{rf} and V_{ec} .

4.1. Loading an Ion

A single barium ion is loaded into the trap by photoionization where a first photon resonantly excites a neutral barium atom into an immediate excitation state, and a second photon subsequently drives the excited atom to its ionization continuum. This process is called the resonance enhanced multi-photon ionization or REMPI.

For loading barium ions, there are two convenient intermediate states one can use: $5d6p\ ^3D_1$ and $6s6p\ ^3P_1$. Excitation to $5d6p\ ^3D_1$ requires a 413 nm photon from the ground state, and exactly the same photon energy is sufficient to ionize from $5d6p\ ^3D_1$; this path is called the 1+1 REMPI while the two photons have the same energy. We did not seriously explore photoionization loading with 413 nm photon due to the difficulty of the laser source at the time. We instead utilized the $6s6p\ ^3P_1$ state. It takes a 791 nm photon to drive $6s^2\ ^1S_0 \rightarrow 6s6p\ ^3P_1$. From the intermediate state, the ionization threshold is 3.645 eV, or 340.1 nm, and can be easily fulfilled by a nitrogen gas laser. This process is called the 1+1' REMPI.

REMPI has an excellent state selectivity due to the use of a resonant transition. It is then useful for loading a specific isotope into the trap. With a narrow linewidth laser such as the 791 nm diode laser used in this task, the resolution of selection is mostly limited by the thermal Doppler broadening. However, in our oven setup, the oven output flux is filtered by two apertures to have a smaller divergent angle. Therefore, the transverse temperature of the neutral barium beam could be lower. While the laser interacts with the atomic beam transversely, the Doppler broadening is minimized.

Natural barium consists 71.7% of ^{138}Ba , followed by 11.2% of ^{137}Ba and 7.9% of ^{136}Ba . The isotope shift of the loading transition $6s^2\ ^1\text{S}_0$ to $6s6p\ ^3\text{P}_1$ is about 1.8 GHz between ^{138}Ba and ^{137}Ba ; it is around 100 MHz between ^{138}Ba and ^{136}Ba . See also Arroe (1950); Villemoes *et al.* (1993); Wendt *et al.* (1984); Steele *et al.* (2007) for the isotope shifts of other transitions both in Ba and Ba^+ .

While there is no specific requirement for the second photon as long as its energy is above the ionization threshold, the pulsed nitrogen gas laser is just an easy solution for UV wavelength. Nevertheless, there has been a demonstration of loading with UV led too (Wang *et al.*, 2011). With the pulsed UV laser, the loading rate is tuned to around 1 ion every several laser pulses. This is achieved by tuning the oven temperature, which determines the flux of the neutral barium atoms.

4.2. Laser Interaction with the Barium Ion

Laser interaction with the trapped Ba^+ facilitates several tasks in our laboratory including laser cooling and internal and motional quantum state manipulation. The barium ion has one valence electron. Similar to alkali metals, Ba^+ has a relatively simple level

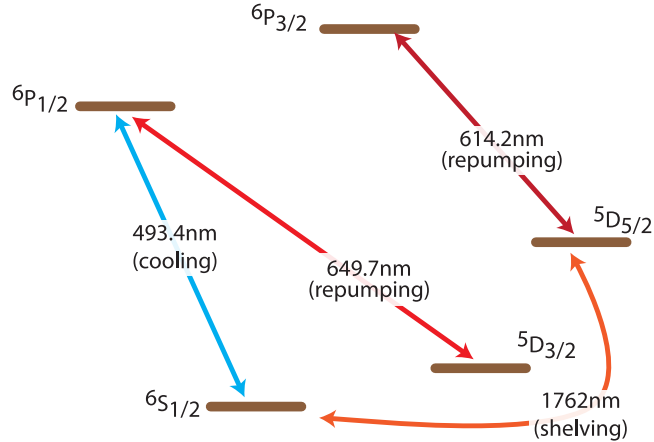


Figure 4.3. Partial level diagram of Ba^+ .

structure near the ground state as shown in Fig. 4.3 (Davidson *et al.*, 1992; Dzuba and Ginges, 2006; Curry, 2004; Arnesen *et al.*, 1975). The ground state of Ba^+ is $6s^2S_{1/2}$, while there are two meta-stable states $5d^2D_{3/2}$ ($\tau = 89.4s$) and $5d^2D_{5/2}$ ($\tau = 32.0s$) (Gurell *et al.*, 2007). The $D_{3/2}$ state and the ground $S_{1/2}$ state together with the $P_{1/2}$ form a closed cycling system, which is used for applications requires lots of photon scattering such as Doppler cooling. The $D_{5/2}$ state is isolated from the $S_{1/2}$ - $P_{1/2}$ - $D_{3/2}$ three-level Λ system and thus can be used as a shelving state to protect the population from falling into the Λ system.

Coherent Population Trapping

Laser interaction introduces coherence between the coupled two quantum states (Agap'ev *et al.*, 1993). In a three-level system, where three states are coupled by two lasers, coherences between each state can result in quantum interference. Coherent

population trapping (CPT) is a well-known destructive interference effect in a three-level system that, at the resonance condition, the photon scattering (absorption) in the system is suppressed. A Λ -type S-P-D three-level structure is found in several commonly trapped atomic ions such as Ba^+ , Ca^+ , Sr^+ , and Yb^+ . These species are heavier atoms that have vacant d electron orbitals. Here we briefly study this phenomenon.

The relevant system in Ba^+ is labeled as $|1\rangle=|6S_{1/2}\rangle$, $|2\rangle=|5D_{3/2}\rangle$, and $|3\rangle=|6P_{1/2}\rangle$. The density matrix of the system is given by

$$\rho = \begin{pmatrix} \rho_{11} & \rho_{12} & \rho_{13} \\ \rho_{21} & \rho_{22} & \rho_{23} \\ \rho_{31} & \rho_{32} & \rho_{33} \end{pmatrix} \quad (4.1)$$

where the ρ_{ii} terms are the population in $|i\rangle$ and the ρ_{ij} is the quantum coherence between $|i\rangle$ and $|j\rangle$. The dynamics of the density matrix is described by the optical Bloch equation

$$\dot{\rho} = \frac{i}{\hbar} [\rho, \mathcal{H}] + \left\{ \frac{\partial \rho}{\partial t} \right\} \quad (4.2)$$

where \mathcal{H} is the Hamiltonian, $[\cdot, \cdot]$ denotes the commutator, and $\{\partial\rho/\partial t\}$ is the decoherence. For two lasers with Rabi frequencies $\Omega_{1,2}$ and optical frequencies $\omega_{1,2}$ that respectively couple ground states $|1\rangle$ and $|2\rangle$ to the common excitation state $|3\rangle$, the system's Hamiltonian reads

$$\mathcal{H} = \begin{pmatrix} 0 & 0 & \frac{\hbar\Omega_1}{2}e^{i\omega_1 t} \\ 0 & \hbar(\omega_{31} - \omega_{32}) & \frac{\hbar\Omega_2}{2}e^{i\omega_2 t} \\ \frac{\hbar\Omega_1}{2}e^{-i\omega_1 t} & \frac{\hbar\Omega_2}{2}e^{-i\omega_2 t} & \hbar\omega_{31} \end{pmatrix} \quad (4.3)$$

where ω_{31} and ω_{32} are the energy differences from $|3\rangle$ to, respectively, $|1\rangle$ and $|2\rangle$. The decoherence matrix is built in the phenomenological manner. Here we consider decoherence only due to the spontaneous emission from $|3\rangle = |P_{1/2}\rangle$:

$$\left\{ \frac{\partial \rho}{\partial t} \right\} = \begin{pmatrix} \Gamma_1 \rho_{33} & 0 & -\frac{1}{2}(\Gamma_1 + \Gamma_2) \rho_{13} \\ 0 & \Gamma_2 \rho_{33} & -\frac{1}{2}(\Gamma_1 + \Gamma_2) \rho_{23} \\ -\frac{1}{2}(\Gamma_1 + \Gamma_2) \rho_{31} & -\frac{1}{2}(\Gamma_1 + \Gamma_2) \rho_{32} & -(\Gamma_1 + \Gamma_2) \rho_{33} \end{pmatrix} \quad (4.4)$$

with Γ_i being the spontaneous emission rate from $|3\rangle$ to $|i\rangle$.

The optical Bloch equation Eq. (4.2) can be simplified by applying Fourier transformations. Alternatively as well as equally, the simplification can be done by factoring ρ into two different timescales:

$$\rho_{ij}(t) = \tilde{\rho}_{ij}(t) e^{i\xi t} \quad (4.5a)$$

for the corresponding term in the Hamiltonian

$$\mathcal{H}_{ij}(t) \propto e^{i\xi t} \quad (4.5b)$$

with $\tilde{\rho}$ being the slow-varying amplitude in contrast of the high frequency $\exp(i\xi t)$ term.

With the above substitution, the optical Bloch equation Eq. (4.2) becomes

$$\dot{\tilde{\rho}}_{33} = \frac{i}{2}\Omega_1(\tilde{\rho}_{31} - \tilde{\rho}_{13}) + \frac{i}{2}\Omega_2(\tilde{\rho}_{32} - \tilde{\rho}_{23}) - (\Gamma_1 + \Gamma_2)\tilde{\rho}_{33} \quad (4.6a)$$

$$\dot{\tilde{\rho}}_{11} = -\frac{i}{2}\Omega_1(\tilde{\rho}_{31} - \tilde{\rho}_{13}) + \Gamma_1\tilde{\rho}_{33} \quad (4.6b)$$

$$\dot{\tilde{\rho}}_{22} = -\frac{i}{2}\Omega_2(\tilde{\rho}_{32} - \tilde{\rho}_{23}) + \Gamma_2\tilde{\rho}_{33} \quad (4.6c)$$

$$\dot{\tilde{\rho}}_{31} = i\delta_1\tilde{\rho}_{31} + \frac{i}{2}\Omega_1(\tilde{\rho}_{33} - \tilde{\rho}_{11}) - \frac{i}{2}\Omega_2\tilde{\rho}_{21} - \frac{1}{2}(\Gamma_1 + \Gamma_2)\tilde{\rho}_{31} \quad (4.6d)$$

$$\dot{\tilde{\rho}}_{32} = i\delta_2\tilde{\rho}_{32} + \frac{i}{2}\Omega_2(\tilde{\rho}_{33} - \tilde{\rho}_{22}) - \frac{i}{2}\Omega_1\tilde{\rho}_{12} - \frac{1}{2}(\Gamma_1 + \Gamma_2)\tilde{\rho}_{32} \quad (4.6e)$$

$$\dot{\tilde{\rho}}_{21} = i(\delta_1 - \delta_2)\tilde{\rho}_{21} + \frac{i}{2}\Omega_1\tilde{\rho}_{23} - \frac{i}{2}\Omega_2\tilde{\rho}_{31} \quad (4.6f)$$

where $\delta_i = \omega_i - \omega_{3i}$ for $i = \{1, 2\}$ is the laser detunings. Only equations for half of the coherences terms are listed above; the other half are simply the complex conjugate of Eqs. (4.6d) to (4.6f) since $\tilde{\rho}_{ij} = \tilde{\rho}_{ji}^*$.

Quantum interference in this three-level system is established through the coherence between $|1\rangle$ and $|2\rangle$. In Eq. (4.6d), for instance, the coherence $\tilde{\rho}_{31}$ is due to not only the corresponding laser excitation $i\Omega_1(\tilde{\rho}_{33} - \tilde{\rho}_{11})/2$, but also the interaction between the other laser and the ground states' coherence $-i\Omega_2\tilde{\rho}_{21}/2$. It is easy to see that, only the real part of $\tilde{\rho}_{21}$ contributes to the quantum coherence, while the imaginary part acts like the decoherence term. Therefore, from Eq. (4.6f), a two-photon resonance condition is

found when $\delta_1 = \delta_2$. At this condition, the steady state population distribution is

$$\rho_{11} = \tilde{\rho}_{11} = \frac{\Omega_2^2}{\Omega_1^2 + \Omega_2^2} \quad (4.7a)$$

$$\rho_{22} = \tilde{\rho}_{22} = \frac{\Omega_1^2}{\Omega_1^2 + \Omega_2^2} \quad (4.7b)$$

$$\rho_{33} = \tilde{\rho}_{33} = 0 \quad (4.7c)$$

where there is no excitation state population even the two lasers continuously interact with the system. The coherence ρ_{31} and ρ_{32} also vanish:

$$\rho_{31} = \tilde{\rho}_{31} e^{-i\omega_1 t} = 0 \quad (4.8a)$$

$$\rho_{32} = \tilde{\rho}_{32} e^{-i\omega_2 t} = 0, \quad (4.8b)$$

but there is coherence between two ground states:

$$\rho_{21} = \frac{-\Omega_1 \Omega_2}{\Omega_1^2 + \Omega_2^2}. \quad (4.8c)$$

At the CPT resonance, the population is in the following quantum superposition:

$$\frac{\Omega_2}{\sqrt{\Omega_1^2 + \Omega_2^2}} |1\rangle - \frac{\Omega_1}{\sqrt{\Omega_1^2 + \Omega_2^2}} |2\rangle. \quad (4.9)$$

The coherent population trapping can be easily observed with the trapped single Ba^+ , as shown in Fig. 4.4. The width of the resonance primarily depends on the Rabi frequencies of the lasers. However, the width in Fig. 4.4 is wider than expected as it is broadened due to the laser linewidth. The Zeeman shift also contributes to the width by a

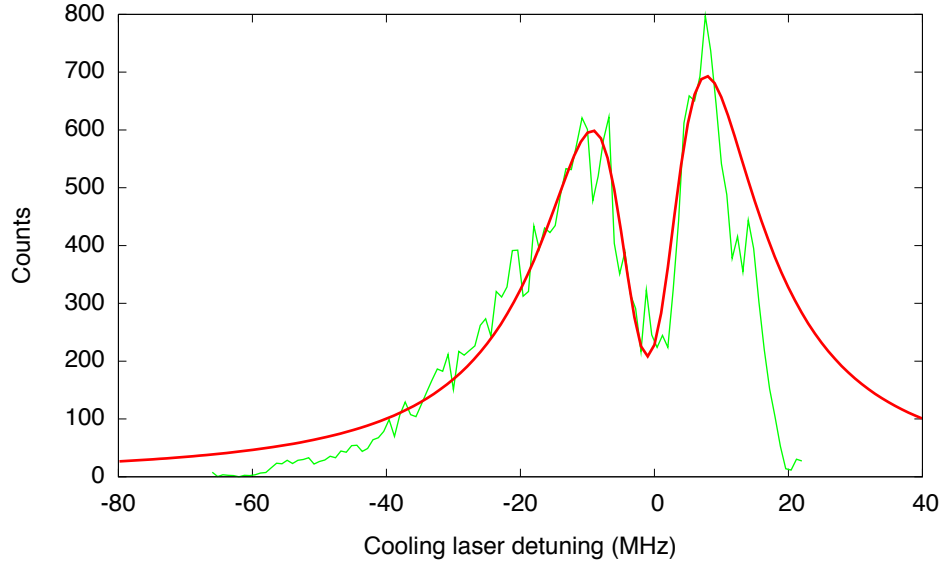


Figure 4.4. CPT resonance observed by the laser-induced spectroscopy of Ba^+ .

small amount. In order to avoid the CPT resonance during the laser cooling process, the 650 nm laser is actually set to blue detuned to the corresponding transition's resonance.

A note to the decoherence terms. Other phenomenological sources of relaxation can be added to the decoherence matrix $\{\partial\rho/\partial t\}$ if necessary. For instance, decoherence due to the finite laser coherence can be written as

$$\begin{pmatrix} 0 & 0 & -\gamma_1\rho_{13} \\ 0 & 0 & -\gamma_1\rho_{23} \\ -\gamma_1\rho_{31} & -\gamma_2\rho_{32} & 0 \end{pmatrix} \quad (4.10)$$

[check check check] where γ_1 and γ_2 are the linewidths of the laser. To describe relaxation from $|2\rangle$ to $|1\rangle$ at rate γ , add the following term to $\{\partial\rho/\partial t\}$:

$$\begin{pmatrix} \gamma\rho_{22} & -\frac{\gamma}{2}\rho_{12} & 0 \\ -\frac{\gamma}{2}\rho_{21} & -\gamma\rho_{22} & 0 \\ 0 & 0 & 0 \end{pmatrix}. \quad (4.11)$$

In reality, Ba^+ has Zeeman sublevels in each state. The theoretical study can be carried out in a similar manner. When the sublevels degenerate, the system is much similar to the three-level case. When the degeneracy is lifted by, say, the magnetic field, the system becomes an ensemble of multiple three-level CPT systems.

4.3. Laser Cooling

Cooling of a single ion's motion is done in two stage. The Doppler cooling technique brings the ion from room temperature to the so-called Doppler limit, which is of order $100\ \mu\text{K}$. The ion is further cooled to the ground state of the trap by means of sideband cooling. For the projects in this thesis, Doppler laser-cooled ion is sufficient. Motional ground state cooling is required ultimately for the precision spectroscopy experiment. Ground-state cooling of a single barium ion by two-photon Raman transition has recently been demonstrated in Seck *et al.* (2016) by other members in the laboratory.

Doppler laser cooling has become a standard technique in many atomic and molecular physics experiments, hence I will skip the introduction to this technique. We laser cool the trapped barium ion over the $6S_{1/2} \rightarrow 6P_{1/2}$ transition with the 493 nm laser, while the population is being repumped from the $5D_{3/2}$ by the 650 nm laser. As mentioned earlier, this Λ system could result in the coherent population trapping when the detunings of the

two lasers are similar. Therefore, we can not have both lasers red detuned. Only the 493 nm laser is red detuned; the 650 nm laser is set to resonant with or blue detuned to the $5D_{3/2} \rightarrow 6P_{1/2}$ transition to avoid the CPT. See, e.g., Marzoli *et al.* (1994); Lindberg and Javanainen (1986) for more discussions on laser cooling of a three-level system.

In passing, the issue can be avoided by doing incoherent repumping. In addition to using an incoherent 650 nm source, the repumping can be done via the $6P_{3/2}$ excitation state. However, since spontaneous emission from $6P_{3/2}$ to $5D_{5/2}$ is allowed, repumping on that transition is also required. Thus, two repumping lasers are required in this scheme.

Cooling Limit

The Doppler-limited temperature is

$$T_D = \frac{\hbar\Gamma}{2k_b} \quad (4.12)$$

and is achieved when the laser detuning is $\delta = -\Gamma/2$ but independent to the laser intensity (Wineland and Itano, 1979). However, when the ion is first loaded into the trap, it can have quite a high velocity such that the Doppler shift is too large for most of the time to have sufficient photon scattering. Thus, laser cooling can be very slow initially. We then sometimes further detune the laser to accommodate the large initial high temperature. We also increased the laser intensity to have a larger scattering rate. When the ion becomes colder, the laser is set to $\delta = -\Gamma/2$ and $I \approx I_s$ with I_s being the saturation intensity for the best Doppler cooling.

Consider the quantum motion of the trapped ion, the mean occupation number of the motional state in the trap of secular frequency ω is given by (Wineland *et al.*, 1987;

Stenholm, 1986)

$$\bar{n} = \frac{1}{\exp(\hbar\omega/k_B T) - 1} = \frac{1}{\exp(2\omega/\Gamma) - 1} \quad (4.13)$$

at the Doppler-limited temperature T_D . $\bar{n} = 7.0$ when $\omega = 2\pi \times 1$ MHz along the trap axis. Additionally, the low occupation number means that the ion is sufficiently in the Lamb-Dicke regime where ground state cooling can be performed by driving sideband transitions.

4.4. Photon Counting - Time Correlation

Laser-induced fluorescence measurement allows us to detect the existence and the state of the trapped barium ion. In this project, the fluorescence photon is collected by both a camera and a photomultiplier tube (PMT). While the camera provides spatial resolution, the PMT provides an excellent time domain resolution.

Fluorescence Modulation

In my single ion experiment, I searched for the time domain patterns of the fluorescence to determine the motion of the trapped Ba^+ . This idea is applied to both the secular oscillation and the RF-related micromotion. The fluorescence rate is the product of the excitation state population P_e and the spontaneous emission rate Γ . For the simplicity, we consider a stationary two-level atom whose excited population is a Lorentzian function of the detuning δ . Thus, the fluorescence rate is

$$R(\delta) = \Gamma P_e(\delta) = \frac{\Gamma}{2} \frac{s}{1 + s + 4\delta^2/\Gamma^2} \quad (4.14)$$

where $s = I/I_s$ is the saturation parameter. As the ion oscillating with velocity amplitude v_0 and frequency ω , the detuning experienced by the ion is shifted by the first order Doppler shift:

$$\delta = \delta_0 + v_0 \cos \omega t / \lambda \quad (4.15)$$

with δ_0 being the laser detuning and λ being the wavelength of the transition. The ion's periodic motion hence modulates the fluorescence as $R(\delta_0 + v_0 \cos \omega t / \lambda)$. The response of fluorescence modulation depends on the laser detuning δ_0 and the amplitude v_0 . The modulation is linear in the ion's motion when the laser detuning δ_0 is away from the transition resonance and the corresponding Doppler is small. In this regime, the modulation index, the coefficient of the $\cos \omega t$ term normalized to the constant term, is

$$h = \frac{R'(\delta_0)}{R(\delta_0)} \frac{v_0}{\lambda} = -\frac{8\delta_0/\Gamma}{1 + s + 4x^2/\Gamma^2} \frac{v_0}{\lambda\Gamma}. \quad (4.16)$$

It is straightforward to find the maximum modulation

$$h = \mp 2v_0 / \sqrt{1 + s} \lambda \Gamma \quad (4.17)$$

at $\delta_0 = \pm \sqrt{1 + s} \Gamma / 2$. The \pm sign indicates the phase of fluorescence modulation, which is differed by π when the laser is switched from red detuned to blue detuned, and vice versa.

The second order term in the modulation is a second harmonic term as $\cos^2 \omega t = (1 + \cos 2\omega t) / 2$. With the definition of the modulation index in Eq. (4.17), the strength of the second order term is $R''(\delta_0) / R(\delta_0) = h^2 / 2$ regardless the sign of δ_0 . The third order coefficient is zero. Therefore, the fluorescence rate of an oscillating ion driven around

$\delta_0 = \sqrt{1+s}\Gamma/2$ can be expressed as

$$R = \frac{s\Gamma}{2(1+s)} \times \left(\left(1 + \frac{h^2}{4}\right) + h \cos \omega t + \frac{h^2}{4} \cos^2 \omega t \right). \quad (4.18)$$

Correlation Measurement

Experimentally, the modulation of the fluorescence is measured simply by recording the fluorescence strength as a function of time. This measurement, however, is less straightforward for the single ion experiment due to the low photon collection efficiency. Consider the typical experiment condition where the collection efficiency is 10^{-4} and the spontaneous emission rate $\Gamma = 9.5 \times 10^7 \text{ s}^{-1}$ for the $6P_{1/2} \rightarrow 6S_{1/2}$ decay channel in the Ba^+ . The photon flux is then of order $10^{-4}/\text{s}$, which is low compared to the trapped ion's oscillation frequency in the MHz range. Therefore, the arrival time (at the detector) of each fluorescence photon is recorded instead, and the correlation of the time series is computed to find modulations in the photon flux.

Since for either application, detecting micromotion or secular motion, the oscillation frequency ω is known, it is convenient to measure the cross-correlation function between the photon flux and $\cos \omega t$. This measurement is approximated by measuring the histogram of photon counts for various phases of the oscillation. The period of the oscillation is divided into 10 to 20 counting bins, and the histogram is fitted by Eq. (4.18) to determine the modulation index, which can be further converted to the velocity. In practice, including only the first order term $\cos \omega t$ in the fitting function is sufficient representative in most applications. The correlation measurement is usually limited by the photon shot

noise. A good signal-to-noise ratio requires the shot noise in each counting bin being smaller than the modulation to be observed.

Autocorrelation

When the oscillation frequency is unknown, one can compute the autocorrelation function to find the motion. As the fluorescence photons are tagged with their arrival time, the computation of the autocorrelation function becomes statistics on the delay times between any two photons. Unlike the cross-correlation which measures a single frequency, the autocorrelation method measures a large frequency range simultaneously but requires much more data from photons. See Sheridan and Keller (2011) for an application example.

4.5. Micromotion compensation

Micromotion, introduced in Eq. (2.9), is the forced oscillation driven by the trapping RF electric field in the Paul trap. As the micromotion amplitude is proportional to the secular motion (the location of the ion), the micromotion vanishes only when the ion is rest on the RF field null, which defines the trap center.

The negative impact due to the micromotion is two folds. First, the motion causes the Doppler shift, which is a systematic error in the precision spectroscopy. Also, the electronic noise in the RF field can disturb the ion's secular motion through the micromotion. This randomness is thus a heating source for ions in an RF trap. RF field heating coupled by micromotion is particularly a concern for a large number of ions due to the spatial extent. Thus, it is necessary to minimize excessive micromotion; the procedure is called the micromotion compensation.

Compensation: by Imaging

A single ion is pushed away from the trap center by the DC electric field due to stray charges and patch potentials. By biasing the trap electrodes, this field can be canceled locally such that the ion is trapped around the field null. In the laboratory, micromotion compensation is done in two stages. In the first stage, coarse compensation is done by monitoring the single ion's location on the camera while varying the strength of the RF field. The equilibrium point of a single ion depends on the strength of the trapping field except when it is at the field null. Therefore, if an ion is away from the trap center, varying the RF voltage will shift its location. However, when the stray field is properly compensated, the ion sits around the trap center and remains at the center for all RF voltage.

For a cloud of ions as in Chapter 7, micromotion compensation can be done in a similar manner. However, instead of monitoring the location of single ions, we adjust the compensation DC voltages until the center of mass of the cloud remains the same when sweeping the RF voltage.

Compensation: by Fluorescence Correlation

As mentioned in Section 4.4, the micromotion creates a modulation in the fluorescence, which can be detected by methods of correlation functions. Therefore, micromotion can be finely compensated by minimizing the modulation at the RF frequency in the fluorescence (Berkeland *et al.*, 1998). Figure 4.5 shows a typical fluorescence measurement cross-correlated with the trap RF drive signal. In this measurement, each photon counting bin is 5 ns wide, which divides an RF drive cycle into roughly 9 bins. The measured modulation index is $h = 0.25$, and thus from Eq. (4.17), the micromotion amplitude is

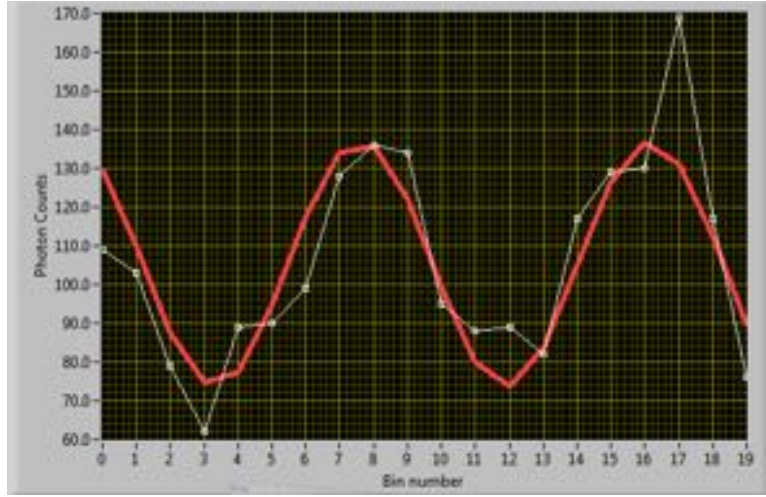


Figure 4.5. Detect micromotion by autocorrelation.

$v_0 = 11.7 \text{ m/s}$ while the fluorescence is induced by a laser of $\lambda = 493 \text{ nm}$ and $s \approx 1$; $\Gamma = 9.5 \times 10^7 \text{ s}^{-1}$. There is an addition factor of $\sqrt{2}$ multiplied into this result as the laser's direction is 45° with respect to the radial direction.

Figure 4.6(a) shows micromotion modulated amplitude for various applied DC voltage along one direction. In this measurement, excessive micromotion is minimized at 108 kV. In Fig. 4.6(b), the compensation voltage is recorded for 21 hours to demonstrate the drift. The trap condition can change quite frequently and hence in the future experiment, excessive micromotion needs to be checked constantly.

Other Methods

Compensation based on the ion's location or the fluorescence modulation are the two common approaches. Yet, Ibaraki *et al.* (2011) demonstrated micromotion compensation by means of parametric resonance. In this scheme, the parametric excitation is done by amplitude modulating the trapping RF voltage. When modulating at the secular

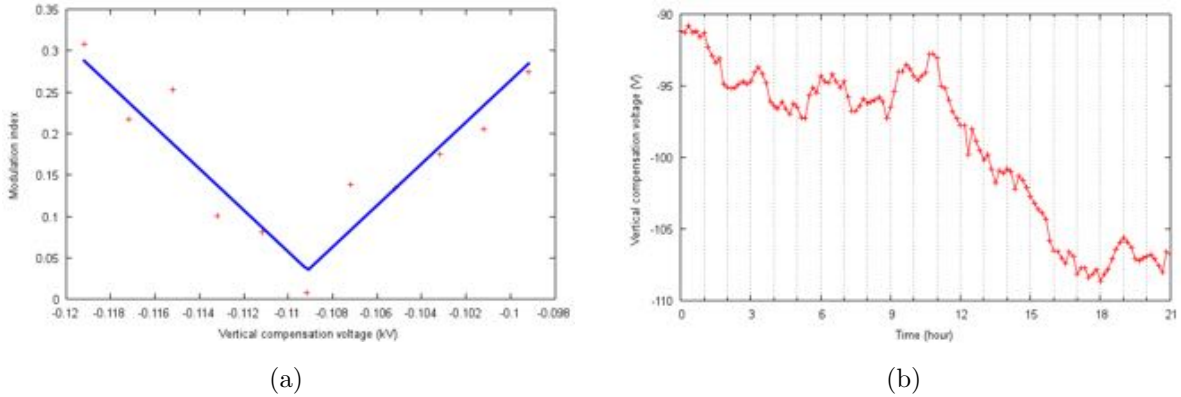


Figure 4.6. Micromotion amplitude as a function of bias DC

frequency, the ion's oscillation is resonantly excited unless it is at the RF null. Therefore, the parametric resonance can be used to detect excessive micromotion.

Finally, if the ion is in the Lamb-Dicke regime, sideband transitions due to the micromotion would be resolved. Hence, compensation is done by minimizing the corresponding sideband amplitude.

4.6. Secular Oscillation

This section talks about the characterization of the ion's secular motion, which provides preliminary information for the experiment presented in the next chapter as well as other applications. We especially focus on the measurement of the secular frequency in the axial (z) direction.

The secular frequency is probed by finding the resonance between the ion's motion and its external driving force. The simplest motional excitation is an AC electric field along the axial direction, which is provided by driving one of the endcap electrodes with an AC signal. The single ion is continuously laser cooled. When the ion's motion in the trap

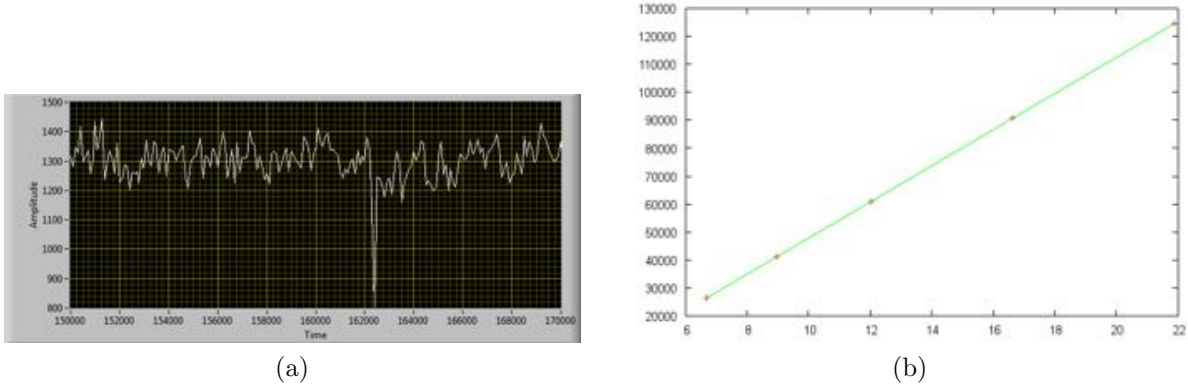


Figure 4.7. Tickling on end cap

resonants with the AC electric field, the oscillation amplitude quickly builds up such that the Doppler shift becomes too large for sufficient laser scattering. Thus the fluorescence rate drops at the resonance. Figure 4.7(a) shows a typical spectrum of the axial secular motion. The dropping of fluorescence at 203 200 kHz is identified as the axial secular mode. To further justify, the square of the resonance frequency for various endcap DC voltage V_{ec} is measured in Fig. 4.7(b) and a linear relationship is observed. The slope is $6774.9 \text{ kHz}^2/\text{V}$ and is equal to $\kappa_z e / (2\pi)^2 m z_0^2$ according to Eq. (2.8) with the correction of the geometric factor κ_z . Therefore, the geometric factor is measured to be $\kappa_z = 0.41$ with $z_0 = 0.95 \text{ mm}$ for this ion trap. The finite element analysis of this trap yields $\kappa_z = 0.54$. The discrepancy is most likely due to the dimensional error in the trap.

The trapped ion represents a high-quality mechanical oscillator and therefore presents a narrow linewidth in its motional spectrum. Although the ion is laser cooled during the measurement, damping due to the Doppler cooling is, in fact, negligible. Another source of damping is the resistance seen by the imaging charge. Finally, the spectral width is

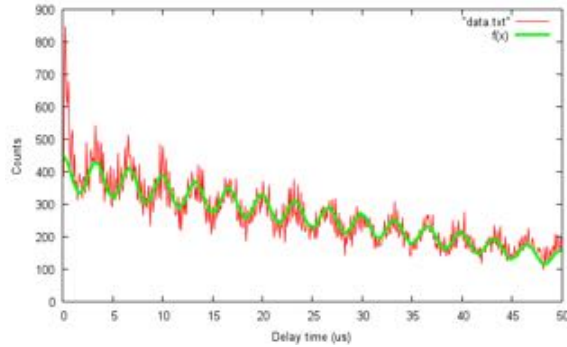


Figure 4.8. Autocorrelation function of the oscillating ion.

most likely due to the uncertainty of the secular frequency originated from the endcap voltage fluctuation.

The motional excitation can be provided by the light pressure as well. In this method, the cooling laser (493 nm) is amplitude modulated at a certain frequency to provide a periodic optical force. The shape of the modulation is less critical here; I simply apply the square wave modulation. The fluorescence of the ion integrated over multiple periods drops, as in the previous setup when the optical force resonantly excites the secular motion.

The secular motion can be probed by the photon correlation function introduced in Section 4.4 as well. To demonstrate, the ion is driven by a weak AC electric field as in the earlier experiment. The detected fluorescence photons are tagged with their arrival time and the autocorrelation function is computed. A typical result is shown in Fig. 4.8. There is an obvious oscillation with a period $3.3 \mu\text{s}$ coming from the secular motion. Furthermore, the amplitude of the oscillation has a decay time around $63 \mu\text{s}$. In Table 4.1, the frequency response obtained by means of photon correlation is shown.

Table 4.1. Frequency response

Drive frequency(kHz)	Measured period(μ s)	Measure frequency(kHz)	Modulation index
300.3	3.329(6)	300.390	0.023(4)
300.4	3.332(3)	300.120	0.040(4)
300.5	3.328(2)	300.480	0.084(4)
300.6	3.326(2)	300.661	0.059(4)
300.7	3.325(11)	300.751	0.012(4)

In the next chapter, we will convert the secular frequency measurement into an internal state readout protocol for the single ion spectroscopy experiment.

CHAPTER 5

Coherent Motion Single Ion State Readout

This chapter presents the development of state readout by coherent motion, which was published in Lin *et al.* (2013).

5.1. Motivation

The high quality of environmental isolation, storage time, and particle localization provided by ion traps creates an excellent environment for quantum control and precision spectroscopy (Leibfried *et al.*, 2003). To date, nearly all few-ion experiments have accomplished control and addressing by relying on laser-accessible closed-cycle optical transitions, which occur in only a small number of atomic ion species. An essential feature required for extending the power of ion traps to other atomic and molecular species is the ability to perform non-destructive internal state readout with a small or vanishing numbers of scattered photons (Schmidt *et al.*, 2006; Leibfried, 2012; Ding and Matsukevich, 2012; Mur-Petit *et al.*, 2012; Clark *et al.*, 2010). Ability to control and monitor new atomic and molecular ion species could open new possibilities in such areas as quantum information processing, parity-violation studies, search for time-reversal symmetry breaking, and search for time-variation of fundamental constants.

Here, we study the excitation of a Doppler-cooled single barium (Ba^+) ion in a harmonic trapping potential with negligible damping, under the influence of a resonantly pulsed radiation pressure force in the regime of few photon scattering. A pulsed radiation

pressure force, in the regime of large scattering numbers, has previously been used for few-ion mass spectrometry (Drewsen *et al.*, 2004). In modeling and experiment, we find that phase-locking behavior allows efficient energy transfer to the ion oscillator, such that scattering of order one hundred photons effectively separates the driven velocity from the Doppler-cooled distribution. Since motional excitation by photon scattering is conditional upon the ion’s internal state, a pulsed radiation pressure force could be used to transfer internal state information from a molecular or atomic spectroscopy ion with only a marginally closed-cycle transition onto a co-trapped logic ion used for state readout. State readout of a non-cycling spectroscopy ion has been accomplished by first reducing its temperature by laser-cooling a co-trapped logic ion, then using sophisticated protocols to map its internal state information onto detectable motion of the two-ion crystal (Schmidt *et al.*, 2005; Hume *et al.*, 2011). A pulsed radiation pressure force applied to a molecular or atomic spectroscopy ion with only a marginally closed-cycle transition could offer a new and simple means to accomplish the state mapping.

5.2. Pulse-Driven Oscillator

We treat the ion as an undamped oscillator because damping from radiation and resistive losses are negligible, and damping due to off-resonant photon scattering is also unimportant, as the ion motion is small in our experiment.

The equation of motion of a harmonic oscillator driven resonantly by a square pulse train is:

$$x''(t) + \omega^2 x(t) = F(t)/m. \quad (5.1)$$

In the above equation, $x(t)$ is the position of the oscillator at time t ; ω is the secular frequency of the oscillator; m is the mass. The driving force is a periodic function with period $T = 2\pi/\omega$ and for $0 < t < T$ it can be written as

$$F(x) = \begin{cases} \lambda, & 0 \leq t < DT \\ 0, & DT \leq t < T \end{cases} \quad (5.2)$$

with λ being the drive strength and D the duty cycle. Because the driven oscillator phase locks such that photon scattering transfers maximum energy (with ion velocity along the laser direction at the time of scattering,) excitation by a pulse train with small duty cycle D is more efficient per photon than excitation by a sinusoidally modulated radiation pressure force. For the moment neglecting stochastic aspects of photon scattering, the driving force λ is given by $\lambda = \hbar k \rho_e \Gamma / \sqrt{2}$, where k is the photon wave number, ρ_e is the excited state population, and Γ is the scattering rate. The $\sqrt{2}$ factor accounts for the 45° angle between the force and the motion in our experiment; $\lambda \sim 10^{-20}$ N for typical visible dipole transitions, with $\rho_e = 0.3$ determined experimentally.

To study Eq. (5.1) I first find the Green's function $G(t, t')$ of this system:

$$G(t - t') = \frac{1}{\omega} \Theta(t - t') \sin(\omega(t - t')) \quad (5.3)$$

where $\Theta(t - t')$ is the step function. The Green's function describes the response due to an infinitesimal kicking to the oscillator and is the solution to the following equation:

$$G''(t) + \omega^2 G(t) = \delta(t - t'). \quad (5.4)$$

By the Green's Theorem, the full solution to Eq. (5.1) can be expressed as

$$x(t) = A \sin(\omega t + \phi) + \frac{1}{m} \int_{-\infty}^t G(t-t') F(t) dt'. \quad (5.5)$$

Let's first consider the response due to only one pulse. By plugging Eq. (5.2) into Eq. (5.5) and carrying out the integration from $t = 0$ to DT , we obtain

$$x(t) = A \sin(\omega t + \phi) + \frac{2\lambda}{m\omega^2} \sin\left(\frac{\omega DT}{2}\right) \sin\left(\omega t - \frac{\omega DT}{2}\right).$$

Further let $\omega DT = 2\pi D \equiv \Theta$ and the above expression therefore becomes

$$x(t) = \left(A \cos \phi + \frac{\lambda}{m\omega^2} \sin \Theta \right) \sin \omega t + \left(A \sin \phi + \frac{\lambda}{m\omega^2} (\cos \Theta - 1) \right) \cos \omega t. \quad (5.6)$$

Namely, after the application of a single pulse,

$$x_0(t) = A \sin(\omega t + \phi) \rightarrow x_1(t) = A_1 \sin(\omega t + \phi_1) \quad (5.7)$$

for

$$A_1 = \sqrt{c_1^2 + c_2^2} \quad (5.8a)$$

and

$$\tan \phi_1 = c_2/c_1 \quad (5.8b)$$

with

$$c_1 = A \cos \phi + \frac{\lambda}{m\omega^2} \sin \Theta \quad (5.8c)$$

$$c_2 = A \sin \phi + \frac{\lambda}{m\omega^2} (\cos \Theta - 1) \quad (5.8d)$$

Hence, a recursive equation can be set up to account for each consecutive pulse from the pulse train. That is, a equation to describe the evolution

$$(A_0, \phi_0) \rightarrow (A_1, \phi_1) \rightarrow \cdots \rightarrow (A_n, \phi_n) \quad (5.9)$$

after the application of n pulses.

Phase Evolution

We are interested in the phase shift due to the pulse drive. Equation (5.8b) is explicitly

$$\tan \phi_1 = \frac{A \sin \phi + \frac{\lambda}{m\omega^2} (\cos \Theta - 1)}{A \cos \phi + \frac{\lambda}{m\omega^2} \sin \Theta}.$$

Now, write $\phi_1 = \phi + \delta$ and recall the following identity:

$$\begin{aligned} \tan \phi_1 = \tan(\phi + \delta) &= \frac{\tan \phi + \tan \delta}{1 - \tan \phi \tan \delta} \\ &= \frac{\sin \phi + \cos \phi \tan \delta}{\cos \phi - \sin \phi \tan \delta}. \end{aligned} \quad (5.10)$$

By comparing the above two expression, we can find that

$$\tan \delta = \frac{-2 \sin \Theta/2 \sin(\phi + \Theta/2)}{Am\omega^2/\lambda + 2 \sin \Theta/2 \cos(\phi + \Theta/2)}. \quad (5.11)$$

Note that the oscillator's phase eventually is locked to the drive at $\phi_c = -\Theta/2$. Therefore, to study the phase-locking mechanism, we write $\phi = \phi_c + \Delta = -\Theta/2 + \Delta$. When $\Delta \ll 1$, the above equation hence become

$$\tan \delta \approx \delta = -\frac{2 \sin \Theta/2}{Am\omega^2/\lambda + 2 \sin \Theta/2} \Delta \quad (5.12)$$

which describes a negative feedback between δ and Δ . By realizing $\delta = \Delta_n - \Delta_{n-1}$ at the application of the n -th pulse, Eq. (5.12) is therefore the recursion equation for Δ_n and the solution is

$$\begin{aligned}\Delta_n &= \left(1 - \frac{2 \sin \Theta/2}{Am\omega^2/\lambda + 2 \sin \Theta/2}\right)^n \Delta_0 \\ &= \left(\frac{Am\omega^2/\lambda}{Am\omega^2/\lambda + 2 \sin \Theta/2}\right)^n \Delta_0.\end{aligned}\tag{5.13}$$

The phase is locked to its final value exponentially in time with a time constant

$$\tau = T / \ln \left(1 + \frac{2\lambda \sin \Theta/2}{Am\omega^2}\right).\tag{5.14}$$

It is to see that a rapid phase-locking is provided by a strong drive, $\lambda \gg Am\omega^2$, and 50% duty cycle such that $\sin \Theta/2 = \sin \pi D = 1$.

Amplitude Evolution

Let's first find the condition for maximum amplitude growth. From Eq. (5.8a),

$$\begin{aligned}A_1^2 &= c_1^2 + c_2^2 \\ &= \left(A + \frac{2\lambda \sin \Theta/2}{m\omega^2}\right)^2 - \frac{4A\lambda}{m\omega^2} \sin \frac{\Theta}{2} \left(1 - \cos\left(\phi + \frac{\Theta}{2}\right)\right).\end{aligned}\tag{5.15}$$

The increment is maximized when the phase ϕ equals to

$$\phi_c \equiv \frac{-\Theta}{2} = -\pi D\tag{5.16}$$

and the growth is

$$A_1 - A = \frac{2\lambda \sin \pi D}{m\omega^2}.\tag{5.17}$$

In general, Eq. (5.15) can be approximated as

$$A_1^2 = A^2 + 2A\eta \cos \Delta \quad (5.18)$$

where $\eta = 2\lambda \sin(\pi D)/m\omega^2$ being much smaller than A in this experiment. In our experiment $\eta = 2.7$ nm and $A_0 \approx 34$ nm for a Ba^+ ion at the Doppler limit. With $A_1 = A + \Delta A$, we further obtain

$$\Delta A \approx \eta \cos \Delta, \quad (5.19a)$$

which is the recursion equation of the amplitude. Similarly,

$$\delta = \frac{-\eta}{A} \sin \Delta \quad (5.19b)$$

is the recursion equation of the phase.

By treating Eq. (5.19) as continuous in n and integrating, we find closed-form expressions:

$$A_n = \sqrt{(A_0 \sin \phi_0)^2 + (\eta n + A_0 \cos \phi_0)^2} \quad (5.20a)$$

$$\phi_n = -\cos^{-1}\left(\frac{\eta n + A_0 \cos \phi_0}{A_n}\right). \quad (5.20b)$$

The peak velocity of the oscillator after n cycles is then $V_n = \omega A_n$ and can be experimentally measured by the Doppler velocimetry introduced in Section 4.4 with extreme high sensitivity (Berkeland *et al.*, 1998; Biercuk *et al.*, 2010).

We compare 5.20 to a molecular dynamics simulation which takes the random timing and spontaneous emission angle of photon scattering into account. For the sample initial conditions and simulated scattering history shown in Fig. 5.1, the simulation differs

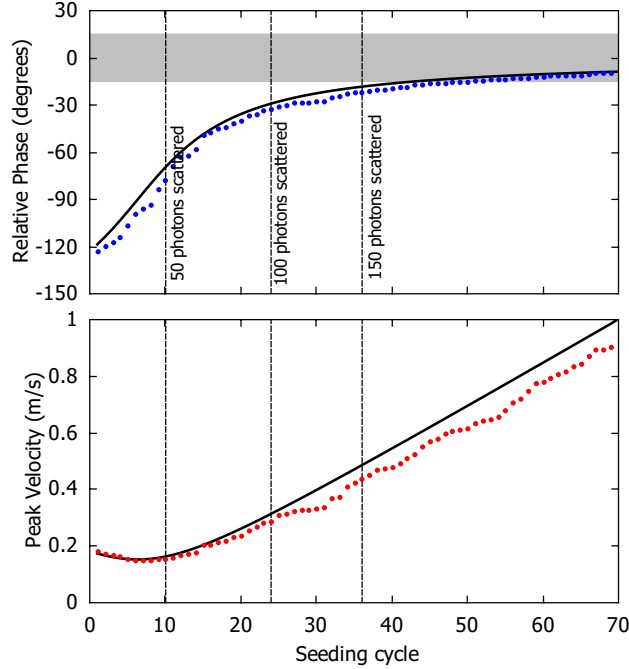


Figure 5.1. Modeled response of the Ba^+ oscillator to a pulsed drive with 10% duty cycle (gray band), with realistic drive parameter $\eta = 2.67$ nm, and initial conditions $\phi_0 = -122^\circ$ and $A_0 = 34$ nm ($V_0 = 0.2$ m/s), typical of Doppler cooling. Results from the simulation (points) deviate from the model of Eq. (5.20) (lines) because of noise in photon scattering.

slightly from the prediction, as the randomness inputs noise into the drive strength η and the driving phase ϕ . Also see Fig. 5.1 for the phase-locking behavior between the ion's oscillation and the driving force. We find that Eq. (5.20) describes the ensemble average from the simulation within the experimental uncertainty. Note that scattering of order 150 photons effectively separates the Ba^+ ion velocity from the initial thermal value.

5.3. Experimental Setup

While the experimental setup has been introduced in the previous chapters, here I summarize the important parameters. Our experimental investigation is performed with

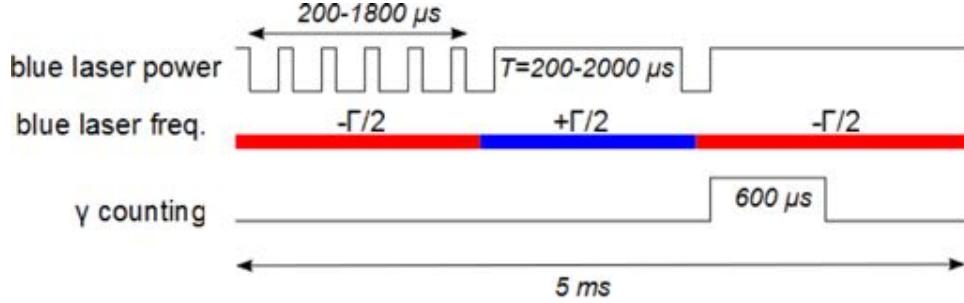


Figure 5.2. Experimental timing sequence.

a single $^{138}\text{Ba}^+$ along trap's axial mode with a secular frequency $\omega_z = 2\pi \times 926$ kHz. The manipulation of the ion is done by driving the blue $6S_{1/2} \rightarrow 6P_{1/2}$ transition (493.4 nm, $\Gamma_S = 2\pi \times 15.2$ MHz) and the red $5D_{3/2} \rightarrow 6P_{1/2}$ transition (649.7 nm, $\Gamma_D = 2\pi \times 4.9$ MHz). The two lasers are focused on the ion and co-propagate at 45° with respect to the trap z-axis. For Doppler cooling, we set the blue laser intensity to $2 I_{sat}$ with -15 MHz detuning; the red repumping laser intensity is $10 I_{sat}$, detuned by -20 MHz.

In order to detect few-photon seeded motion of the trapped ion, we use a motional amplification scheme, where a continuous-wave (CW) laser is blue-detuned from a cycling transition. See Section 5.4. Fluorescence from the ion is detected by a photomultiplier tube (PMT) with an overall efficiency of 0.1% including a bandpass filter transmitting only the blue light. We use an FPGA-based counter to perform photon statistics.

The major cycle of the experiment consists of seeding the motion, amplification, and resetting by Doppler cooling, as depicted in Fig. 5.2. To seed the ion motion, we chop the blue laser at the secular frequency ω_z ; the laser intensity is set to $10 I_{sat}$ with zero detuning; the seeding pulse train is applied for time t_s . The blue laser detuning is then set to 15 MHz for time t_a to amplify the seeded oscillation; $t_a = 10$ ms was chosen by experimental optimization. After amplification, the laser detuning is then set back to

–15 MHz to damp the excited ion. The repumping laser is not altered for each stage of the experiment. To detect the motion, we collect fluorescence from the last 4 ms of the amplification stage and the first 4 ms of the cooling stage. The above experiment cycle is repeated every 50 ms, and we integrate for 2 seconds to obtain the modulated fluorescence signal. These 40 cycles typically yield 1000 photon counts, collected by the FPGA into 20 timing bins of width 46.7 ns. Ion motion is detected as a modulation in photon arrival times with modulation amplitude h determined by fitting the correlation function $g(\tau)$ to $1 + h \cos(\omega_z(\tau - \tau_0))$ where τ is the time referenced to each secular motion cycle, and τ_0 compensates for constant experimental phase delays.

5.4. Coherent Motion Amplification

The seeded ion has a very small oscillation amplitude. For its motion to be detected by the fluorescence technique, the oscillation needs to be coherently amplified. We amplified the ion’s secular motion in the trap by laser scattering, based on the technique in Kaplan (2009); Vahala *et al.* (2009). This technique has been used to detect motion induced by electrostatic (Knünz *et al.*, 2010), radiation pressure (Sheridan *et al.*, 2012), and optical dipole forces (Hume *et al.*, 2011).

While the scattering of a red-detuned laser removes the momentum from the ion, a blue-detuned laser does the opposite. However, the blue-detuned laser does not add momentum to the ion randomly. As the ion has a secular oscillation, the scattering rate is modulated and thus the corresponding radiation pressure is modulated as well. Therefore, the ion, in fact, sees a periodic driving force due to the laser scattering. Since the periodic drive is in phase with the oscillation, it amplifies the motion coherently. The mechanism

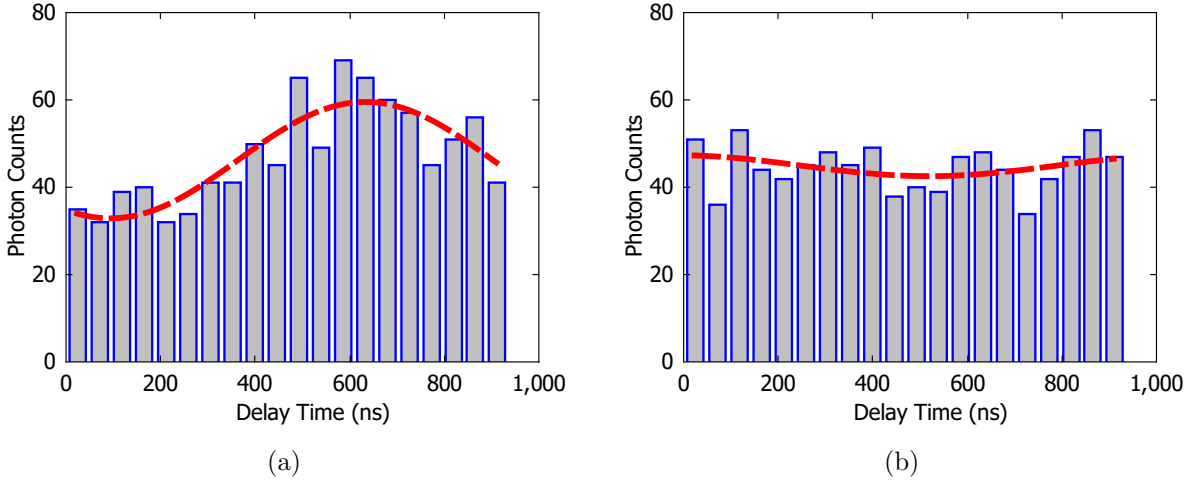


Figure 5.3. Fluorescence modulation. (a) The ion is bright to the seeding laser. (b) The ion is dark to the seeding laser.

is quite similar to the Doppler velocimetry, which is based on the fluorescence modulation, but the momentum transfer due to photon scattering is considered here.

It is straightforward to see the best amplification occurs when the detuning is the spectrum's half width at the half maximum, just like in the Doppler velocimetry. The amplification time needs to be experimented such that the motion is not over amplified. Chen *et al.* (2015) discussed the coherent motion amplification of a three-level particle.

5.5. Experiment Results

We first investigate the effect of pulse width on seeding, maintaining a constant average number of scattered photons. Figure 5.4 shows the modulation amplitude for different seeding pulse duty cycles, with the seeding time t_s is adjusted to keep fixed the laser-ion interaction time $D \times t_s$. We observe a stronger excitation for a shorter duty cycle as predicted by Eq. (5.20) normalized to the scattering number. The fitting model is an ensemble average over the initial phases ϕ_0 . We treat the coherent amplification as a

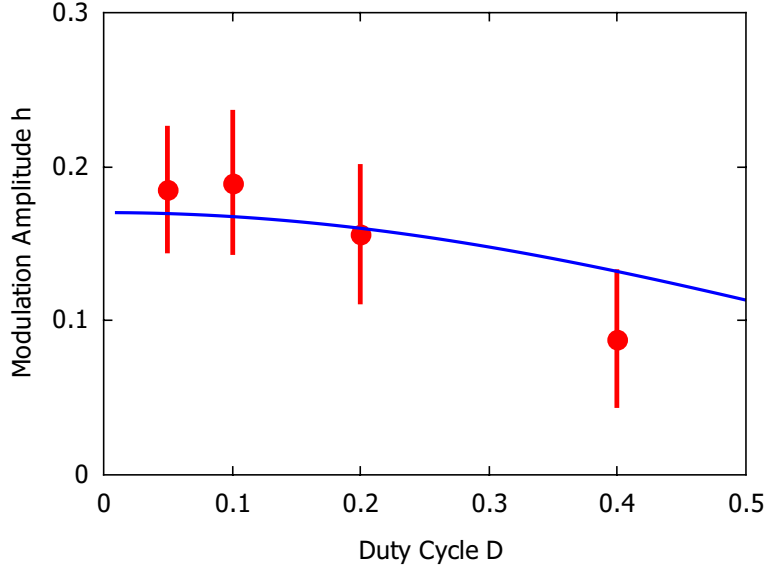


Figure 5.4. Measured modulation amplitude mean (points) and standard deviation (bars) versus seeding duty cycle, with seeding time varied to maintain $D \times t_s = 4 \mu\text{s}$; data were collected over 30 trials. Averaging Eq. (5.20) over initial phases and fitting for amplification-stage gain yields the solid curve.

constant velocity gain g_a (here $g_a = 2$), found from a single-parameter fit to the data, and then convert the amplified ion velocity into modulation amplitude according to a Lorentzian spectrum using an experimentally determined full-width-half-maximum of 30 MHz. The deviation between the experiment and the theory is attributed to the known variation of the amplification gain as the laser frequencies drift during the experiment.

Figure 5.5 shows the measured modulation amplitude versus seeding time, using $D = 0.1$, with the predicted response from Eq. (5.20) and a single-parameter fit for amplification gain (here $g_a = 2.7$.) Due to the initial distribution of oscillator phases, the model predicts slow ensemble-averaged velocity buildup at short times, until some degree of phase locking has occurred (see also Fig. 5.1.) The time scale for phase-locking

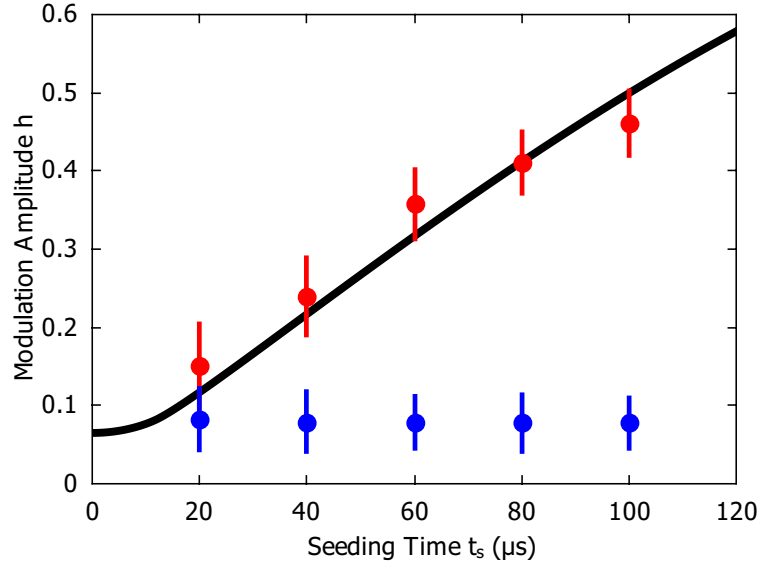


Figure 5.5. Modulation amplitude versus seeding time, when the seeding pulses excite an S-state ion (red), and when the ion is shelved in the D-state (blue). Each point is the average of 30 measurements, with the vertical bars showing the distribution standard deviation (rather than the error on the mean). The predicted response (black curve) is from Eq. (5.20), fitting for amplification-stage gain.

is given by $A_0/\eta \approx 13$ cycles, or $14 \mu\text{s}$ in this work. Once the phase is locked, all the photon momentum contributes to secular motion excitation coherently. Since the oscillation converts to fluorescence modulation approximately linearly, modulation amplitude goes linearly with the seeding time for a phase-locked oscillator.

5.6. Spectroscopy Application

We now consider the application of our pulsed seeding technique to internal state read-out by mapping the internal state onto ion motion. Figure 5.5 also shows the response from an unseeded ion, obtained by optically pumping into the $D_{3/2}$ state before seeding pulses are applied; before amplification, the ion is repumped to the $S_{1/2}$ state. In the

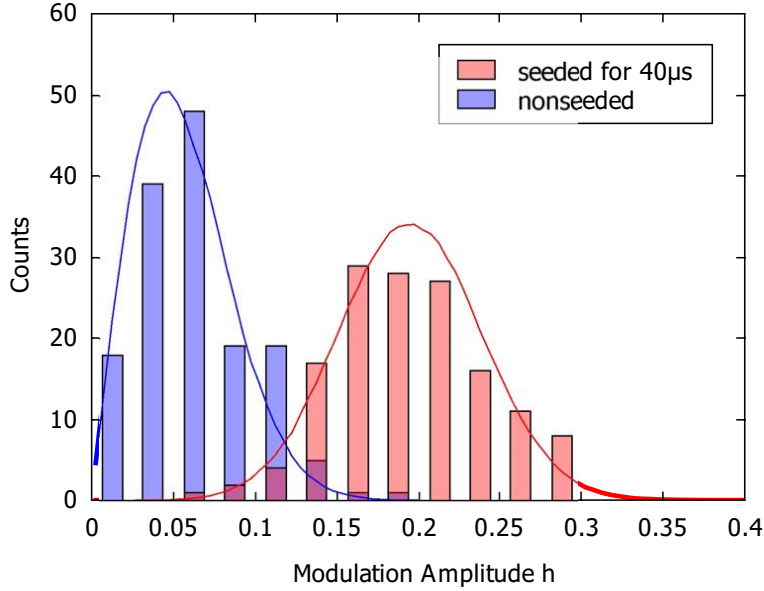


Figure 5.6. Distribution of the modulation amplitudes, measured after seeding the motion for 40 μ s (red histogram) and for an unseeded ion (blue histogram). The simulation (solid curves) accounts for noise in ion dynamics and shot noise in detection. Amplification gain is the single fit parameter.

context of a spectroscopy experiment, (failed) seeding from the $D_{3/2}$ state simulates state readout after a successfully driven spectroscopy transition, while (successful) seeding from the $S_{1/2}$ state simulates state readout after a failed spectroscopy transition (or vice versa.) Based on the magnitude of the dark state baseline, seeding for $t_s \approx 40 \mu$ s is sufficient to create Ba^+ motion well separated from the noise floor after amplification and our integration over 40 excitation/detection cycles. For this seeding time, there are approximately $n_\gamma = 150$ photons scattered per excitation cycle, and the measured fluorescence modulation is $\bar{h} = 0.24$. In Fig. 5.6 we show the experimental h distributions for seeded and unseeded ions, again using $D = 0.1$, along with the simulated results (with $g_a = 2.5$ the only fit parameter) accounting for various noise sources summarized in Table 5.1.

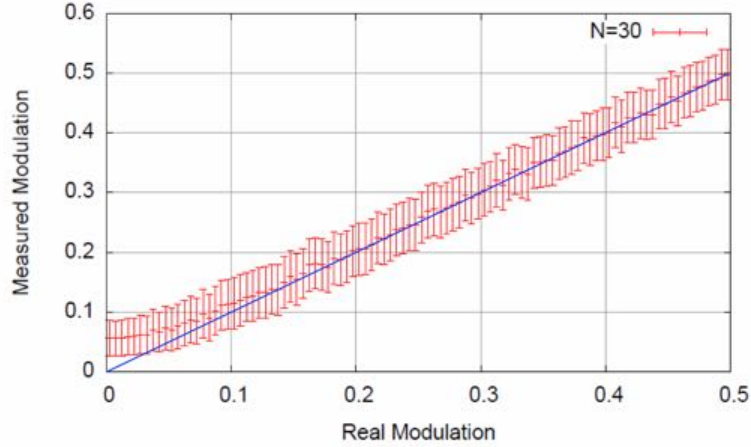


Figure 5.7. Determination of modulation index from data with 30 average counts per bin.

5.7. Error Sources and Improvement

In our experimental implementation, the major source of noise is low photon detection efficiency. Photon shot noise propagates through the data analysis and contributes to the width. For example, Fig. 5.7 shows the determination of the modulation index based on data that has on average 30 counts per bin. One can see that, with such low photon counts, $h = 0.1$ is roughly the detection limit.

In addition to the seeding noise already discussed, the coherent amplification processes injects noise into the ion motion, as the photon scattering has random spatial and temporal components. In Table 5.1 we model this noise term as a random walk in velocity space, $(\Delta v)^2 \approx v_r^2 \rho_e \Gamma t_a$, where $v_r = \hbar k/m$ is the recoil velocity and $\rho_e \approx 0.02$ during amplification. Overall, the summarized error sources characterize our state-detection uncertainty and form the distribution in Fig. 5.6. If we discriminate whether the ion's motion is excited by a threshold value $h_{th} = 0.12$, where the two distributions intersect, the false positive rate is estimated to be 3.2% and the false negative rate is 3.8%.

Table 5.1. Modeled contribution of various noise sources to the distribution width of the modulation amplitude, for $n_\gamma = 150$ yielding $\bar{h} = 0.20$. Data is integrated over N excitation/detection cycles, with initial ion temperature 360 μK , $t_s = 40 \mu\text{s}$, $t_a = 10 \text{ms}$, and $g_a = 2.5$. For $N = 1$, consider only the noise intrinsic to ideal single-shot excitation, say, for perfect fluorescence collection or for sustained oscillation during detection. For $N = 40$, there are 1000 fluorescence photon counts spread over 20 timing bins. The last line represents the quadrature addition of all sources.

Source	$\Delta h, N = 1$	$\Delta h, N = 40$
Photon counting	0	0.043
Initial thermal motion	0.072	0.011
Seeding stage	0.032	0.005
Amplification stage	0.114	0.018
Total width	0.139	0.048

Note that the measurement uncertainty is reduced by $N^{-1/2}$ after integrating over N excitation/detection cycles. ($N = 40$ in this work.) However, the required number of photons for state discrimination is then $N \times n_\gamma$, where $n_\gamma \approx 150$ is the seeding photon number required here. Currently, we perform detection while the ion velocity is either being amplified or cooled. An important improvement, which would eliminate the need to integrate over $N > 1$ excitation cycles, would be to simultaneously damp and amplify the oscillation with both the cooling and the repumping laser to achieve self-limiting sustained large-amplitude oscillation (Vahala *et al.*, 2009; Knüenz *et al.*, 2010). The number of scattered photons required for seeding the motion could also be reduced by a factor of $\sqrt{2}$ by sending the laser along the trap axis, making the photon momentum parallel to the secular motion direction. The detection sensitivity could also be enhanced by measuring the modulation amplitude with lock-in technique and increasing the photon detection efficiency (Streed *et al.*, 2011; Shu *et al.*, 2010). Seeding a lighter ion would require fewer scattered photons, as the ratio of recoil to thermal velocity goes as $m^{-1/2}$.

5.8. Outlook

If the trap is loaded with both a spectroscopy ion (used for the seeding stage) and a fluorescing logic ion (used first to Doppler cool the two-ion system then later in the amplification/detection stage), this state discrimination method can be applied to spectroscopy experiments. Further study of seeding behavior in a 2-ion crystal is required, but we expect approximately a degradation factor of 2 from the 1-ion seeding efficiency, to account for excitation of additional non-detected normal modes.

It is instructive to compare this state readout approach to other protocols using a co-trapped spectroscopy and logic ion. Quantum logic spectroscopy (Schmidt *et al.*, 2005) does not use spectroscopy ion scattering, but places restrictions on transition linewidth and wavelength, also requiring ground state cooling and logic ion shelving. Coherent excitation by an optical dipole force (Hume *et al.*, 2011) also does not scatter from the spectroscopy ion and relaxes ground-state cooling and shelving constraints, but it requires a suitable transition and challenging alignment of counter-propagating beams onto a dark ion. Our pulsed-excitation method does not require ground state cooling or shelving, can in principle be applied to any transition, and is quite simple to implement; however, it is limited to spectroscopy species with partially closed-cycle transitions allowing repeated scattering. Finally, sympathetic heating spectroscopy (Clark *et al.*, 2010) uses non-modulated spectroscopy ion scattering, requiring much more scattered photons than the phase-coherent approach described here.

To conclude, we have modeled and experimentally studied the state-dependent excitation of a single-ion oscillator impulsively driven at the trap frequency. Rapid phase-locking behavior results in efficient energy transfer; scattering approximately $n_\gamma = 150$

photons effectively separates the bright and dark state velocity distributions. However, our detection method is currently inefficient, requiring $N = 40$ excitation/detection cycles to build up photon statistics, such that 6000 scattered photons are currently needed to determine the internal state. Implementation of sustained amplification with phase-sensitive detection, along with other technical improvements discussed above, could reduce scattering to the small number (order 100 and $N = 1$) required to make a seeded excitation detectable above the thermal and scattering noise. With a co-trapped fluorescing ion used for the amplification and detection, this motional seeding technique could be useful in spectroscopy experiments on molecular ions with semi-closed transitions (Lien *et al.*, 2011; Nguyen and Odom, 2011; Nguyen *et al.*, 2011), atomic ions with slow cycling transitions, and in bichromatic force schemes where cycling is enhanced by stimulated emission (Voitsekhovich *et al.*, 1989; Grimm *et al.*, 1990; Chieda and Eyler, 2011). This resonant impulsive excitation technique could also be used to coherently excite selected normal modes of larger trapped ion crystals.

CHAPTER 6

Apparatus for the Molecular Ion Trap

This chapter introduces the apparatus for studying the internal state cooling of molecular ions, specifically the silicon monoxide cation or SiO^+ . Part of the apparatus used in this project is common to those in the single ion project. The main difference is the trap itself, the laser systems, and the detecting method.

In this molecular cooling project, an ion cloud is trapped in a centimeter-scale linear Paul trap. A larger number of ions provides larger signal and thus makes data collection faster when researching molecules. The lasers used to manipulate the molecular ion are usually in the UV wavelengths; some of the lasers are high power pulsed lasers. Detecting trapped molecular ions with fluorescence is harder because of the lack of cycling transitions. Hence, we turned to the mass spectroscopy.

6.1. The Molecular Ion Trap**Geometry**

This larger scale ion trap is also a linear Paul trap. Refer to Fig. 6.1 for the trap's outline. The trap has four stainless steel rods as the electrodes for the RF field. These electrodes can be biased each with a different voltage for the micromotion compensation or other applications. The endcaps are tube electrodes such there the axial clearance for lasers. These electrodes are mounted on two macro pieces, and the trap assembly is mounted on a vacuum blank flange attached to the chamber.

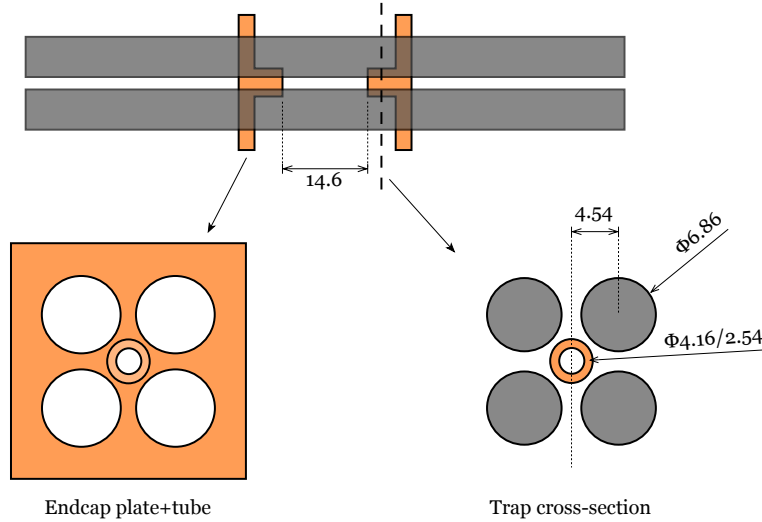


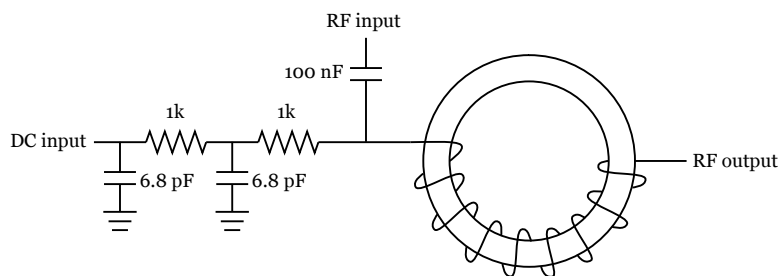
Figure 6.1. Molecular ion trap outline

This trap has $r_0 = 3$ mm and $z_0 = 7.3$ mm; the geometric factors are $\kappa_r = 0.25$ and $\kappa_z = 0.42$ obtained from the trap potential simulation (Appendix B.2).

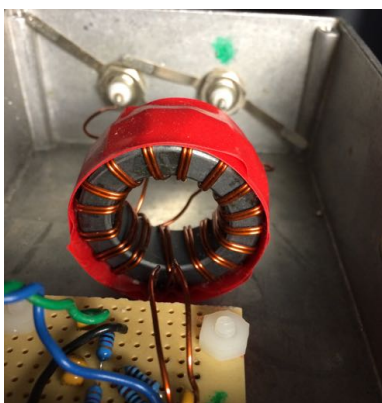
RF Source

The molecular ion trap is driven at a lower AC frequency such that with tangible voltage. For this trap geometry, a few hundred volts at 2 to 4 MHz is able to provide simultaneously trapping of species we are interested in, such as Si^+ , SiO^+ , and Ba^+ . Either the coaxial or the helical resonator is not suitable for this application since the physical size of the resonator is unrealistically large for 2 to 4 MHz. Instead, we build an inductor-capacitor (LC) resonance circuit to generate the high voltage for the trap.

The LC circuit is shown in Fig. 6.2(a). Like the other trap, the capacitance in the circuit is mainly from the trap itself and contact connections such as at the vacuum electrical feedthroughs; in practice, we expect of order 100 pF capacitance. For a resonance



(a) Schematic.



(b) The inductor.

Figure 6.2. RF source with toroidal inductor.

at 2 to 4 MHz, the required inductance is 15 to 60 μH and is realized often by a ferrite toroid coil.

Ferrite is a ferromagnetic ceramic material that has a large relative magnetic permeability $\mu_r = \mu/\mu_0 = 10^3$ at frequencies from DC to a few MHz. Beyond this range, the ferromagnetic response quickly rolls off as the phase between the magnetic field and the magnetization becoming larger. The out-of-phase ferromagnetic response not only reduces the permeability but also become resistive, so it is important to choose a ferrite core that can operate at the desired drive frequency. Two interesting references regarding ferrite materials are Goldfarb and Bussey (1987); Ott *et al.* (2003).

The specification of the toroid inductor can be estimated based on

$$L = \frac{\mu N^2 A}{l} \quad (6.1)$$

where L is the inductance, μ is the permeability of the core, N is the number of turns in the coil, A is the area of the coil cross-section, and l is the length of the coil. However, as other parameters such as the capacitance is known less accurately, the dimension of the inductor (usually the coil's number of turns) is oftentimes adjusted until the desired resonant frequency is obtained. Figure 6.2(b) shows the ferrite toroid inductor used in this molecular ion trap RF electronics.

The driving signal is capacitively coupled into the circuit through the 100 nF capacitor in Fig. 6.2(a). This configuration allows us to add a DC voltage to the electrode for creating a DC electric field in the radial direction. Two of the RF electrodes (from one diagonal pair) are each connected to one circuit; the two inductors from each copy of the circuits, however, share the same ferrite core and are built as matched as possible so the RF voltages on both electrodes can be the same.

The response of the LC resonant circuit is probed simply by measuring the voltage at the inductor's output end, which is connected to the trap electrode directly. With a few watts of pump power, several hundred volts can be generated at the electrodes. It is, however, not possible to generate higher voltages in this circuit with more pump power as the response saturates. This is due to the magnetic saturation of the ferrite core. Also, the RF amplifier is no longer linear at high output.

As in the single ion trap electronics, there is a low-pass filter each between the DC voltage supply and the electrode. The RC low-pass filter uses $R = 1 \text{ k}\Omega$ and $C = 6.8 \text{ nF}$, which has a 3 dB frequency of 23.4 kHz.

6.2. Lasers

The lasers for cooling barium ions were described in Section 3.4. This section will cover other laser systems for manipulating SiO^+ .

Continuum Mini-Lite

This is a low power pulsed Nd:YAG laser that outputs 10 ns pulses at 10 Hz repetition rate. The 1064 nm and the second harmonic 532 nm outputs are used in the laser ablation process for atomic or molecular source generation. The fourth harmonic 266 nm UV output is an easy solution to get energetic photons in the ionization or dissociation process.

Spectra-Physics Quanta-Ray YAG

This is high power ($>750 \text{ mJ}$ per pulse at 532 nm) is the pump source for the pulsed dye lasers or the optical parametric oscillator (OPO) lasers.

Spectra Physics Sirah Dye Laser; Lambda Physik Dye Laser

These lasers provide light sources for resonantly driving transitions in the SiO and SiO^+ . The selective transitions are used in the source production and the analyzing the molecular internal states. The dye laser uses a color dye as the laser gain medium. Although each dye has a specific operating wavelength length, the visible and near IR spectrum have been mostly covered by all sorts of laser dyes. The dye laser pulses can be further frequency doubled to generate the UV wavelength.

In general, the dye lasers' wavelengths are measured by a spectrometer, which has a resolution of a few wavenumber at best. The Spectra-Physics Sirah dye laser has a narrower linewidth and thus can be measured by a wavelength meter instead.

Spectra-Physics Mai-Tai

This is a turn-key mode-locked Ti:Sapphire femtosecond laser for cooling of the silicon monoxide ions. The cooling mechanism will be discussed in Section 8.3. The preparation of the laser for this application will be detailed in Chapter 9.

6.3. Fluorescence Detection

The geometry of the imaging system for the molecular ion trap is similar to the one used in the single ion experiment. Limited by the obstruction of the trap electrodes, the emission from a single ion at the trap center has a solid angle of 0.151 sr, equivalent to 1.2% of the total fluorescence. The photon is first collected by an $f = 100$ mm lens followed by a relay telescope consisting of an $f = 200$ mm and an $f = 50$ mm lenses. The light is then split by a dichromatic mirror such that photons of different colors are imaged at two cameras at the same time. Specifically, the dichromatic mirror separates the UV photons from the visible ones. In each branch, there is an $f = 125$ mm lens to focus the beam onto the camera. The outline is also depicted in Fig. 6.3 as well. All the lenses in this imaging system are achromatic doublet lenses. The overall magnification is 5X.

Alignment

While the imaging system is constructed in the infinity corrected configuration, components can be separated into groups for alignment. A laser with the wavelength of interest is used as a calibration source during the alignment; we used the 385 nm laser

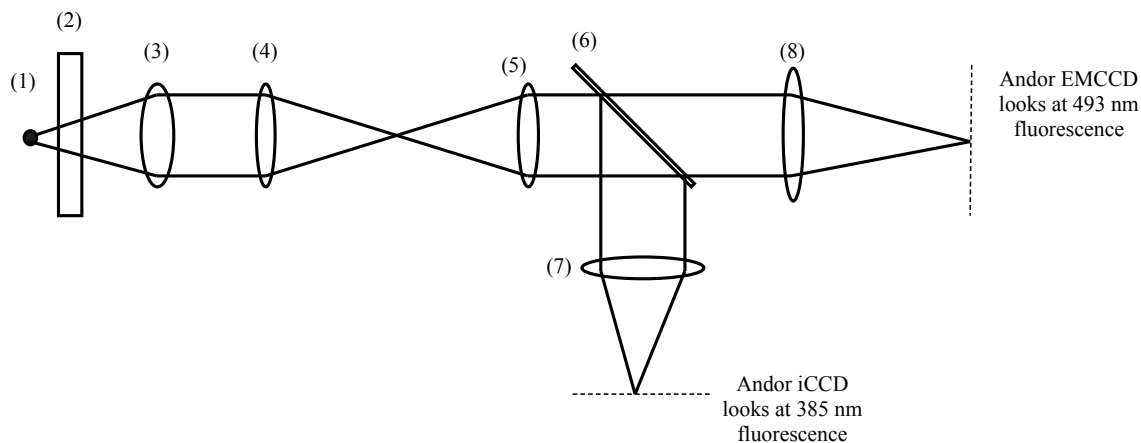


Figure 6.3. Imaging system for the molecular ion trap. (1) Single ion source, N.A. = 0.22. (2) Vacuum viewport; fused silica, about 10 mm thick. (3) $f=100$ mm achromatic doublet. (4) $f=200$ mm achromatic doublet. (5) $f=50$ mm achromatic doublet. (6) Dichroic mirror transmits 493 nm and reflects 385 nm. (7)(8) $f=125$ mm achromatic doublet.

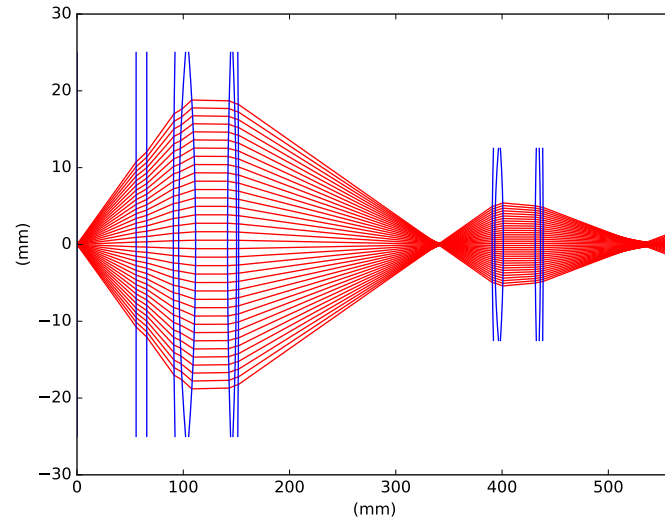
as the system is built to observe fluorescence from SiO^+ in the future. The calibration laser source is output coupled from a single fiber to ensure a good Gaussian mode. The collimation is checked by a shear interferometer.

The tube lens (L4 in Fig. 6.3) is aligned to the camera by making the laser best focused on the sensors. The relay telescope, which has two lenses (L2 and L3) confocal, takes a collimated input and makes a collimated output beam as well. Once these two modules are aligned, they are assembled together with other optics such as the dichroic mirror and other filters. The distance between modules is less critical due to the infinity corrected configuration. The objective lens (L1) is the last piece to be installed and is adjusted until a clear image is formed.

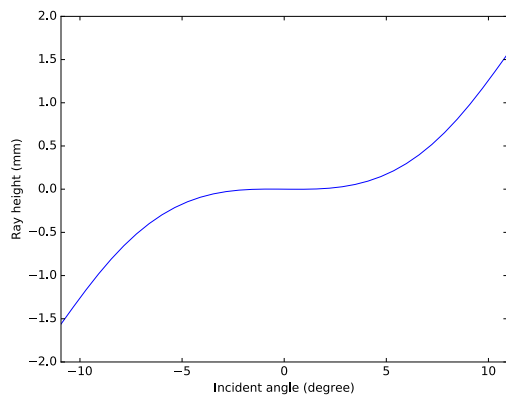
Aberration

The aberration of the imaging system is analyzed here by the optical ray tracing technique. In Fig. 6.4, the transverse ray aberration (TRA) of the imaging system used in this molecular ion project is plotted. The TRA plot shows the correspondence between the ray's initial location at the objective lens (horizontal axis) and its final location on the imaging plane (vertical axis). In this simulation, the rays are originated from a point source representing the ion. Therefore, a flat TRA curve would indicate a sharp image of the point source. However, the curve in Fig. 6.4 is flat only in a smaller region closed to the center of the optics. At larger aperture location, rays severely deviate from the focal spot. That is, not all of the collected fluorescence contributes to the image constructively; some of the light is actually scattered away and creates the halo around the image. Figure 6.5 shows some sample images of ions with aberrations.

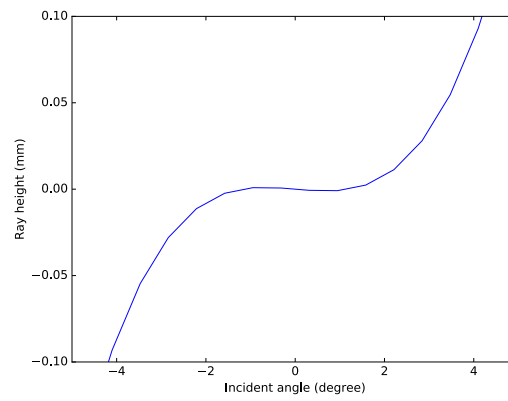
The major type of the aberration the imaging system suffering from is spherical. While the transverse spherical aberration grows as the cube of the aperture, it significantly lowers the imaging efficient. In Fig. 6.6, the collection efficiency for various sizes of the region of interest is measured. In this experiment, the ion is made to fluoresce a fixed amount of photons. Controlled fluorescence is achieved by first pumping the barium into the $5D_{3/2}$ state. Then, the camera is armed to detect signal while the 650 nm laser pumps the population into the $6S_{1/2}$. When the spontaneous decay to $6S_{1/2}$ happens, there is exactly one photon at 493 nm emitted. Therefore, the number of 493 nm fluorescence photons generated is equal to the times this sequence is repeated for. This experiment provides an accurate way to measure the fluorescence detection efficiency.



(a) System configuration



(b) TRA



(c) TRA zoom-in

Figure 6.4. TRA of imaging system

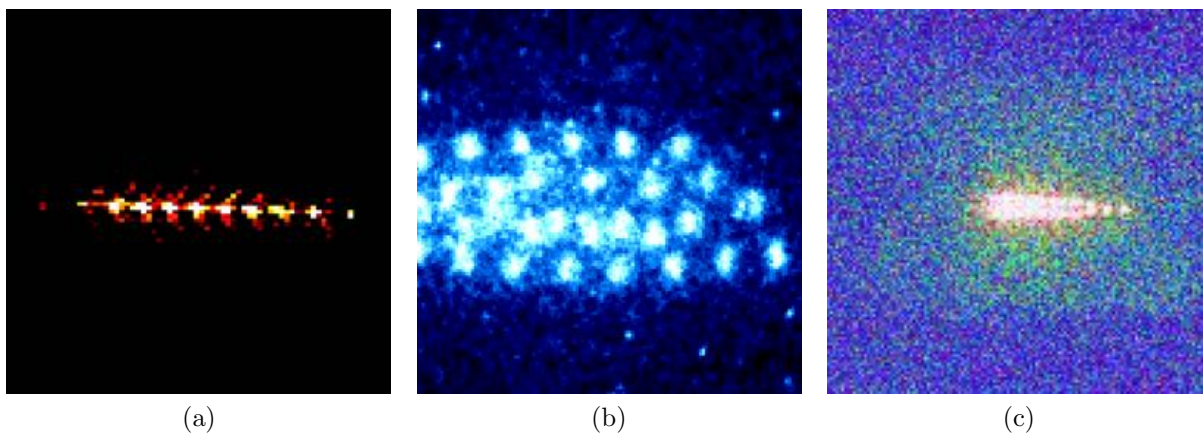


Figure 6.5. Some images of ions with optical aberration

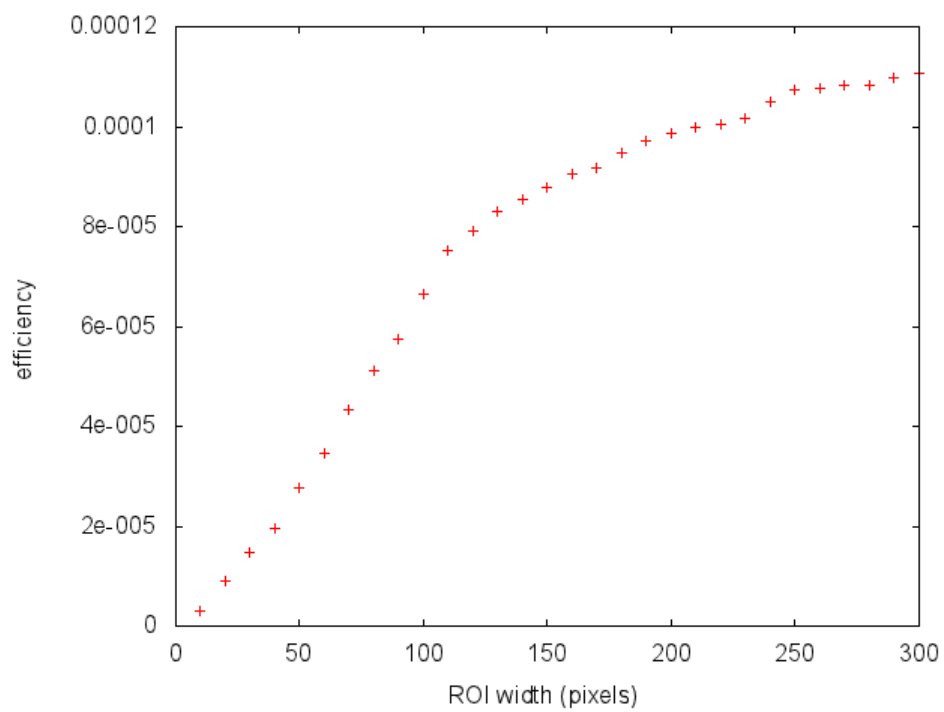


Figure 6.6. Efficiency vs ROI size

CHAPTER 7

The Molecular Ion Trap

This chapter covers the routines in the silicon monoxide ion project.

7.1. Trapping Barium Ions**Loading**

Barium ions are loaded into the trap to sympathetically cool the translation of the SiO^+ . The source is generated by laser ablating a barium bulk outside the trapping region. The ablation laser is the 532 nm pulsed YAG laser, which is visible and makes alignment easier. Laser ablation somewhat depends on the wavelength, but for atomic species, it is less critical. Usually, a focused laser beam with 10 to 100 μJ per pulse is sufficient for the ablation. A stronger ablation has much higher yield such that the excessive and energetic plume sputters the trapping hardware and often produces patch potentials severely shifting the ions away from the trap center.

With a moderate ablation energy, Ba^+ ion can be generated directly and some of the ions are kept by the ion trap while traveling through. While the trapping field is conservative, any ion traveling into the trap also has sufficient energy to escape the trap. Therefore, the ion must lose some energy to some other ions via the Coulomb interaction to be trapped. Note that Doppler laser cooling may not be fast enough to help capture ions as there is too few photon scattering during the time ions traveling across the trap, which is several microseconds. Pure ablation loading of ions is, therefore, less efficient due

to the above reasons. Examples of studies on this topic are, but not limited to, Appelhans and Dahl (2002); Doroshenko and Cotter (1997); Schuessler and Chun-Sing (1981).

Photoionization, on the other hand, produces ions inside the trap and thus makes trapping much easier. In this scheme, the neutral barium flux is generated by less ablation energy to suppress the ion yield. A photoionization laser, derived from either the dye or the OPO laser, then ionize the neutral atoms inside the trap. There is a 20 to 50 μs time delay between the ablation and the ionization laser corresponding to the traveling time into the trap. Empirically, a UV pulsed laser with sufficient energy (a few mJ) is able to ionize neutral barium without driving specific transitions. However, the production rate may be enhanced by driving a resonant transition. There are a bunch of excitation states that are accessible by the UV laser. Note that REMPI by a pulsed dye or OPO laser usually has insufficient state selectivity due to the broader laser linewidth. Therefore, in this trap, we load several isotopes of barium according to the natural abundance (refer to Section 4.1).

Laser Cooling

Doppler laser cooling of the trapped barium ion cloud is not different from the cooling of a single ion. In this experiment, the cooling lasers are along the end caps (axial) direction. Motion in the radial direction is also efficiently cooled as the radial momentum can be coupled to the axial direction by the isotropic Coulomb repulsion between ions.

Dark ions, i.e., ions do not interact with the cooling lasers, such as barium-137 are sympathetically cooled as their kinetic energy is transferred to the coolant ions, $^{138}\text{Ba}^+$.

Figure 7.1 shows a Coulomb crystal of the barium ions while the bright dots are individual $^{138}\text{Ba}^+$ and other dark isotopes are located at the right of the crystal. Usually,

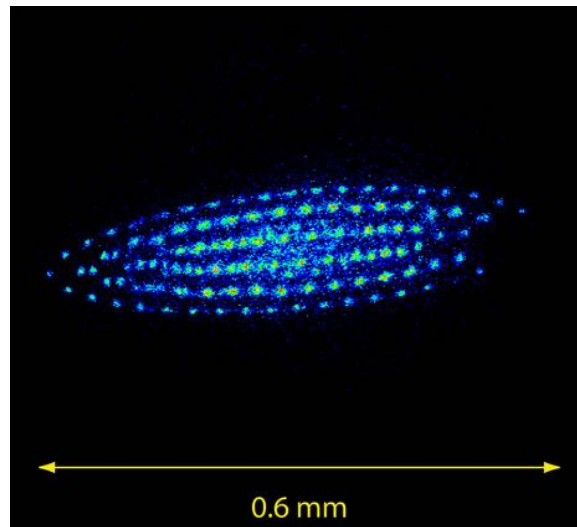


Figure 7.1. laser cooled barium ions

we trap an ion crystal of 500 to 1000 barium ions in the trap for the experiment. For the cloud with larger ion number, the micromotion heating becomes too strong and is difficult to laser cool to the ultracold temperature.

Micromotion Compensation

Detecting the micromotion amplitude by the fluorescence correlation does not work nicely for an ion cloud as the ions have different oscillation phases and will cancel out the modulation. Therefore, we can only compensate according to the fluorescence image as described in Section 4.5.

7.2. Loading SiO^+

Ablation

In order to produce silicon monoxide ions, we first ablate SiO target with a pulsed YAG laser similar to the barium ablation procedure. There are two forms of SiO targets

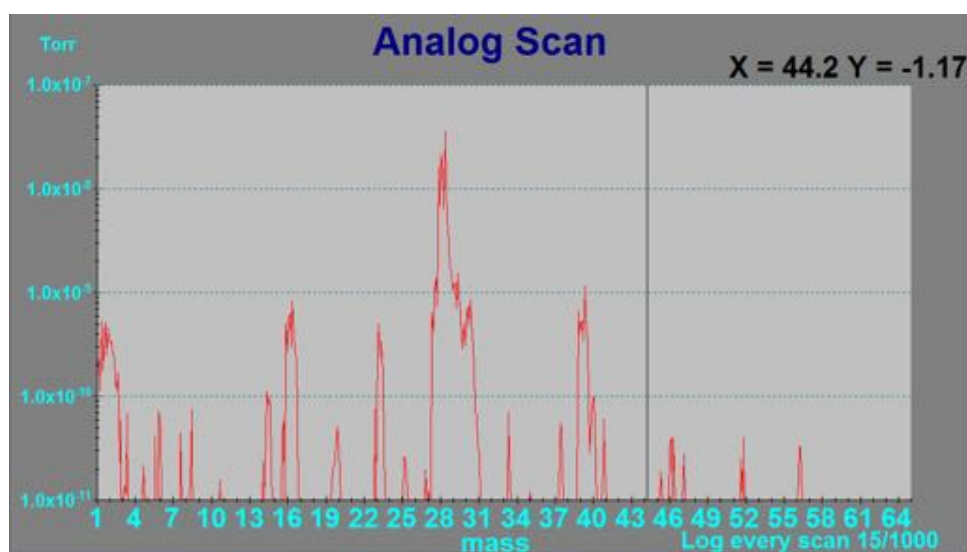


Figure 7.2. The mass spectrometry of the ablation product on RGA.

in the laboratory: pellet and piece. The pellet was made by compressing SiO powder; it is hardened by heat treatment. Recently, we started using small SiO pieces that can be obtained from several chemical suppliers. There are no additional preparation steps when using small pieces as the target. However, since the SiO pieces are structurally harder than the compressed pellets, we have to use more laser power to ablate the target for loading.

Unlike barium, which is an atomic material, laser ablation of the SiO target is a complex process that generates many undesired byproducts and comparatively little SiO^+ regardless of the form of the target (Jadraque *et al.*, 2009; Torres *et al.*, 2005). Some of the byproducts are alkali metals (Li, Na, K) as well as other atomic species (e.g., CO) that are common impurities found in chemical products. Both the neutral and the ionic form of these impurities can be present in the ablation plume depending on their ionization energies. On the other hand, because of the high energy density during ablation, the molecular

products can undergo additional reactions and make some common byproducts such as Si, SiO₂, and SiOH in both the neutral and ionic forms. Therefore, ablation loading of SiO⁺ would result in a contaminated ion cloud in the trap.

We then adopt the REMPI process to selectively produce the silicon monoxide ions (Nakamura and Kitajima, 1994, 1995; Nakamura *et al.*, 1996). First, the laser ablation intensity is tuned such that none of the ions produced by ablation will be trapped, but liberate neutral particles will reach the trapping volume. A pulsed dye or OPO laser at 287 nm then resonantly drives a two-photon transition between the $H^1\Sigma^+$ and the $X^1\Sigma^+$ states in SiO (Lagerqvist and Renhorn, 1974; Nakamura *et al.*, 1996; Oddershede and Elander, 1976). (Refer to Fig. 7.3 for the potential energy curves.) A third photon from the same laser pulse is able to provide enough energy to further ionize the excited molecule.

Sympathetic Cooling Efficiency

The silicon monoxide ions are sympathetically cooled by the barium ions which are loaded into the trap beforehand. While the lighter species is more tightly confined by the RF trapping field, the ultracold SiO⁺ stays inner to the Ba⁺ cloud. Therefore, the SiO ions present a dark core in the ion cloud as shown in Fig. 7.5.

We usually load approximately 100 SiO⁺ into the trap with 500 to 1000 Ba⁺. More SiO⁺ often results in inefficient cooling such that the trapped ions can not be cooled and crystallized. Sympathetically cooling rate is usually reduced for species with asimilar masses. See the molecular dynamics simulation study in (Zhang *et al.*, 2007) for some insight.

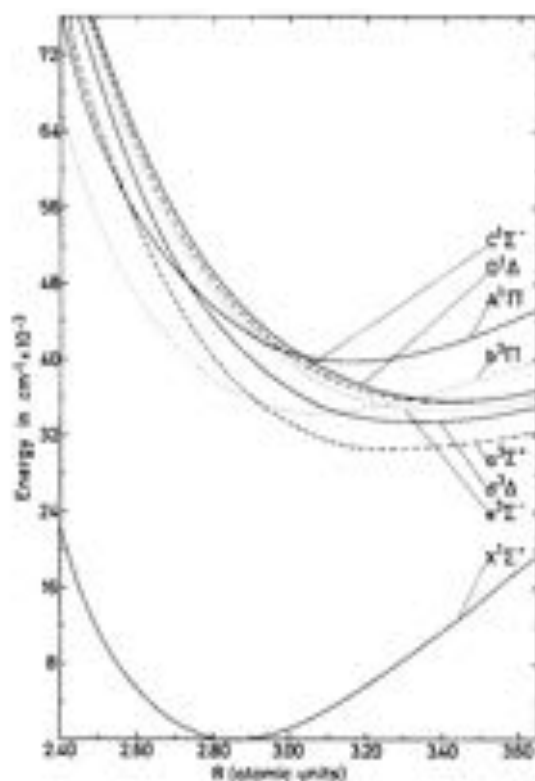


Figure 7.3. Potential energy curves in the neutral SiO. From Oddershede and Elander (1976).

7.3. Mass Spectrometry: Q-Scan

This section introduces the mass spectrometry of trapped ions based on the Paul trap mass filter. The mass spectrometry is used to examine the contents loaded into the trap and the product of photodissociation for the internal state analysis. Specifically, in the SiO^+ project, we measure the numbers of Si^+ and SiO^+ . Since the mass difference between these species is large, the mass spectrometry only needs moderate resolution which can be easily achieved in a quadrupole mass filter.

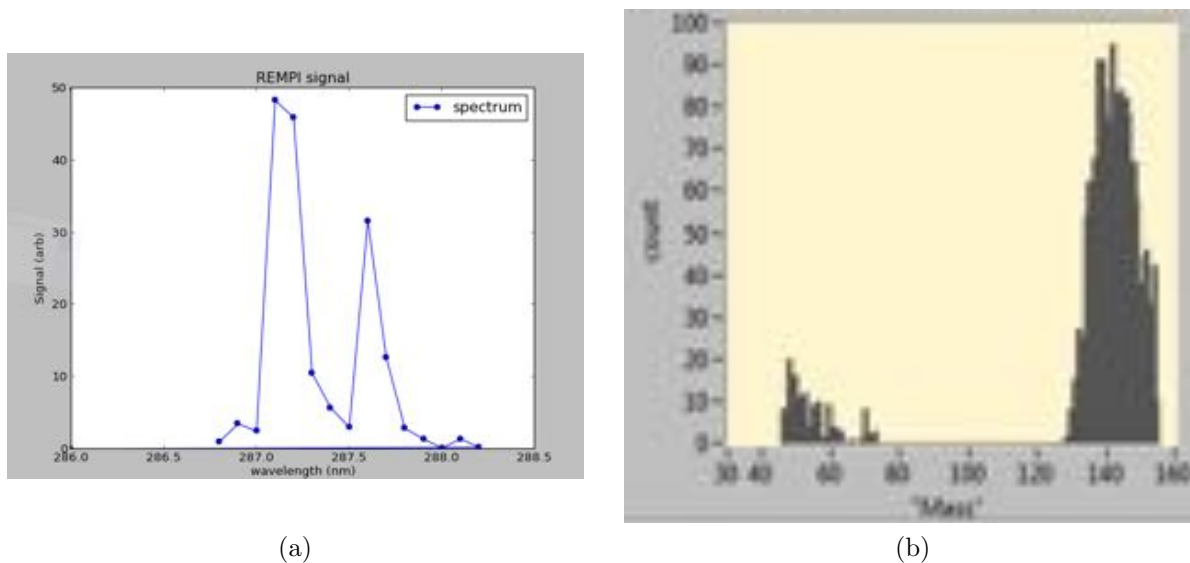
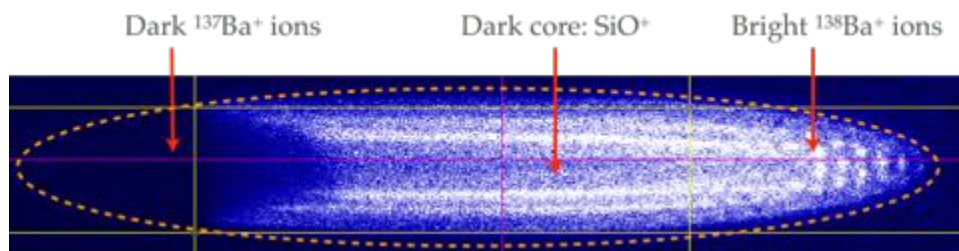


Figure 7.4. SiO REMPI spectrum.

Figure 7.5. SiO⁺ dark core.

Principle

The principle of an ion trap mass filter is the stability of the trap highlighted in Section 2.1. By tuning the RF voltage and/or DC voltages, we can selectively eject species outside the stable region (the trap) and register those ions on an ion detector. In particular, we sweep the RF voltage such that the ion's stability in the radial direction is scanned; a channel electron multiplier (CEM) is mounted next to the trap to catch the destabilized ions (Welling *et al.*, 1998; Schwartz *et al.*, 2002). As the q parameter is

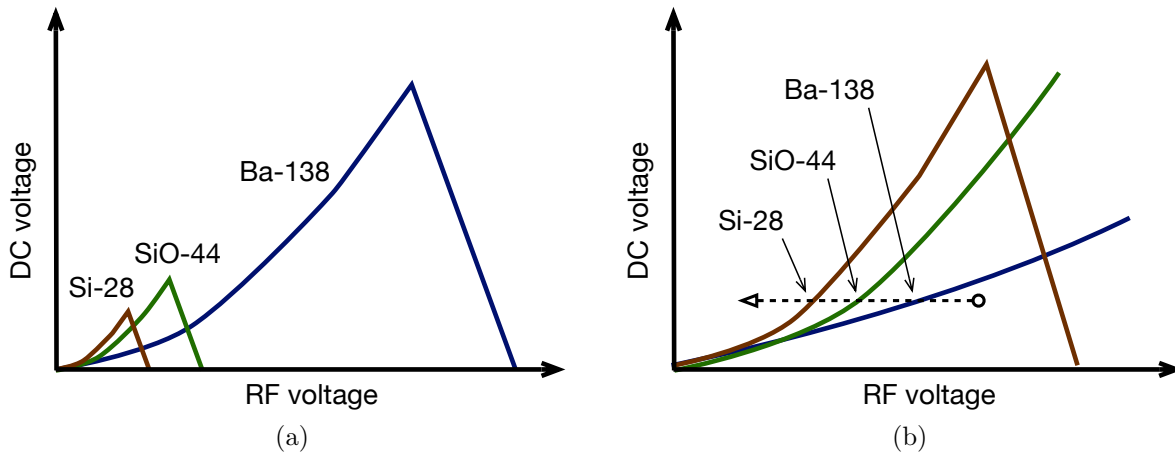


Figure 7.6. Stability region and the q-scan.

related to the RF voltage, this mass spectrometry is nicknamed as the q-parameter scan or the q-scan. Figure 7.6(a) shows the stability in terms of the trap voltage settings for Si^+ , SiO^+ , and Ba^+ . Initially, the trap is operated in the region where all species are stable. A certain species is ejected from the trap when the RF voltage is swept across the corresponding stability boundary. Therefore, by correlating the ion detector's signal with the RF voltage, one obtains the mass (m/e) spectrum of the trapped ions.

The mass spectrometry can be done by increasing or decreasing the value of the q parameter. In the first case, usually done when there is no DC electric field presented (i.e., $a = 0$), the charged particle is stable when $q < q_c = 0.908$. As $q \propto eV_{\text{RF}}/m$, the threshold voltage of the RF field is then proportional to the ion's mass-charge ratio m/e .

In the second case, the ion is destabilized at a lower q value where the trap confinement is weak. The weakly trapped ion can be pulled out by a sufficiently strong biasing electric field. Recall that the trap confinement (the pseudo-potential) is proportional to ω^2 , the

square of the secular frequency. As $\omega \propto q \propto V_{\text{RF}}$ for small q , it is easy to find that the threshold RF voltage is proportional to $\sqrt{m/e}$.

Between the two approaches, the former has a better spectrometry resolution. However, the latter is easier to implement. More theoretical study as well as the experimental demonstration of the q-scan mass spectrometry can be found in Welling *et al.* (1998); Schwartz *et al.* (2002).

Implementation

In the setup, the channel electron multiplier is roughly 2 cm from the trap center. See Fig. 7.7. The CEM is supplied with approximately -1800 V to attract positive ions as well as for the electron multiplier. The CEM output is first sent to a high bandwidth pre-amplifier. The amplified signal is either detected by a NIM (Nuclear Instrumentation Module) counter or recorded on an oscilloscope. When doing the mass spectrometry, we ramp down the RF voltage; ramping up is infeasible as we can not generate much higher voltages. The voltage is swept at the rate such that the corresponding mass sweep is slower than 1 ms per atomic mass unit (amu or u) so there is sufficient time for the unstable ions to register onto the CEM. The rate 1 ms/u was chosen experimentally.

Figure 7.8 shows a typical result of q-scan mass spectrometry of an ion cloud consisting Ba^+ , SiO^+ , and Si^+ . The data presents a moderate fractional mass resolution $\Delta m/m = 0.2$, which is quite sufficient for distinguishing different species in this project. However, isotopes or similar mass species such as SiOH^+ can not be resolved.

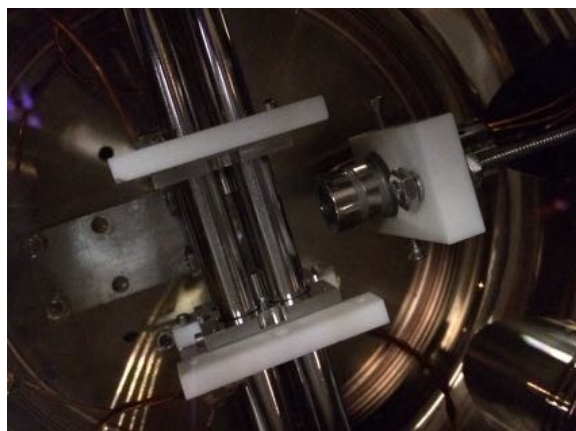


Figure 7.7. trap and ccm

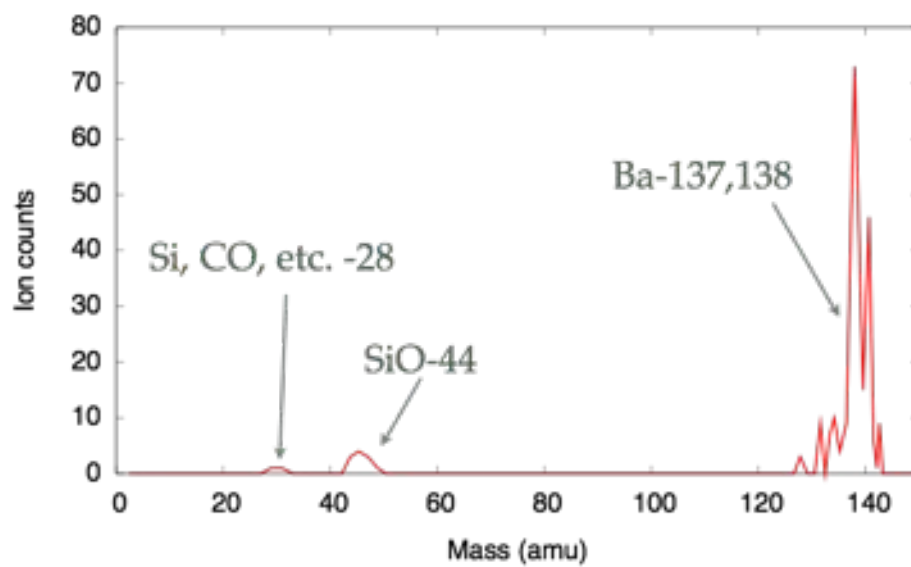


Figure 7.8. The q-scan data

CHAPTER 8

SiO⁺ Experiments

In this chapter, I introduce the silicon monoxide ion, one of the candidates for the single ion precision spectroscopy. SiO⁺ plays an important role in the chemistry of interstellar clouds and circumstellar regions; see the introduction in Scholl *et al.* (1995) for a comprehensive review. SiO⁺ is chosen because of several of its nice properties such isotope abundance, diagonal transitions, etc. The rotational transition is easily accessible in the microwave band. The laser wavelengths for manipulating the internal states are not extreme either.

Isotope Abundance

The most common silicon monoxide isotope is ²⁸Si¹⁶O while the natural abundance of ²⁸Si is 92.23% and 99.8% for ¹⁶O. Thus, the natural abundance of ²⁸Si¹⁶O is 92%, followed by ²⁹Si¹⁶O (4.7%) and ³⁰Si¹⁶O (3.1%). In the single ion experiment, one repeats the loading process until the desired isotope is loaded; the mass of the loaded species co-trapped with a single Ba⁺ can be determined from their normal mode secular frequencies. To load larger amount of pure ⁴⁴[SiO] ions, the REMPI could be an effective approach. However, we never explore the idea; neither we have the sufficient mass spectrometry resolution. Because the mass of the unwanted SiO isotopes is between 44 u and 138 u (for ¹³⁸Ba⁺), we can not selectively eject those SiO⁺ out from the Paul trap mass filter without ejecting other species.

As both nuclei are even isotopes that have zero nuclear spins, SiO also have zero total nuclear spins and thus there is no hyperfine structures. This greatly simplifies the manipulation of the silicon monoxide ion's internal state.

8.1. Level Structure

The silicon monoxide ion has one valence electron, which makes this molecular ion like an alkali-atom.

The $X^2\Sigma^+$, $A^2\Pi$, and $B^2\Sigma^+$

The ground electronic state of the SiO^+ is $X^2\Sigma^+$, which dissociates into a ground-state $\text{Si}^+(^2P_u)$ and a ground-state $\text{O}(^3P_g)$. The $^2\Sigma$ state is a Hund's case (b) molecule where the electron's orbital angular momentum is coupled to the molecular axis, but the spin is only weakly coupled to or decoupled to the axis. Especially for $^2\Sigma^+$, the total angular momentum excluding spins, N , is equal to the rotational angular momentum; the total angular momentum excluding nuclear spin is, therefore, $J = N + S$. Rotational states are labeled by $|J, N, m_j\rangle$ in this state with $N = 0, 1, 2, \dots$ and $J = 1/2, 3/2, 5/2, \dots$ as $S = 1/2$.

The excitation state $B^2\Sigma^+$, also a Hund's case (b) molecule, is almost directly above the X ground state. The vibrational constant is similar to that of the X state too. Therefore, the vibrational transitions between these two states are fairly diagonal. The total state lifetime is 69.5 ns from $v = 0$ (Scholl *et al.*, 1995). See next section for more details. This state has the same rotational level structure as in the X . The $B^2\Sigma^+$ dissociates into a $\text{Si}^+(^2P_u)$ and an excited $\text{O}(^3D_g)$.

Laying 2242.25 cm^{-1} above is the first excitation state, the $A^2\Pi$ state, in the SiO^+ . This state has the same dissociation limit as the ground X state. The equilibrium radius of the A state is quite different from the one of the X and the B state.

Energy Spectrum

For the $^2\Sigma$, the energy spectrum is expressed as

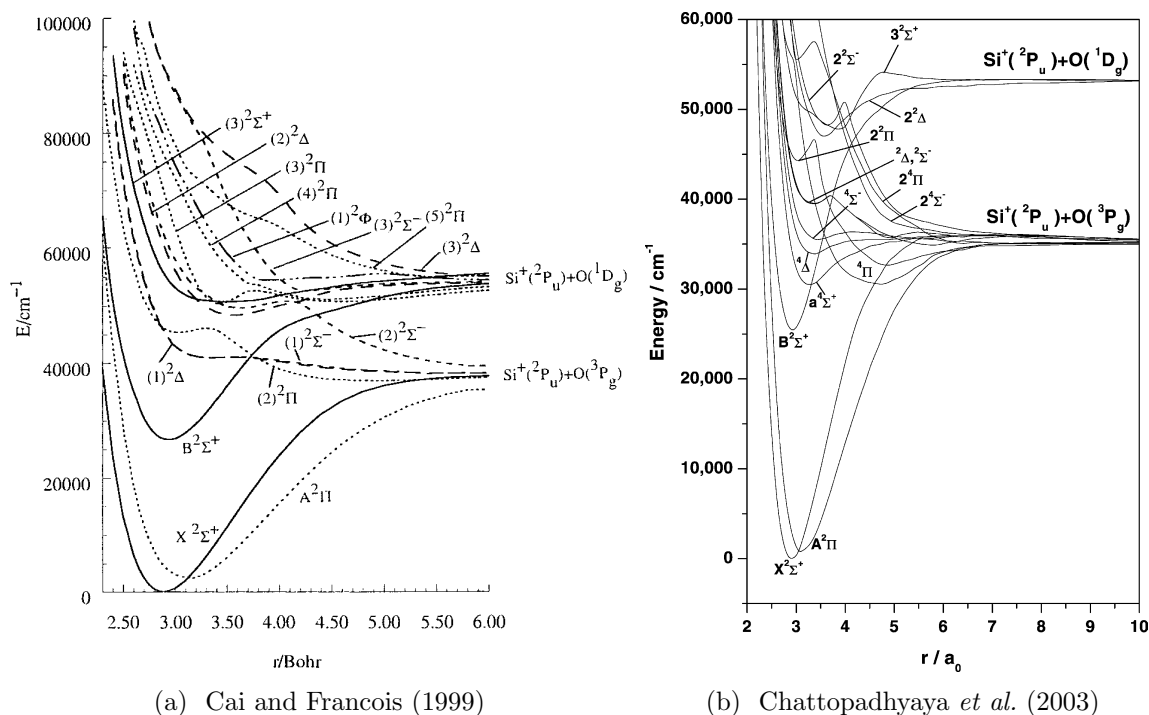
$$E = T_e + \omega_e(v + \frac{1}{2}) - \omega_e x_e(v + \frac{1}{2})^2 + B_e J(J + 1) - D_e [J(J + 1)]^2 - \frac{1}{2} \gamma_v J \quad (8.1)$$

where $v = 0, 1, 2, \dots$ is the vibration quantum number. The names of each constant in the above equation along with other common spectroscopic constants are summarized below.

- T_e : the equilibrium energy; this is the energy when the inter-nuclear distance is r_e .
- r_e : the equilibrium inter-nuclear distance.
- ω_e : the (harmonic) vibrational constant.
- $\omega_e x_e, \omega_e y_e$: the first-order and the second-order anharmonic vibrational constants.
- B_e : the rotational constant.
- D_e : the centrifugal distortion constant.
- γ_v : the spin-rotation coupling constant.

Note that the coupling between the X and the A states is the primary reason for the spin-rotation coupling in the $X^2\Sigma^+$.

The energy spectrum of the $A^2\Pi$ is analyzed in, for example, Cameron *et al.* (1995b).

Figure 8.1. Potential energy curves of SiO^+ .Table 8.1. Spectroscopic constants of the X , A , and B state in the SiO^+

State	T_e (cm^{-1})	R_e (nm)	ω_e (cm^{-1})	$\omega_e x_e$ (cm^{-1})	B_e (cm^{-1})
$X \ ^2\Sigma^+$	0	0.151 62	1162.18	6.9698	0.720 62
$A \ ^2\Pi$	2242.25	0.163 65	946.28	7.005	0.618 59
$B \ ^2\Sigma^+$	26 029.01	0.152 43	1136.58	6.9215	0.713 03

Some spectroscopic constants of the X , A , and B states in SiO^+ are listed in Table 8.1. Figure 8.1 shows the calculated potential energy curve of the SiO^+ .

Literature Review - Experiments

Experimentally, the spectrum of SiO^+ was studied with the fast-ion-beam spectroscopy. Cameron *et al.* (1995a,b); Rosner *et al.* (1998) have described the experimental

and data analysis methods. Frequencies of transitions in multiple $B-X$ and $B-A$ were published in these papers as well. This database is our primary transition frequency reference.

One of the earliest observations of SiO^+ was Pankhurst (1940). But, in fact, the spectrum was mistakenly attributed to SiO_2 and was corrected by Woods (1943). More spectroscopy experiments on SiO^+ include Lagerqvist and Renhorn (1974); Colbourn *et al.* (1978); Ghosh *et al.* (1979) as well as the fast-ion-bem spectroscopy mentioned above.

Literature Review - Theories

The theoretical study of the electronic structures in SiO^+ is quite involving and is beyond the scope of this dissertation. The introduction sections in some of the recent theoretical papers (for instance, Shi *et al.* (2012)) generally provided a good review on previous computational works.

8.2. Transitions in SiO^+

This section introduces the electronic transitions between the X , A , and B states. I will first focus on the branching ratio in these transition bands, then I will describe the rotational transitions in the $B-X$ band.

The conventions of the notations are stated below.

- Quantum numbers with a single prime are for the initial state; a double prime is for the final state.
- When referring to a transition band, the state with higher energy is mentioned first. For example, I write the $B-X$ band in the SiO^+ , instead of the $X-B$.
- The transition band between v_1 and v_2 has the shorthand (v_1v_2) .

- The path of the transition is indicated by the arrow. That is, both $a \rightarrow b$ and $b \leftarrow a$ are transitions from a to b . Oftentimes, the former indicates a spontaneous emission whereas the latter indicates a driven transition.

Branching Ratio in $B-X$

Most of the SiO^+ work are done with the transitions between the $B^2\Sigma^+$ and the $X^2\Sigma^+$. While these two states have similar equilibrium internuclear separations R_e and vibrational constants ω_e , vibrational transitions are quite diagonal in this band. The theoretical branching ratios were computed by Dr. Jason Nguyen during his appointment in our group; the result is listed in Table 8.2.

Experimentally, Stollenwerk *et al.* (2016) made a preliminary measurement on the branching fractions by the dispersed fluorescence technique. The branching fraction of the diagonal branch $v'=0 \rightarrow v''=0$ is 97%, while the first off-diagonal branch $v'=0 \rightarrow v''=1$ has up to 3% fractions.

The $B-A$ and $A-X$ Bands

The $B-A$ is yet another decay channel from the B excitation state. Since the potential energy surfaces of these two states are not aligned vertically, the transitions in $B-A$ is not diagonal. That is, the decay from B to A does not preserve the vibration.

The total decay rate in this band is $3.2 \times 10^3 \text{ s}^{-1}$, which is 2.5×10^{-4} of all the decay branches from B according to Cai and Francois (1999). Once the population falls into the A state, we rely on the $A-X$ decay to bring the molecular ion back to the ground electronic state. Again, since A and X are not aligned, the vibrational transitions are not

Table 8.2. Decay rates of some relevant decay channels in SiO^+ . These rates were calculated in-house.

Upper state	Lower state	Decay rate (s^{-1})	Remarks	
$B^2\Sigma^+, v'=0$	$\rightarrow X^2\Sigma^+$	1.4×10^7	Total rate.	
	$\rightarrow v''=0$	1.4×10^7		
	$\rightarrow v''=1$	9.1×10^4		
	$\rightarrow v''=2$	3.3×10^2		
	$\rightarrow v''=3$	9.1		
$B^2\Sigma^+, v'=0$	$\rightarrow A^2\Pi$		Total rate.	
	$\rightarrow v''=0$	2.9×10^2		
	$\rightarrow v''=1$	4.2×10^2		
	$\rightarrow v''=2$	3.6×10^2		
$A^2\Pi$	$v'=0$	$\rightarrow X^2\Sigma^+$	2.4×10^2	Total rate.
	$v'=1$	$\rightarrow X^2\Sigma^+$	1.3×10^3	Total rate.
	$v'=2$	$\rightarrow X^2\Sigma^+$	2.7×10^3	Total rate.
	$v'=3$	$\rightarrow X^2\Sigma^+$	4.5×10^3	Total rate.
$X^2\Sigma^+$	$v'=1$	$\rightarrow v''=0$	3.7×10^{-2}	
	$v'=2$	$\rightarrow v''=0$	3.3×10^{-1}	
		$\rightarrow v''=1$	1.6×10^{-1}	
	$v'=3$	$\rightarrow v''=0$	2×10^{-3}	
		$\rightarrow v''=1$	1	
		$\rightarrow v''=2$	3.3×10^{-1}	

diagonal either. The relaxation rate from A to X is estimated to be $\sim 10^3 \text{ s}^{-1}$, which is comparable to the rate falling into the A state.

Rotational Transitions

The rotational transitions in the SiO^+ $B-X$ is fairly simple as both the ground and the excitation states are $^2\Sigma^+$. In a $^2\Sigma-^2\Sigma$ system, the allowed transitions are $\Delta N = \pm 1$ and $\Delta J = 0, \pm 1$. The main ones are the P and R branches, corresponding to $\Delta N = \Delta J = -1$ and $+1$, respectively. There is no Q branch in the $B-X$. Each transition in the main

branch has a satellite transition next to it, corresponding to $\Delta J = 0$. For the P branch, the satellite branch is PQ where $\Delta N = -1$ and $\Delta J = 0$; similarly, for the R branch, the satellite branch is RQ where $\Delta N = +1$ and $\Delta J = 0$. The satellite branches flip the spin and thus are weaker than the main.

The main and the satellite transitions are resolved due to the spin-rotational interaction $\gamma \vec{S} \cdot \vec{R}$ where \vec{S} and \vec{R} are the spin and pure rotation angular momentum, respectively, and γ is the spin-rotational constant.

A specific rotational transition can be labeled by the branch it belongs to and its lower state. For instance, R(5/2) is an R branch transition from $N'=2, J'=5/2$ to $N''=3, J''=7/2$. The first transition in the P branch is P(1/2).

Reference Spectroscopy

Frequencies of several transitions in the SiO^+ has been measured by the fast-ion-beam spectroscopy and were reported in Cameron *et al.* (1995a,b); Rosner *et al.* (1998). In the laboratory, we performed the laser-induced fluorescence spectroscopy to calibrate the laser system to the database.

Our reference spectroscopy was based on the experimental design in Matsuo *et al.* (1997); Mogi *et al.* (2002). The silicon monoxide ion is formed by laser ablating the silicon bulk in an oxygen-filled chamber. The chemical reaction turns Si^+ into SiO^+ . The probe is the nanosecond pulsed dye laser, which excites the sample 20 to 40 μs after the ablation. The fluorescence is collected for 50 to 100 ns right after the excitation pulse.

We have used the 1064 nm and the 532 nm pulsed YAG for the ablation. However, it takes more ablation energy to produce the ion with the green pulses. If we steadily ablate the same spot on the silicon target, the surface condition may be changed adversely such

that the ion yield fluctuates and eventually drops. Therefore, the target is mounted on an in-vacuum rotation stage so the ablation spot is constantly changing.

In Matsuo *et al.* (1997), the SiO^+ yield was maximized when the background oxygen pressure is around 100 mTorr. However, the reason was not discussed in the reference. In this project, we had observed the similar O_2 pressure dependence. The observed maximum yield might be the balance between the reaction rate and the reaction energy. The reaction $\text{Si}^+ + \text{O}_2 \rightarrow \text{SiO}^+ + \text{O}$ is endothermic. (See Fahey *et al.* (1981) for the dependence on Si^+ mobility.) The required energy apparently comes from the energetic silicon ions produced by the ablation. Most likely, the energy is due to the mobility; it is also possible that the Si^+ is excited and possesses extra energy for a while after the ablation. In any case, the ion loses energy when thermalizing with the room temperature oxygen background gas. While higher O_2 density increases the reaction rate, the reaction constant yet decreases as the energy for the reaction is taken away faster. Therefore, the reaction is maximized at a specific O_2 pressure.

Although the chamber is filled with oxygen gas during the experiment, we found it is necessary to evacuate the chamber beforehand. Flowing O_2 into the chamber and then pumping out the excessive gas to 100 mTorr did not give the same result. It is possible that, without prior vacuum preparation, the residual gasses (e.g., H_2O) quickly react with either Si^+ or SiO^+ such that the sample size is significantly reduced.

Figure 8.2 shows the typical signal captured by a photomultiplier tube. The laser ablation takes place at $t = 0 \mu\text{s}$, while the probe pulse excites at $t = 26 \mu\text{s}$. The light emission in between these two times is the so-called plasma emission and does not have a specific spectrum. In Fig. 8.2(b), the signal after the application of the probe laser

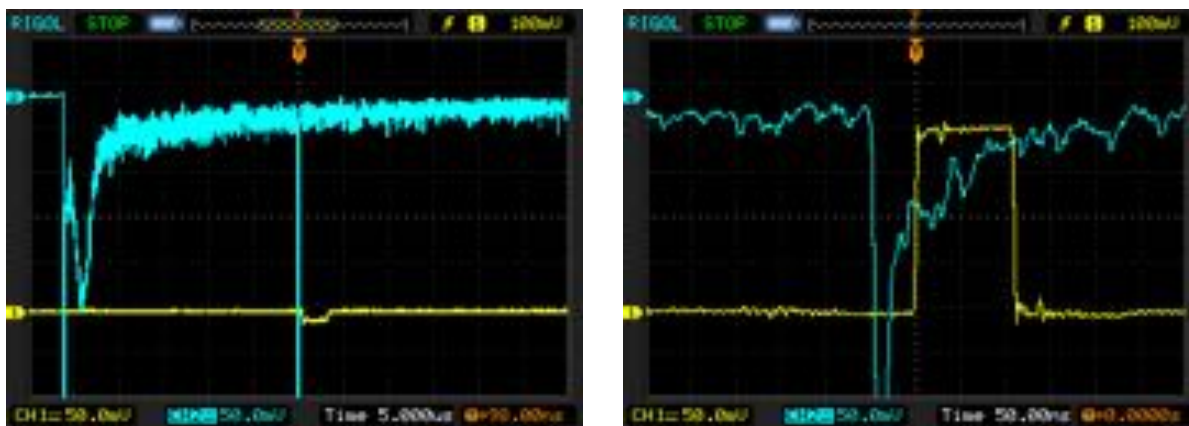


Figure 8.2. reference spectroscopy signal

is zoomed. Extra light, the laser-induced fluorescence, is apparent. The fluorescence goes away with a time constant ~ 70 ns, corresponding to the B state lifetime in SiO^+ . We started collecting the fluorescence ≈ 50 ns after the laser excitation to avoid the laser scattering and the collection gate is ≈ 100 ns. The fluorescence signal as a function of the excitation laser's frequency is shown in Fig. 8.3.

8.3. Internal State Cooling

While the translation of the molecular ions is sympathetically cooled via the Coulomb interaction, the molecular internal state remains unaltered as the long range Coulomb interaction hardly couples to the internal degrees of freedom. In this project, we have proposed and explored all optical cooling of the molecular internal states.

Initial Population Distribution

There is no good estimate of the temperature associated with the laser ablation and REMPI loading. However, SiO^+ 's excited vibrational population decays to the ground

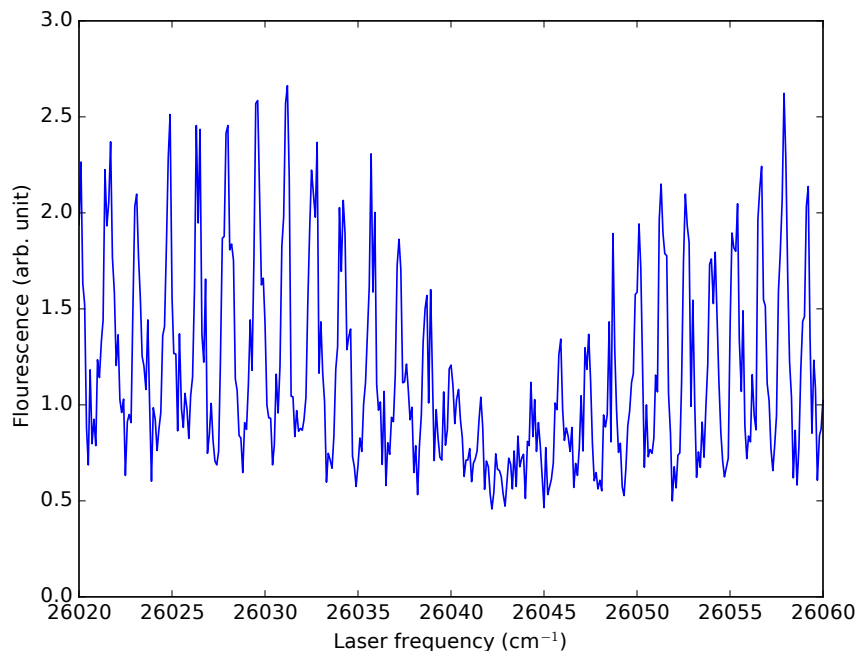


Figure 8.3. SiO^+ laser-induced fluorescence spectrum in $X-B, (00)$.

state within a minute; the higher rotational states also thermalized with the room temperature blackbody radiation in a few seconds. (See Section 8.4 for more information.) Thus, the temperature of the internal degrees of freedom in the SiO^+ should be close to the room temperature.

At the room temperature, the population of the SiO^+ is mostly in the ground vibrational state in the $X^2\Sigma^+$. Recall that the vibrational constant of the X state is $\omega_e = 1162.18 \text{ cm}^{-1}$ or 1672 K. The distribution of the rotational states is

$$P(K) = \frac{1}{Z} (2J + 1) e^{-B_e J(J+1)/k_B T} \quad (8.2)$$

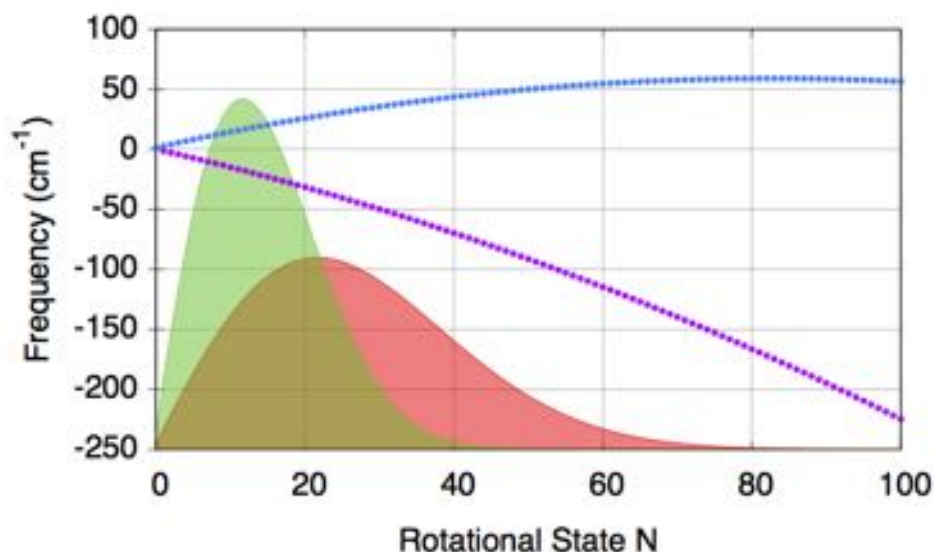


Figure 8.4. Population distribution in the rotational states of SiO^+ at 300 K (green) and 1000 K (magenta). The P-branch (purple) and R-branch (blue) rotational transitions in the $B-X$, (00) band are shown as well.

where J is the rotational quantum number, k_B is the Boltzmann constant, and T is the temperature. Z is the partition function. The rotational constant $B_e = 0.72 \text{ cm}^{-1}$ is equivalent to 1 K. Figure 8.4 shows the rotational population distribution at 300 K and 1000 K. In the best case, where the trapped SiO^+ completely thermalizes to the room temperature, about 40 rotational levels are populated.

P-branch Optical Pumping

Cooling of the SiO^+ 's rotational degree of freedom is done by pumping the P-branch transitions. Figure 8.5 illustrates the process. The SiO^+ in the J rotational level is excited to $J-1$ via the $P(J)$ transition. The spontaneous decay brings the population either back to the original J level via the R-branch or the $J-2$ level via the P-branch; the probability is about equal. By continuously driving this process, the rotation of the

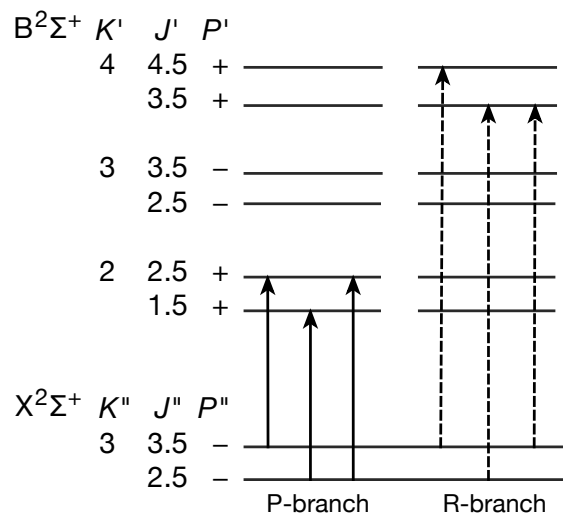


Figure 8.5. Rotational cooling illustrated.

molecule is removed until the population is in either the $J=1/2$ level or the $J=3/2$ level. Since the above optical pumping scheme involves two photons at each step, the parity of the population never changes. Thus, all the even parity population is pumped to $J=1/2$, while all the odd parity population is pumped to $J=3/2$. Strategies for overcoming the parity barriers are discussed later.

The rate of rotational cooling by the optical pumping is mainly determined by the photon scattering rate. If dipole allowed transitions are utilized in the cooling scheme, it takes 10 to 100 ns to remove one rotational quantum. This is much faster than many other molecular cooling schemes such as the buffer gas cooling. For cooling of SiO^+ , the efficient photon scattering is realized by driving transitions between B and X at 385 nm. The scattering rate, when the transition is saturated, is approximately $7 \times 10^6/\text{s}$.

Broadband Optical Pumping

Multiple P-branch transitions need to be driven in order to pump population from high rotation states all the way to the rotational ground state. Instead of using one narrow linewidth each to drive all the cooling transitions, one broadband laser source is used to excite the P-branch simultaneously.

The broadband source, at 385 nm, is the second harmonic generation of a femtosecond Titanium Sapphire (Ti:Sapphire) laser. This Ti:Sapphire laser (Spectra-Physics Mai-Tai) is a mode-locked ultrashort pulse laser that outputs <100 fs pulses at about 80 MHz repetition rate. At the fundamental wavelength 770 nm, the bandwidth of this laser is more than 100 cm^{-1} . Therefore, the spectrum of the SHG UV source is greater than 200 cm^{-1} , which conveniently covers the P-branch and the R-branch in the $B-X, (00)$ transition band. However, exciting the R-branch adds rotations to the molecules and should be avoided. The spectrum of the UV broadband source is therefore modified by the ultrashort pulse shaping technique such that the spectral components driving the R-branch are blocked.

The ultrashort pulse shaper is an optical waveform synthesizer. The setup, similar to an optical spectrometer, uses a diffraction grating to separate different spectral components spatially. By modulating the amplitude and the phase of each component, an output light with a desired waveform is obtained for specific applications. For cooling the SiO^+ 's rotation by P-branch optical pumping, we only modulate the amplitude of the spectrum; the phase is irrelevant and is left uncontrolled. Therefore, we use the ultrashort pulse shaping as a programmable optical filter in our experiment; we then refer the technique as the spectral filtering.

Specifically for the SiO^+ , the filter is low-passing as the P- and R-branch are well separated. The required filtering resolution is therefore set by the 2.8 cm^{-1} gap between two branches. High-resolution spectral filtering in the UV wavelength is discussed in Chapter 9.

Regard the optical pumping rate. The unmodified UV source is about 2 W over 300 cm^{-1} , and therefore, the spectral power density is $0.22\text{ }\mu\text{W}/\text{MHz}$. As the B state lifetime is 70 ns , the saturation intensity of the $B-X$, (00) transitions is of order $50\text{ }\mu\text{W}/\text{mm}^2$. To saturate the transition, the laser is focused to smaller than $37\text{ }\mu\text{m}$ radius.

Branching Ratio and Repumping

State manipulation by optical pumping, of course, requires closed photon cycling. Fortunately, the $B-X$ band in the SiO^+ has a small off-diagonal vibrational branching, about 3%. That is, on average, the population can be scattered in the (00) band for 32 times before it falls out of the manifold. This is already sufficient to pump most population into the rotational ground state.

The population decays into the vibrational excitation states can be repumped by driving the $v-1 \leftarrow v$ transitions. In the SiO^+ , multiple $v-1 \leftarrow v$ transition bands can be driven by a single femtosecond pulsed laser at 405 nm . Figure 8.6 shows the frequencies of several repumping transitions as well as a typical spectrum of the frequency doubled 405 nm Ti:Sapphire laser. With this laser, population from some high vibration state, say up to $v = 10$, can be repumped into $v = 0$ after a few off-diagonal vibrational excitations.

In addition to the off-diagonal vibrational decay in the $B-X$, another decay channel from the B state is the $B-A$. This channel can be somewhat troublesome. There are no specific selection rules over the vibration in this band, and hence, population dropping

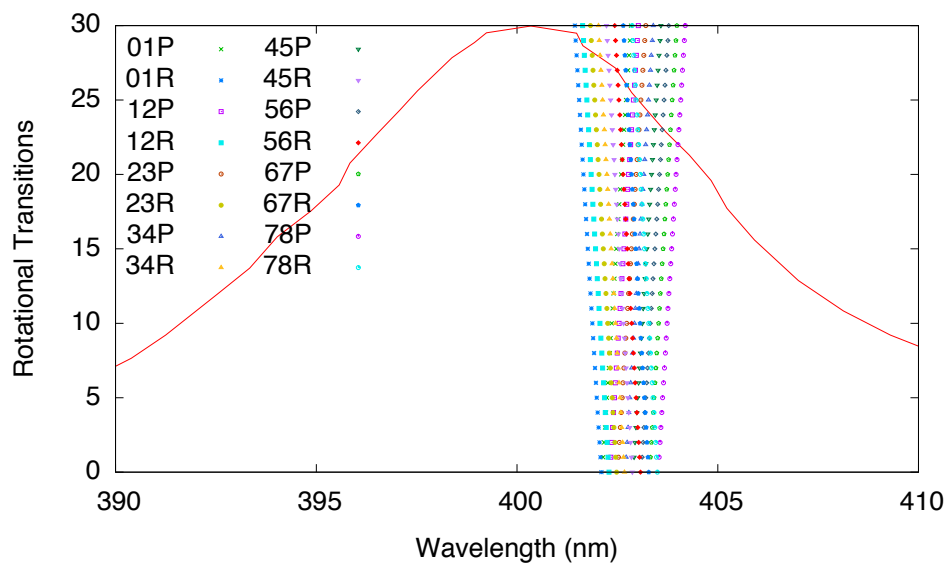


Figure 8.6. Vibrational repumping

into the A state can have any vibrations. This makes repumping difficult. However, some theoretical calculation shows that the relaxation rate from A to X has an order of ms, which may be fast enough for our rotational cooling scheme. The population dynamics in SiO^+ was studied based on the rate equation simulation by Tabor (2014); Nguyen and Odom (2011) for various optical pumping schemes and scenarios of decay rates.

Parity Barrier

As a recap, the rotational cooling scheme discussed above preserves the parity and thus the population is pumped into either $|N=0\rangle$ (even) or $|N=1\rangle$ (odd). To further move the population into a single parity, the barrier between both parities can be removed by an additional photon.

A microwave source can be used to drive population between two adjacent rotational levels. For instance, population in $|N=1\rangle$ can be driven to $|N=2\rangle$ (transition frequency 43 GHz) and then pumped to $|N=0\rangle$ by the cooling laser.

On the other hand, the parity flipping transition can be the vibrational relaxation in X or the $A \rightarrow X$ decay when the molecule is in $|X, v \neq 0\rangle$ or $|A\rangle$ and is not repumped. The integrated probability for pumping population into $|X, v \neq 0\rangle$ or $|A\rangle$ is increased when the $P(3/2), N'=1, J'=3/2 \rightarrow N''=0, J''=1/2$, and the ${}^PQ(1/2), N'=1, J'=1/2 \rightarrow N''=0, J''=1/2$, transitions are driven as these transitions cycle between $|X, N'=1\rangle$ and $|B, N''=0\rangle$ continuously until an off-diagonal decay occurs. However, since $|X, v \neq 0\rangle$ can be actively repumped and the relaxation is quite slow, the major contribution is expected to come from the $A \rightarrow X$ decay. Indeed, some of the time scales need a better experimental justification in order to fully plan out this approach.

For either configuration, the rovibrational ground state, $|X, v=0, N=0\rangle$, becomes the only dark state in the rotational cooling of SiO^+ 's internal state.

Review of Similar Works

One of the earlier investigations on optical cooling schemes for molecules is Bahns *et al.* (1996); also see the reference therein for a review of prior researches.

Viteau *et al.* (2008) demonstrated cooling of molecule's vibration using shaped broadband laser. The principle of such work is similar to our broadband rotational cooling scheme.

One of the first demonstration of optical rotational cooling is Staantum *et al.* (2010). In this work, a single laser drove the $v'=0, J'=2 \rightarrow v''=1, J''=1$ ro-vibrational transition

in the ground-state $\text{MgH}^+(^1\Sigma)$ to pump population into the ground rotational state. Population in higher rotational levels are brought into $v'=0, J'=2$ through transitions induced by the black-body radiation, which limited the cooling rate.

AlH⁺ Demonstration

Our rotational cooling protocol has been demonstrated with aluminum monohydride ion (AlH^+), another molecular ion species our lab works with (Lien *et al.*, 2014). This molecular ion has high nuclear spins and thus the hyperfine structure is not the simplest, which raises some difficulties for the precision spectroscopy. However, AlH^+ is a lighter molecule, hence has larger rotational constants B_e and less rotational states populated thermally. The vibrational relaxation rate is much faster than that of a typical oxide molecule, which makes repumping unnecessary. Nevertheless, AlH^+ has diagonal transitions between $|A^2\Pi\rangle$ and $|X^2\Sigma^+\rangle$, with a 3% first off-diagonal branching ($|A, v'=0\rangle \rightarrow |X, v''=1\rangle$). Overall speaking, AlH^+ is a good test bench for our broadband rotational cooling scheme.

Refer to Kokish *et al.* (2016); Lien *et al.* (2014); Müller and Ottinger (1986) for the production of AlH^+ . Similar to the SiO^+ experiment, multiple AlH^+ are co-trapped with the Ba^+ cloud in an identical ion trap. While the principle of the rotational cooling is as described in this section, specific parameters can be found in the reference mentioned in this topic. Internal state analysis is done by the resonance enhanced multi-photon dissociation (REMPD), followed by the time-of-flight mass spectrometry (Seck *et al.*, 2014).

Figure 8.7 shows evidence of rotational cooling of AlH^+ . The thermal population distribution is shown in dark red. At the room temperature, up to 7 rotational states

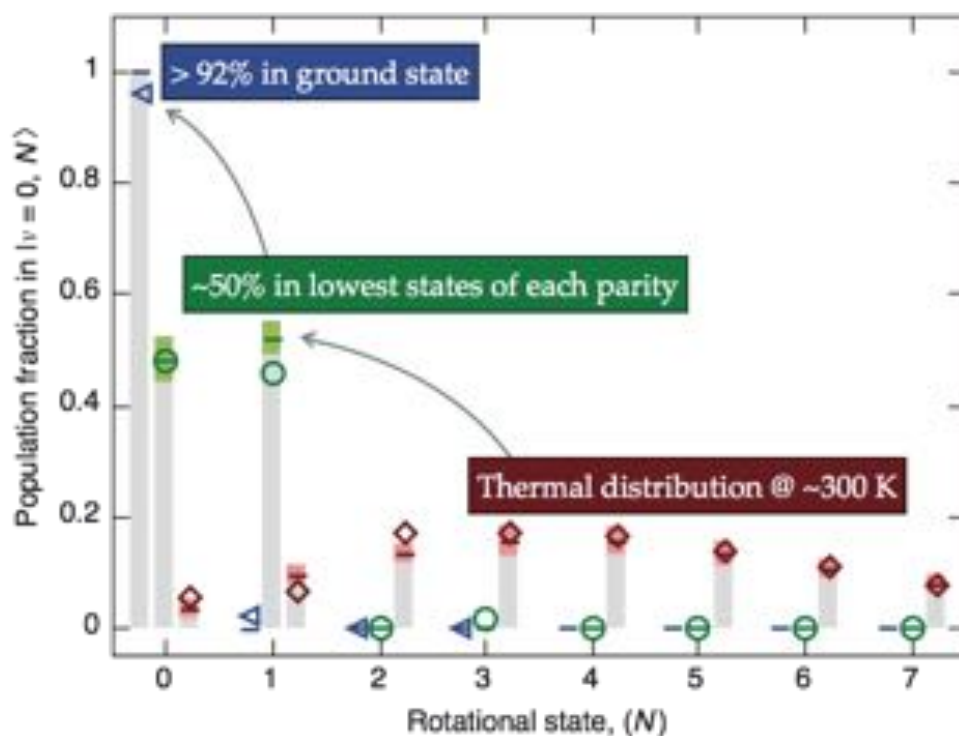


Figure 8.7. Data of cooling AlH^+ . Figure reproduced from Lien *et al.* (2014). Dark red: AlH^+ 's rotational levels are thermally populated up to $N = 7$ at the room temperature. Green: Cooling on the P-branch but the P(1) transition results in population in the $N=0$ and $N=1$. Blue: Further driving the P(1) transition causes the parity flipping via the relaxation through $X, v=1$ and put the population completely in $N=0$.

are populated. With the application of the broadband cooling laser, the population is efficiently pumped into the lower rotational levels. When the laser drives all the P-branch but P(1), the population is pumped into the lowest two rotational states, $N=0$ and $N=1$, about equally as shown in green. The total population in these two states is 94%. The cooling laser application time is 10 ms and is limited by the mechanical shutter's action time. However, the actual cooling time is expected to be $\sim 10 \mu\text{s}$, which is set primarily by the scattering rate and the initial temperature.

The parity barrier between $|N=0\rangle$ and $|N=1\rangle$ is overcome by the vibrational decay from $|X, v'=1\rangle$ to $|X, v''=0\rangle$. Shown in blue, the population from $|N=1\rangle$ is moved into the rotational ground state when P(1) is excited as well. From the inset, we determine that the population falls into the $v=1$ vibrational state and relaxes back to the $v=1$ over ~ 100 ms time scale. In this configuration, the overall cooling efficiency is greater than 95%.

The experiment of cooling of AlH^+ 's rotation proves the feasibility and efficiency of the scheme. As detailed earlier, it is slightly more complicated when applying the scheme to SiO^+ . Not only the spectral filtering resolution needs to be higher, but vibrational repumping might be required. The *B-A-X* branching may play a substantial role in the population dynamics and needs further investigation as well.

8.4. Relaxation and Decoherence

In this section, I introduce the relaxation mechanism of SiO^+ . Of course, the molecular ion is completely lost if chemically reacted. The radioactive relaxation of the rotational state will be discussed in this section as well. Finally, decoherence between $|N=0\rangle$ and $|N=1\rangle$ due to the magnetic field (Zeeman effect) will be briefly introduced.

Chemical Reaction

Regarding the chemical reaction with SiO^+ , the most concerning residual gas in the ultrahigh vacuum environment is H_2 . The rate constant of the reaction



is $3.2 \times 10^{-10} \text{ cm}^3 \text{ s}^{-1}$ at 300 K (Fahey *et al.*, 1981). Therefore, with 10^{-10} Torr partial pressure of H_2 , the reaction rate is $1.2 \times 10^{-3} \text{ s}^{-1}$. This is equivalent to a lifetime of approximately 900 s.

If REMPD is utilized for the internal state analysis, one should consider the chemical reaction with Si^+ as well. Bohme (1990); Fahey *et al.* (1981) studied some of the common reactions. However, those reactions involve molecules that are rare in the UHV, and the reaction rates are all quite small. Therefore, Si^+ is considerably stable during the time between REMPD and the following mass spectrometry.

Radiative Relaxation

Rotational state relaxation due to spontaneous emission or black-body radiation stimulation is discussed here. These two processes are the primary thermalization mechanism of isolated SiO^+ .

We first find the spontaneous decay rate, or equivalently, the Einstein A coefficient between two rotational states in the $X^2\Sigma^+$. The expression of the A coefficient reads

$$\Gamma_s = A_{ki} = \frac{16\nu^3}{3\epsilon_0 hc^3} \sum_i |\langle k | e\vec{r} | i \rangle|^2 \quad (8.4)$$

where ν is the transition frequency and

$$\sum_i |\langle k | e\vec{r} | i \rangle|^2$$

is the sum of the dipole moment squared between the upper state $|k\rangle$ and all possible lower states $|i\rangle$. The transition dipole moment is further approximated as

$$\sum_{m'_J} |\langle X, v=0, N', J' | e\vec{r} | X, v=0, N'', J'', m''_J \rangle|^2 = \frac{1}{g_k} \mu_0^2 f(N', J' | N'', J'') \quad (8.5)$$

where μ_0 is the permanent dipole moment of the state such that

$$\mu_0^2 = |\langle X, v=0 | e\vec{r} | X, v=0 \rangle|^2$$

and $g_k = 2J' + 1$ is the multiplicity of the upper state $|N', J'\rangle$. The factor $f(N', J' | N'', J'')$ is the so-called Hönl-London factor that describes the dependence of the transition probability due to the rotation (Watson, 2008). In the ${}^2\Sigma$ molecule,

$$f(N', J' | N'', J'') = (2J' + 1)(2J'' + 1) \left\{ \begin{matrix} N' & 1 & N'' \\ J'' & 1/2 & J' \end{matrix} \right\}^2 \times (2N' + 1)(2N'' + 1) \left(\begin{matrix} N' & 1 & N'' \\ 0 & 0 & 0 \end{matrix} \right)^2 \quad (8.6)$$

where $\left(\begin{matrix} \cdot & \cdot & \cdot \end{matrix} \right)$ and $\left\{ \begin{matrix} \cdot & \cdot & \cdot \end{matrix} \right\}$ are the Wigner's 3-j and 6-j symbols, respectively.

The transition rate induced by the black-body radiation is computed as

$$\Gamma_{\text{BBR}} = I_T(\nu) B_{ik} \quad (8.7)$$

where

$$I_T(\nu) = \frac{8\pi h\nu^3}{c^3} \frac{1}{\exp(h\nu/k_B T) - 1} \quad (8.8)$$

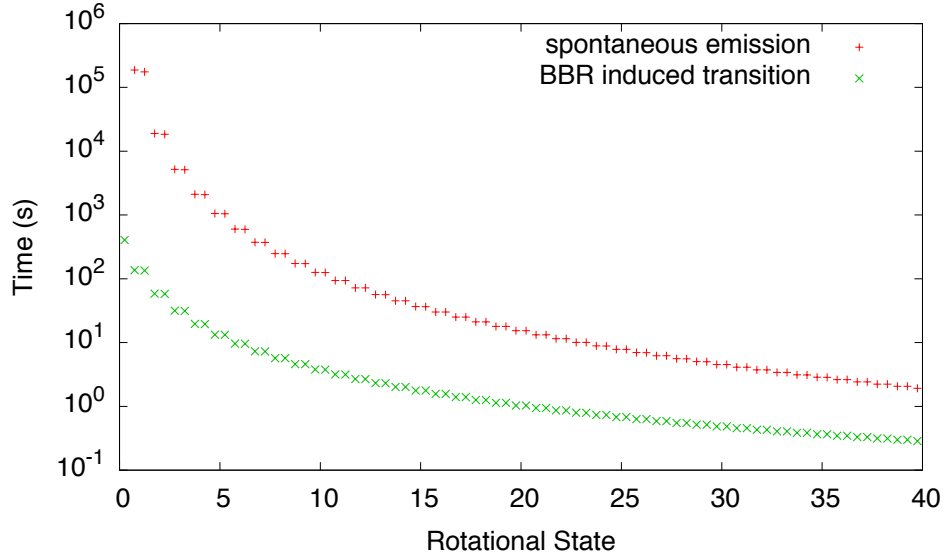


Figure 8.8. Relaxation time due to the spontaneous decay and the BBR-induced transition.

is the black-body spectrum at temperature T and

$$B_{ik} = \frac{g_k}{g_i} \frac{c^3}{8\pi h\nu^3} A_{ki} \quad (8.9)$$

is the Einstein B coefficient of the transition with g_i being the multiplicity of the lower state. Note that the spectrum of the room temperature black-body radiation mostly matches the vibrational transitions in heavier molecules; the black-body radiation drives the rotation of a heavy molecule (such as SiO^+) the least (Vanhaecke and Dulieu, 2007).

The rates of the spontaneous decay (Eq. (8.4)) and black-body induced transition (Eq. (8.7)) in SiO^+ 's $X^2\Sigma^+$, $v=0$ are plotted in Fig. 8.8. The BBR induced transition is found to be the dominated relaxation mechanism.

For the higher rotational levels, the relaxation time is of order 1 s, which determines the thermalization time scale. On the other end, the relaxation time of the ground rotational state is of order 100 s, which sets the T1 coherence time.

Decoherence - Magnetic Field Fluctuation

In the spectroscopy experiment, especially in a Ramsey interferometry, the magnetic field fluctuation causes the phase relaxation and set the T2 coherence time. The origin of the dephasing is the two spectroscopic levels being shifted by the magnetic field differently.

Zeeman effect is considered in the lowest two rotational levels in the $X^2\Sigma^+$ in SiO^+ . We only need to consider the magnetic interaction due to the spin within the $^2\Sigma^+$ manifold. The Hamiltonian of the interaction is therefore

$$\mathcal{H}_1 = -g_s\mu_B B \frac{S_z}{\hbar} = -g_s\mu_B B m_s \quad (8.10)$$

where g_s is the electron g-factor, μ_B is the Bohr magneton, and B is the magnetic field in the z direction. $m_s = S_z/\hbar$ is the spin's magnetic quantum number. The matrix elements in general is (Brown and Carrington, 2003)

$$\begin{aligned} \langle N, S, J, m_J | \mathcal{H}_1 | N, S, J', m_J \rangle &= -g_s\mu_B B (-1)^{J-m_J} \begin{pmatrix} J & 1 & J' \\ -m_J & 0 & m_J \end{pmatrix} \\ &\times (-1)^{J+N+1+S} \begin{Bmatrix} S & J' & N \\ J & S & 1 \end{Bmatrix} [S(S+1)(2S+1)(2J'+1)(2J+1)]^{1/2}. \quad (8.11) \end{aligned}$$

The unperturbed level energies due to the rotation and the spin-rotation interaction are

$$\langle N, S, J, m_J | \mathcal{H}_0 | N, S, J, m_J \rangle = B_e N(N+1) + \frac{\gamma}{2} [J(J+1) - N(N+1) - S(S+1)] \quad (8.12)$$

with the spin-rotation interaction constant γ .

Arrange the basis states in the ascending orders of N , J , and m_J , sequentially. The matrix representation of the full Hamiltonian excluding rotational energy is then

$$\begin{pmatrix} \frac{\epsilon}{2} & 0 & 0 & 0 & 0 & 0 & 0 & 0 \\ 0 & -\frac{1}{2}\epsilon & 0 & 0 & 0 & 0 & 0 & 0 \\ 0 & 0 & -\gamma - \frac{\epsilon}{6} & 0 & 0 & \frac{\sqrt{2}}{3}\epsilon & 0 & 0 \\ 0 & 0 & 0 & -\gamma + \frac{\epsilon}{6} & 0 & 0 & \frac{\sqrt{2}}{3}\epsilon & 0 \\ 0 & 0 & 0 & 0 & \frac{\gamma}{2} + \frac{\epsilon}{2} & 0 & 0 & 0 \\ 0 & 0 & \frac{\sqrt{2}}{3}\epsilon & 0 & 0 & \frac{\gamma}{2} + \frac{\epsilon}{6} & 0 & 0 \\ 0 & 0 & 0 & \frac{\sqrt{2}}{3}\epsilon & 0 & 0 & \frac{\gamma}{2} - \frac{\epsilon}{6} & 0 \\ 0 & 0 & 0 & 0 & 0 & 0 & 0 & \frac{\gamma}{2} - \frac{\epsilon}{2} \end{pmatrix} \quad (8.13)$$

with $\epsilon = g_s \mu_B B$. This matrix is diagonalized to find the level structure under the interaction of the magnetic field. Refer to Table 8.1 for the spectroscopic constants used in the computation for $X^2\Sigma^+$ in SiO^+ .

The level shift in units of MHz as a function of the magnetic field B is plotted in Fig. 8.9. In the weak field regime where the Zeeman interaction is small compared to the spin-rotation interaction, $|N, S, J, m_J\rangle$ remains the energy eigenstate and the energy shift is proportional to the magnetic field. For the strong field, electron spin is aligned and decoupled from the rotation. Hence the $|N, m_N, S, m_s\rangle$ becomes the eigenlevel.

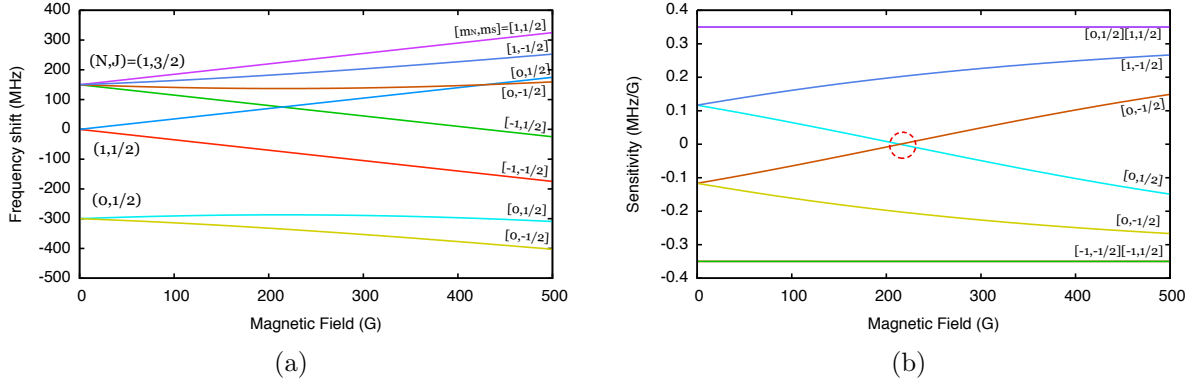


Figure 8.9. Zeeman effect

Figure 8.9(b) plots the sensitivity, the derivative of the energy shift, as a function of B . A field insensitivity transition, indicated by the red circle in the plot, can be found at $B = 214$ G. The corresponding transition is

$$-0.986 |a\rangle + 0.169 |b\rangle \leftrightarrow 0.169 |a\rangle + 0.986 |b\rangle$$

where $|a\rangle = |N=1, J=1/2, m_J=1/2\rangle$ and $|b\rangle = |N=1, J=3/2, m_J=1/2\rangle$. In this configuration, both states have the same slope of energy shift and thus the dephasing is zero to the first order. The second order dephasing, however, is nonzero.

Further discussion on this topic can be found in, for example, Crawford (1934).

8.5. On the Horizon

At the time this dissertation was written, the project of SiO^+ was still ongoing. This section collects some branches of this project that continue the research towards the single ion precision spectroscopy experiment.

Branching Ratio / Spectroscopy

The branching times between $|B, v=0\rangle$ and various vibrational levels in X and A as well as the relaxation times are crucial to the optical pumping scheme for state manipulation of SiO^+ . While the preliminary measurement in Stollenwerk *et al.* (2016) provided the fraction of the $B, v'=0 \rightarrow X, v''=1$ off-diagonal decay, the experiment was not sensitive enough to measure other smaller branches such as the $B-A$ decays.

Patrick Stollenwerk is currently working on an upgraded dispersed fluorescence spectroscopy with trapped species. His apparatus will have a better signal-to-background photon ratio than the previous experiment and hence will improve the detection sensitivity.

It is possible to study the time scales of the vibrational relaxation in X and the $A-X$ decays with trapped SiO^+ . These measurements are usually difficult in a molecular beam spectroscopy due to the short holding time.

Photo-dissociation

In the AlH^+ cooling demonstration, the internal states are read out by REMPD. The fidelity of the REMPD analysis is largely determined by the dissociation probability. Recall that in the REMPD process, the molecule is first resonantly excited to an intermediate state, and then subsequently photo-dissociated. However, if the dissociation step fails (due to probability), the population is not guaranteed to decay back to its original state. Thus, the population distribution is scrambled as REMPD is carried out with low dissociation probability.

The dissociation probability can be calculated as the following. Let σ be the dissociation cross-section of a certain transition, driven by a pulsed laser with energy E per pulse

at wavelength λ . If the laser has a spot radius r , the photon number density per pulse is

$$\frac{E\lambda}{\pi r^2 h c} \quad (8.14)$$

where h is the Planck constant. The dissociation probability is then

$$P = 1 - \exp\left(-\frac{E\lambda\sigma}{\pi r^2 h c}\right) \quad (8.15)$$

in each laser pulse.

For the AlH^+ demonstration, σ is calculated to be $6 \times 10^{-18} \text{ cm}^2$ for the dissociating transition $D^2\Pi$ to $A^2\Pi$ (Seck *et al.*, 2014). The dissociation laser, a 266 nm pulsed YAG, has $E = 2.2 \text{ mJ}$ in each pulse and the beam size is $1000 \mu\text{m}$ by $270 \mu\text{m}$. Therefore, the dissociation probability is 99.6% per pulse, which is quite efficient.

However, for SiO^+ , several dissociation transitions we have considered have a low cross-section. Figure 8.10(a) shows the REMPD cross-sections calculated by Dr. David Tabor in his Ph.D. dissertation (Tabor, 2014). Based on the calculation, a pulsed laser with similar energy would yield a 23% dissociation probability with a typical $\sigma = 2 \times 10^{-19} \text{ cm}^2$, which is not as efficient as the case for AlH^+ . Figure 8.10(b) computes the single shot dissociation probability as a function of pulse energy (in mJ) for 1 mm (green), 0.5 mm (orange), and 0.2 mm (blue) beam radius.

If one wants to apply REMPD to SiO^+ , a possible solution would be applying the laser multiple times to get a higher integrated dissociation probability. In such case, the molecular ion is prepared in the ground rotational state, and the resonant transition in REMPD is the quasi-closed $N'=1 \rightarrow N''=0$ transition in $B-X$. In principle, REMPD

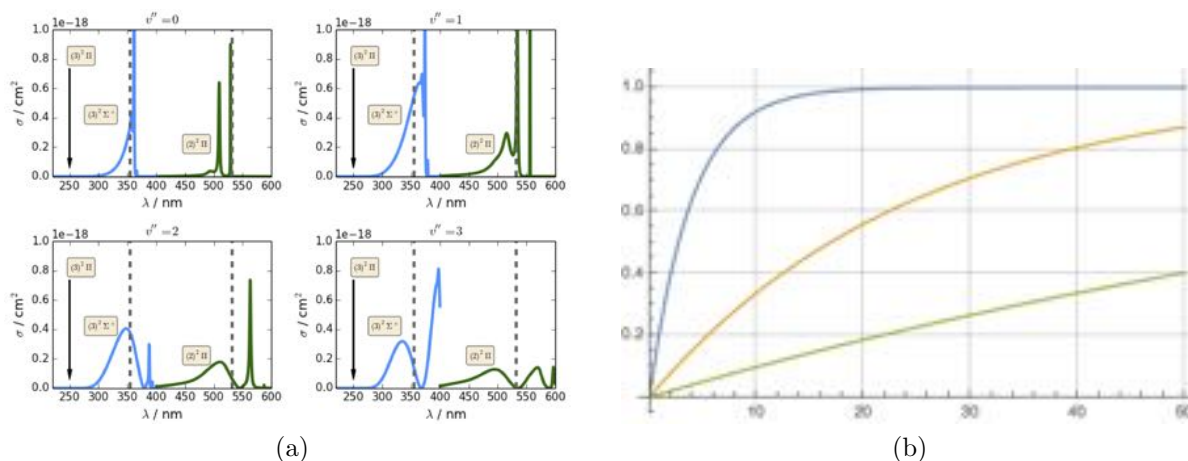


Figure 8.10. SiO^+ dissociation cross-sections from $B^2\Sigma$ to $(2)^2\Pi$ and $(3)^2\Sigma$.

may not be a useful tool for analyzing the internal state distribution, but the measured REMPD spectrum will help improve the ab initio calculation.

Fluorescence Imaging

Direct fluorescence imaging of single isolated molecules has not yet been realized. The challenge is mainly the low fluorescence due to the lack of closed transitions. With both translationally and internally cold SiO^+ , imaging of single molecular ions may be possible with proper repumping of the population from the $X, v \neq 0$ and the A states. Since only a small fraction of the fluorescence is captured, the imaging system needs to operate with low optical aberration such that the limited amount of photons from a single ion can focus onto one or a few pixels. Besides, the use of intensified CCD (iCCD) helps the signal-to-noise ratio at low light level.

Precision Spectroscopy

The ultimate precision spectroscopy with single molecular ion is briefly introduced here. The required techniques have been mostly developed in the laboratory and discussed

in this dissertation. The precision spectroscopy experiment will have several applications such as testing the time-varying proton-to-electron mass ratio.

In short, a single SiO^+ is co-loaded with a single Ba^+ in the trap. Laser cooling of Ba^+ also sympathetically cools the molecular ion to the motional ground state. The internal state of SiO^+ is cooled by the broadband rotational cooling scheme from Section 8.3. With the population in the ground state, one can do the microwave rotational spectroscopy at 43 GHz. The vibrational transition between $v=0$ and $v=1$ in X at $8\ \mu\text{m}$ might be difficult due to the laser. Next, the spectroscopy result can be read out by the motional seeding technique from Chapter 5; the quantum logic spectroscopy technique can be performed as well (Schmidt *et al.*, 2005).

CHAPTER 9

Spectral Filtering**9.1. Introduction**

The coherent broadband nature of ultrashort pulsed lasers greatly increases the bandwidth of interaction between the laser and a subject. Ultrashort pulse shaping technology further advances the degree of such interaction in many applications. For instance, in optical communication, pulse shaping technology is used to encode information and perform computation (Sardesai *et al.*, 1998). It is also used to correct and optimize the phases of the spectrum for generating high-quality ultrashort pulsed lasers (Pastirk *et al.*, 2006). In controlling chemistry, an ultrashort pulse laser with a programmed waveform provides delicate control of molecules (Goswami, 2003; Sauer *et al.*, 2007).

In our laboratory, we have been applying the pulse shaping technique to our molecular rotational state cooling experiment (Lien *et al.*, 2014, 2011). The principle of rotational cooling is the optical pumping of transitions associated with losing rotational angular momentum (P-branch) while avoiding those diffusing (Q-branch) or heating (R-branch) the rotational population. This can be done by shaping a femtosecond laser's spectrum with a filter of which the P-branch is in the passband and the Q- and R-branch is in the stopband, as illustrated in Fig. 9.1. The cutoff width of the filter determines how well one can avoid driving an unwanted transition, and ultimately determines the molecular cooling efficiency.

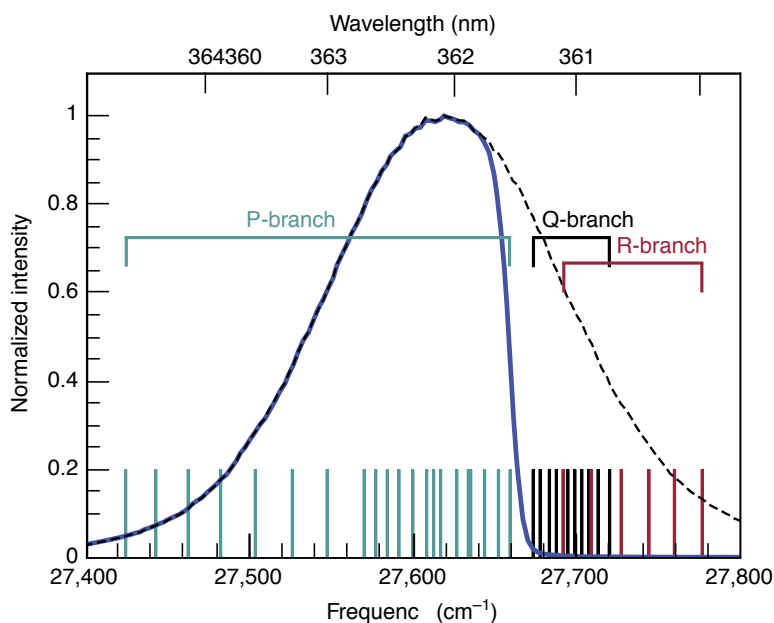


Figure 9.1. Rotational cooling with spectral-filtered broadband source. In this example, relevant transitions from $A^2\Pi_{1/2}, v'=0 \leftarrow X^2\Sigma_{1/2}, v''=0$ band in the AlH^+ are shown as vertical bars at the bottom. P-branch is the rotational cooling transitions, while Q- and R-branch are the opposite. An unfiltered UV femtosecond laser (spectrum shown as dashed line) drives all transitions thus provides no cooling effect. A filtered source (spectrum shown as solid line) drives only cooling transitions and hence slows down the molecule's rotation.

Ultrashort pulse shaping is the optical version of a waveform synthesizer. A typical implementation is similar to an optical spectrometer. The setup first Fourier transforms the input laser to obtain its optical spectrum with a dispersive element. Then, the angularly dispersed light is focused by a lens (or a concave mirror) to map the dispersion onto the focusing plane, where the spectrum is altered by a light modulator. Finally, the inverse Fourier transform is performed with another set of lens and dispersive element to form the output laser pulse with the desired spectrum or time-domain waveform.

High-resolution pulse shaping techniques have been the focus of ultrafast laser research for over two decades. Usually, the pulse shaping frequency resolution $\delta\nu$ is compared to the bandwidth $\Delta\nu$ of the unshaped laser as the figure of merit; the ratio $\eta = \Delta\nu/\delta\nu$ measures the number of pulse shaping control parameters. However, in our research where the laser is used to drive transitions, it is necessary to compare $\delta\nu$ to the molecular structure. Therefore, we emphasize the absolute frequency resolution rather than the fractional. One of the earliest pulse shaping implementations achieved ≈ 0.2 nm (51 GHz) resolution at 1064 nm (Thurston *et al.*, 1986). For the Ti:Sapphire laser wavelength (800 nm), modulation at around 0.1 nm (48 GHz) has been reported in (Monmayrant and Chatel, 2004; Stobrawa *et al.*, 2001). Recently, with the introduction of virtually imaged phase arrays (VIPAs), pulse shaping reached a few GHz resolution at similar wavelength (Lee *et al.*, 2006; Supradeepa *et al.*, 2008). In the UV regime, there was, however, slower progress due to the lack of suitable light modulators. Yet, sub-nm resolution (>200 GHz) has been demonstrated at some UV wavelengths (Weber *et al.*, 2010). In all these experiments, pulse shaping resolution does not necessarily include information about modulation extinction contrast. The cutoff feature of the amplitude modulation was seldom mentioned. For cooling molecules with a pulse-shaped laser to work for heavier molecules such as oxides or fluorides, resolution better than 100 GHz with high extinction ratio is required and is the main goal of this work.

In this paper, we explore spectral filtering of a near UV femtosecond laser by providing an introductory element-wise investigation of the setup. We first briefly review the theory of ultrashort pulse shaping in the next section. Then, we investigate each component used in our setup in Section 9.3. The evaluation and calibration of our spectral filtering are

in Section 9.4. In passing, this work is towards our molecular cooling experiment with SiO^+ , for which some parameters are picked. Specifically, the relevant transitions are at 385 nm, and the rotational heating and the cooling transitions are simply separated by an 84 GHz gap.

9.2. The Spectral Filtering Setup

Our broadband spectral filtering setup is shown in Fig. 9.2(a). The unfiltered laser source is coupled into the setup by folding mirrors M1 and M2. Grating G1 and lens L2 Fourier transform the light and produce the laser spectrum. Specifically, the grating separates each spectral component into different angles. When focused by the lens, each component becomes a spot at different locations on the focusing plane, which makes the (optical) frequency plane. See Fig. 9.2(b). Filtering is achieved by masking the spectrum at the plane. The filtered spectrum is recombined into a single beam by L3 and G2, which performs the inverse Fourier transformation. The output beam is further reshaped with a telescope (M4 and L4) to a proper size for future experiments.

The ultrashort pulse shaping technique has been greatly reviewed in several articles including (Monmayrant *et al.*, 2010; Weiner, 2011). Here we highlight the key results. Consider a Gaussian input beam with $1/e^2$ beam radius w_i . A spectral component of wavelength λ makes a focused spot with beam radius

$$w_o = \frac{\cos \theta_i}{\cos \theta_d} \frac{f \lambda}{\pi w_i} \quad (9.1)$$

at the frequency plane. In the above equation, f is the focal length of the lens; θ_i and θ_d are the incident and diffraction angle at the grating, respectively. The dispersion at the

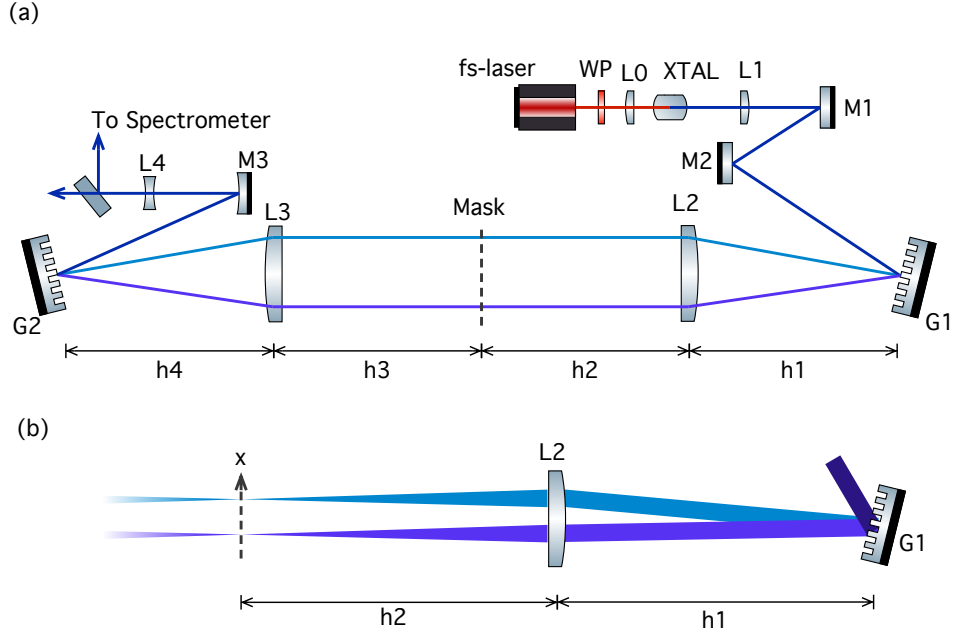


Figure 9.2. Schematic of our spectral filtering setup. fs-laser: mode-locked femtosecond laser; WP: half-wave plate; XTAL: BBO SHG crystal; L1-4: lens; M1-3: mirrors (M3 is concave). G1 and G2 are reflective diffraction gratings; C: fiber coupler. See text for detailed discussion.

frequency plane is

$$\frac{dx}{d\nu} = \frac{\lambda^2 f}{cd \cos \theta_d} \quad (9.2)$$

where d is the pitch of the grating groves. The pulse shaping resolution is then the frequency extent across the spot:

$$\delta\nu = w_o \times \frac{d\nu}{dx} = \frac{cd \cos \theta_i}{\pi \lambda w_i}. \quad (9.3)$$

As a numerical example, we consider an input beam with $\lambda = 385$ nm and $w_i = 5$ mm. We assume $\theta_i = \theta_d - 10^\circ = 49.1^\circ$. With $f = 500$ mm lens and 2400 groves/mm grating, the focus size is $w_o = 15.6$ μm and the frequency resolution is $\delta\nu = 13.5$ GHz. In this example, the theoretical spectral filtering resolution will be sufficient for the SiO^+ cooling

experiment. The resolution is entirely set by the grating density and the input beam size, independent to the imaging lens. However, the focus size and the dispersion are proportional to the focal length f . If a lens with shorter f is used, the smaller spot size becomes difficult to mask in terms of mechanical resolution. On the other hand, using a longer f reduces the mechanical challenge but increases the setup's footprint and requires larger optics, which makes optical aberration become an issue. Our choice of $f = 500$ mm represents a compromise between the above two concerns, along with other matters discussed later.

The theoretical treatment of an ultrashort pulse system by the Wigner function is a well-established method (Paye and Migus, 1995; Wefers and Nelson, 1996). On the other hand, the response of the optics can be described by the optical transfer function (OTF). The combination of these two thus provides the comprehensive theoretical study of a real world pulse shaper. However, most of the previous works adopted the paraxial approximation such that aberrations were not considered at all. Here, we only point out but skip the theoretical investigation as it is outside the scope of our experimental work.

9.3. Setup

In this section, we introduce and comment on components in our spectral filtering setup as well as the alignment procedure.

9.3.1. Light source

The input 385 nm broadband source is the second harmonic generation (SHG) of a mode-locked femtosecond laser (Spectra Physics Mai-Tai). This is done by focusing the fundamental (770 nm) light with an $f = 30$ mm achromatic lens onto a thin (0.5 mm) BBO crystal (Zhang *et al.*, 1998; Ghotbi and Ebrahim-Zadeh, 2004; Ghotbi *et al.*, 2004). The UV beam from the crystal is collimated by a doublet lens with approximately 400 mm effective focal length. We found it is sufficient to compare the beam size at near and far fields to determine collimation. The collimated UV beam's radius is 4.8 mm beam horizontally and 5.7 mm vertically. The results were obtained by the knife edge beam size measurement. The data presented an acceptable Gaussian intensity distribution.

We noticed that the UV beam acquires dispersion from the SHG process, most likely due to the walk-off. We then set up the SHG such that the dispersion is aligned to the grating's dispersion direction, and accommodate such initial dispersion with the pulse shaper. Further discussion continues in Section 9.3.5.

9.3.2. Grating

We use holographic gratings with 2400 groves/mm in our spectral filtering setup. These gratings are set up in a close to Littrow configuration: the incident angle is $\theta_i = 47.1^\circ$ and the diffraction angle is $\theta_d = 40.9^\circ$ at $\lambda = 385$ nm. While our choice of the grating is due to component availability, a grating with higher density is of course preferred. We would avoid ruled gratings as they are prone to periodic and irregular ruling errors that result in ghosting and stray light and hurt the filtering resolution. However, blazed ruled

gratings can be more efficient; our holographic grating has about 1/2 diffraction efficiency and is the least efficient component in the setup.

9.3.3. Focusing lens

A large aperture lens is used to accommodate the broadband light, which is a few centimeters wide at L2. In such case, all types of optical aberration can be easily picked up and makes the focus less tight. Spherical aberration is the dominant type. For tilted incident, astigmatism is somewhat less problematic in one-dimensional pulse shaping. Coma, on the other hand, produces a comet-like spot shape that indeed corrodes the resolution in an asymmetric fashion. Lastly, we safely ignore chromatic aberration since $\Delta\lambda \approx 2 \text{ nm} < \lambda = 385 \text{ nm}$. Although there is a quality spectrum of stocked optics available from visible to IR wavelength, off-the-shelf optics for our application in UV is quite limited. The option to be considered is the combining of spheric lenses into a doublet lens to reduce all types of aberration mentioned above. Constructing a doublet lens usually involves using two different glasses and optimizing the curvatures of each surface. While we have access to only some 2" fused silica lenses, our doublet lens is constructed by stacking a positive meniscus lens (Thorlabs LE4822) on a plano-convex lens (Thorlabs LA4337). The effective focal length of this doublet is around 500 mm.

9.3.4. Mask

The SiO^+ rotational cooling requires a simple low-pass filtering mask, which is realized by a razor blade. Installing the mask is straightforward as we place the mask at the location where best resolution is obtained. That is, the longitudinal location of the blade



Figure 9.3. Microscope images of three samples of razor blades used in this experiment. While we image the blades (gray area) in front of a dark background, the boundary between two areas is due to the blade edge. It is easy to see the fuzziness of the blade edge is around $1\ \mu\text{m}$, smaller than the focal spot size ($\sim 10\ \mu\text{m}$) in our setup.

is searched, while the transverse one is set to a specific cutoff frequency based on the molecule. The knife edge is set vertically but a little tilt is not too critical as it will soften the cutoff by $1/\cos\theta$, which is tiny for small tilt angle θ . We inspected the razor blades under a microscope (see Fig. 9.3) and found typical edge roughness is of order $1\ \mu\text{m}$ - smaller than the focal spot size. Hence the quality of the blade edge is not yet the limiting factor to our spectral filtering resolution. But we would avoid a used blade because of the likely worn knife edge.

9.3.5. Dispersion compensation

The output beam acquires dispersion because the second grating G2 does not properly recombine the filtered spectrum. The mathematical description follows. We start with

the grating diffraction equation at G2:

$$d(\sin \theta_i + \sin \theta_d) = \lambda. \quad (9.4)$$

By expanding the above equation to the first order in $\delta\theta_i$, $\delta\theta_d$, and $\delta\lambda$, we obtain the first order dispersion:

$$\frac{\delta\theta_d}{\delta\lambda} = \frac{1}{d \cos \theta_d^0} - \frac{\cos \theta_i^0}{\cos \theta_d^0} \frac{\delta\theta_i}{\delta\lambda} \quad (9.5)$$

with

$$d(\sin \theta_i^0 + \sin \theta_d^0) = \lambda_0 \quad (9.6)$$

being the diffraction condition at the center wavelength λ_0 . The term $\delta\theta_i/\delta\lambda$ on the right hand side of Eq. (9.5) is used to characterize the propagation of filtered spectral components when they merge onto the grating. The output beam is dispersion-free when $\delta\theta_d/\delta\lambda = 0$ and is fulfilled at a specific grating angle

$$\theta_i^0 = \cos^{-1} \left[\frac{1}{d} \left(\frac{\delta\theta_i}{\delta\lambda} \right)^{-1} \right]. \quad (9.7)$$

Qualitatively, Fig. 9.4 illustrates some possible scenarios. (a) is the flawless case where the input beam has no dispersion and the optics are matched pairs. In this case, a symmetric 4-f line is aligned and can be reduced to a 2-f configuration by retro-reflecting the filtered spectra at the frequency plane. In (b), the distance $h1$ is slightly off f such that each spectral component does not propagate in parallel between L2 and L3. This angular error eventually results in the output beam's dispersion if G2 is not adjusted correspondingly. (c) shows the general situation where the source of error includes the input laser already carrying dispersion and optical elements not being identical. As explained earlier,

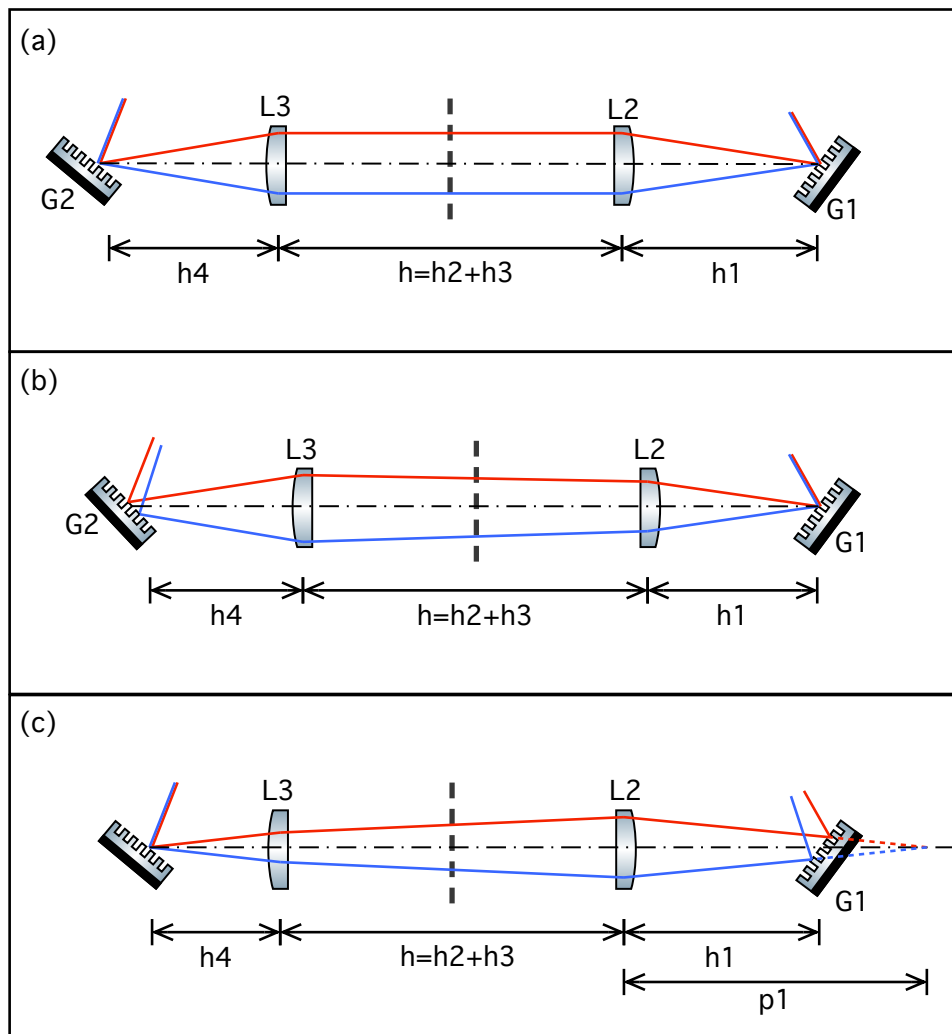


Figure 9.4. Some possible scenarios regarding dispersion in the 4-f line. The red and the blue lines represent the propagation path of two different spectral components. (a) is an ideal case where the input beam is dispersion-free and $G1=G2$ and $L2=L3$. In (b), the alignment of some components is off, and hence the output beam derives dispersion. In general, as in (c), the source of dispersion can come from the input beam and errors from components and alignment. However, dispersion can be compensated by properly aligning the location and the diffraction angle of the grating G2.

the sum of all these errors is compensated by optimizing the location and the angle of the recombining grating G2. It is worth mentioning that the input laser's dispersion alone

can be corrected beforehand. Here, we simply delay that task as we can correct for some other errors as well. Other than this aspect, the 4-f configuration is expected to have equal performance as a 2-f configuration.

9.3.6. Alignment

We align elements in the 4-f line sequentially. After grating G1, the focusing lens L2 is set approximately one focal length away without further optimization. The location of L3 is adjusted such that the two lenses (L2 and L3) form a 1:1 Galilean telescope.

The recombining grating G2 should be placed where all spectral components merge; its angle is tuned to diffract all components into the same direction. To check the alignment, we use a mask with two tiny slits to select only components from both ends of the spectrum. We then optimize the grating until these spectral components form an overlapped output. For example, if one sees two spots, the location of the grating needs adjustment. Furthermore, when two spots travel at crossing paths, we know the diffraction angle is off. After G2 is optimized, the recombined output beam remains a single spot over a long propagation distance.

9.4. Evaluation and Calibration

9.4.1. Spectrometer

In order to diagnose our spectral filtering, we also built a high-resolution spectrometer as outlined in Fig. 9.5. The input light is coupled into the spectrometer by a single mode fiber and is collimated to 6.8 mm beam radius. We use 3600 grooves/mm ruled grating in our spectrometer. The focusing lens L5 is the same as the one in spectral filtering.

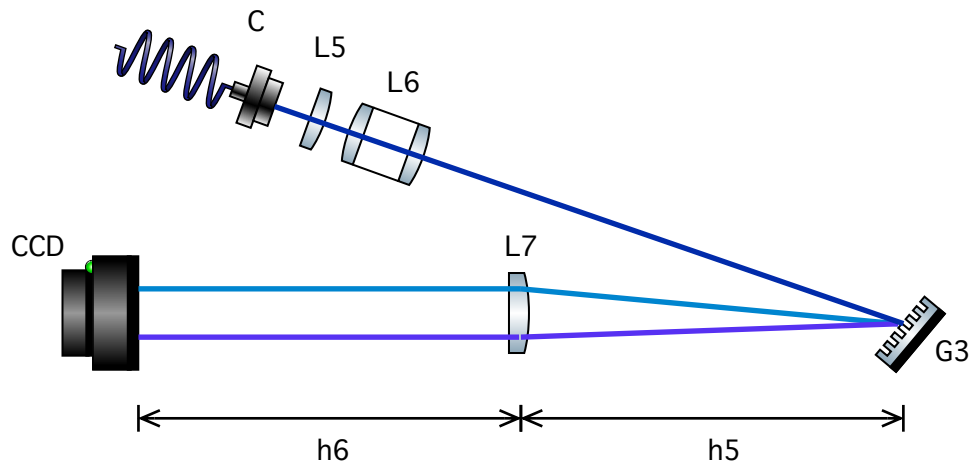


Figure 9.5. Schematic of our spectrometer. C: fiber output coupler; L5-6: collimation lens; G3: diffraction grating; L7: focusing lens; CCD: linear camera.

A linear camera is placed on the frequency plane to record the spectrum; it has 3648 pixels and each is $8\ \mu\text{m}$ wide and $200\ \mu\text{m}$ tall. Based on the data presented later, the $1/e^2$ -full-width frequency resolution of this spectrometer is 28 GHz.

Our homebuilt spectrometer was also the test bed for the focusing lens. The evaluation incorporated a narrowband CW laser to produce a single spectral component on the frequency plane. We took this approach to check the performance of our homebuilt doublet lens.

9.4.2. Permissible input beam size

In Fig. 9.6 we measure the profile of the focal spot for two different input beam sizes: $w_i = 6.8\ \text{mm}$ (left) and $12.1\ \text{mm}$ (right). (The input beam size is controlled by the fiber collimation lens.) In both cases, a compact Gaussian-like peak is observed. But the profile due to the larger beam also has additional tails next to the central peak. As the extra

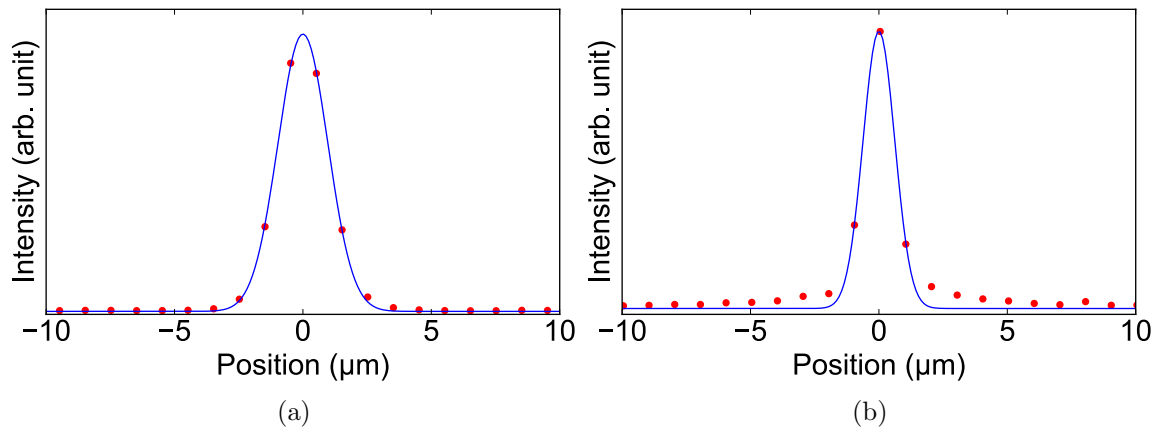


Figure 9.6. Intensity profile on the focusing plane of a narrowband laser, recorded by a line camera. A large input beam size $w_i = 12.1$ mm is used in the right panel, and causes the focal spot to be less compact. While in the left, a permissible beam size $w_i = 6.8$ mm is used, and the focal spot profile is fairly close to Gaussian.

feature contains non-negligible intensity, it significantly degrades the resolution even when a larger beam is supposed to be more tightly focused. In spectral filtering, the tail results in a low extinction cutoff.

The origin of the tail is mostly from the transverse spherical aberration, which grows rapidly as the cube of the aperture size. Spherical aberration limits the clear aperture of an optics for tight focusing. From the above result, we learned that any input beam with $w_i < 6.8$ mm should acquire only modest spherical aberration. Our homebuilt doublet lens is then satisfactory in this project as the broadband UV beam size (refer to Section 9.3.1) fits into its clear aperture.

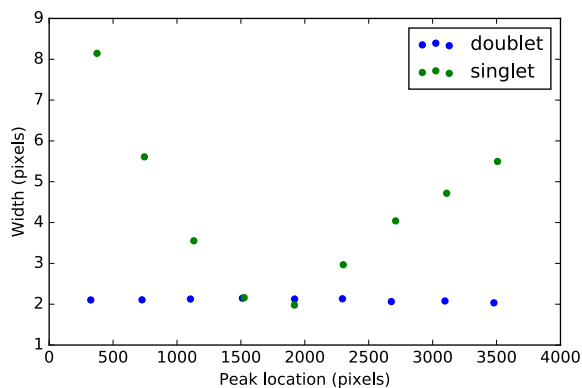
9.4.3. Other aberrations

In this section, we exam the focusing behavior for spectral components that access the lens off-center. A different narrowband spectral component can be obtained by changing the wavelength of the CW laser. It, however, requires a fancy laser system to modulate the laser wavelength over several nanometers. Therefore, to simulate tilted beams due to different wavelengths, we rotated the grating instead. We measured the focal spot profile for various diffracted beam pointing in Fig. 9.7. For comparison, we performed the same measurement with a singlet lens as well. In (a) we have the peak width on the camera versus different tilt; in (b) some sample spot profiles at various tilts are presented. The focal spot size stays around 16 μm over an approximately $\pm 2^\circ$ tilt with the doublet lens, while it varies quite a lot with the singlet lens. The result shows us that we can expect a relatively consistent resolution over the entire spectral range both in the spectrometer and the spectral filtering setup.

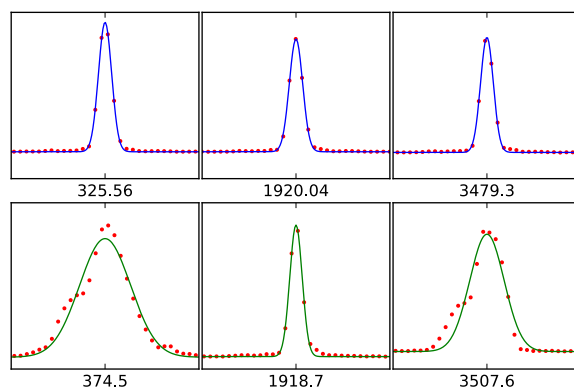
From the same data we also calibrate the spectrometer's linear dispersion. We first read the peak locations for each tilt from Fig. 9.7(b) and fit to a straight line. Then we computed the angular dispersion due to the grating in this spectrometer. With both pieces of information, we obtained the calibration 7.2 GHz/pixel. In addition, the focal spot size converts to a 14 GHz spectral resolution in our spectrometer.

9.4.4. spectral filtering

With the spectrometer and the focusing lens characterized, we now turn the attention to the overall performance of our spectral filtering. We sent a few percent of the output light power into our spectrometer for diagnosis. In Fig. 9.8 we see the output spectrum with



(a)



(b)

Figure 9.7. (a) Consistency of spectrometer resolution over its measurement range. In this test, we simulate different narrowband laser wavelengths by rotating the grating, as if the diffraction angle is changed due to another wavelength. (b) Spot profiles for data #1 (left-most), #5 (middle), and #9 (right-most) from the data sequence in (a). The horizontal axis is the pixel number on the linear camera. The spots in the upper row are focused by the doublet lens and those in the bottom row are focused by the singlet lens. The width of each plot is 30 pixels.

(green line) and without (red line) masking. The unfiltered spectrum has a Gaussian-like overall shape. The origin of the fringes on top of the profile is not yet clear to us. However, we were able to see the same fringes right after the UV generation crystal, therefore our best guess is it might come from the second harmonic generation process. Without further

knowledge of the fringes, we simply model the feature as a sinusoidal modulation to the Gaussian function:

$$A \exp\left(-\left(\frac{\nu - \nu_c}{\Delta\nu}\right)^2\right) \times \left[1 + h \sin\frac{2\pi(\nu - \nu_p)}{\Omega}\right] \quad (9.8)$$

where ν_c is the broadband laser center frequency, $\Delta\nu$ is the laser bandwidth, Ω is the fringe period, ν_p is used to adjust the fringe's offset, and h is the modulation index. The unfiltered spectrum has $\Delta\nu = 7.1$ THz full-width-half-maximum bandwidth, and the period of the fringes is around $\Omega = 150$ GHz.

For the cutoff, we model it with an error function

$$g(\nu, \nu_0) = g(\nu - \nu_0) = \frac{1}{2} \left[\operatorname{erf}\left(\frac{\nu - \nu_0}{\sqrt{2}\delta\nu}\right) + 1 \right] \quad (9.9)$$

where ν_0 is the cutoff frequency and $\delta\nu$ is the cutoff width. Positive $\delta\nu$ represents a high-pass mask and negative $\delta\nu$ is low-pass. The error function is a natural choice in our analysis as the edge of the mask partially blocks a Gaussian beam. Fig. 9.8(b) shows a typical filtered spectrum near the cutoff with our model applied to the data. In this demonstration, the cutoff width $\delta\nu$ is 48 GHz. Compared to the expected diffraction-limited resolution, this result is 33% worse.

In Fig. 9.9 we measure the width $\delta\nu$ for different mask longitudinal locations z . The result is modeled by

$$\delta\nu(z) = \delta\nu_0 \sqrt{1 + \left(\frac{z - z_0}{z_R}\right)^2} \quad (9.10)$$

which resembles the equation for Gaussian beam width evolution. The range $z_R = \pm 11.2$ mm is considered the alignment tolerance of the mask.

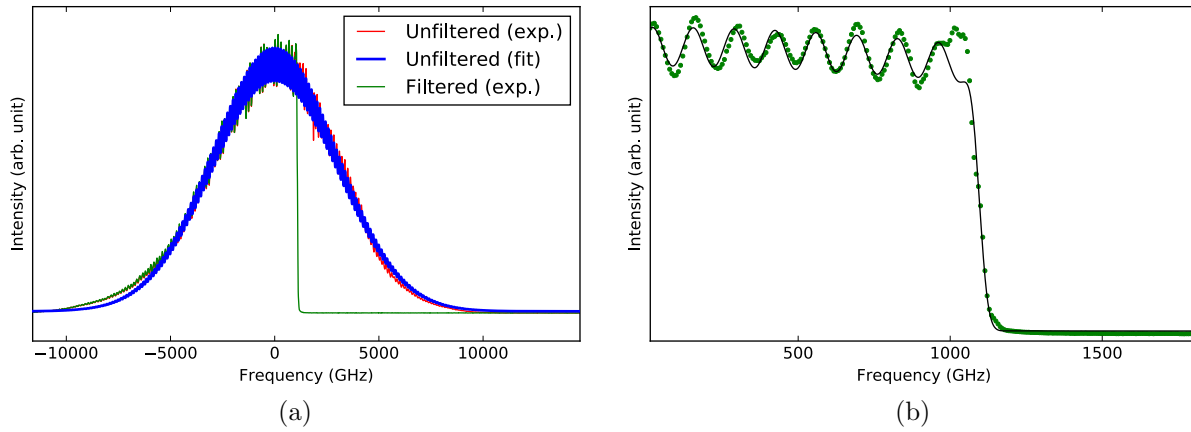


Figure 9.8. Spectrum of the original and filtered light.

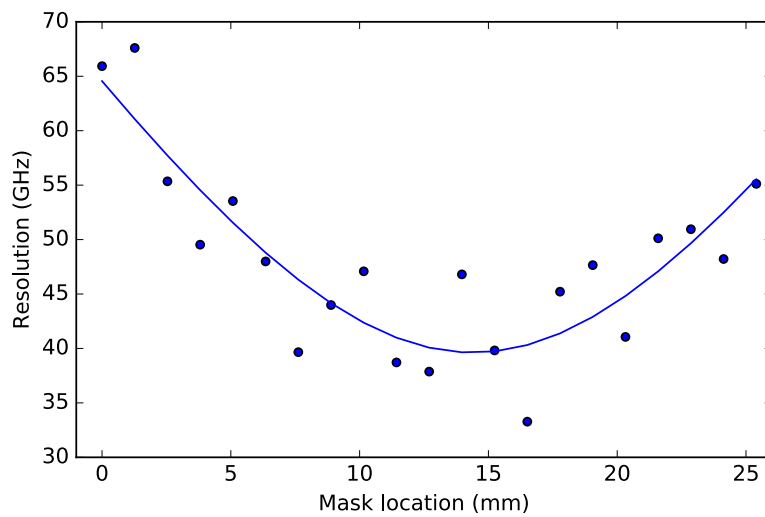


Figure 9.9. Cutoff resolution versus mask longitudinal position.

We also measured the cutoff behavior at different cutoff frequencies to test the consistency over the spectrum. We found the cutoff frequency is related to the blade's transverse position by $1.6 \text{ GHz}/\mu\text{m}$; this is also a measurement of the linear dispersion of our spectral filtering setup. In Fig. 9.10 we plot the cutoff width as a function of cutoff frequency.

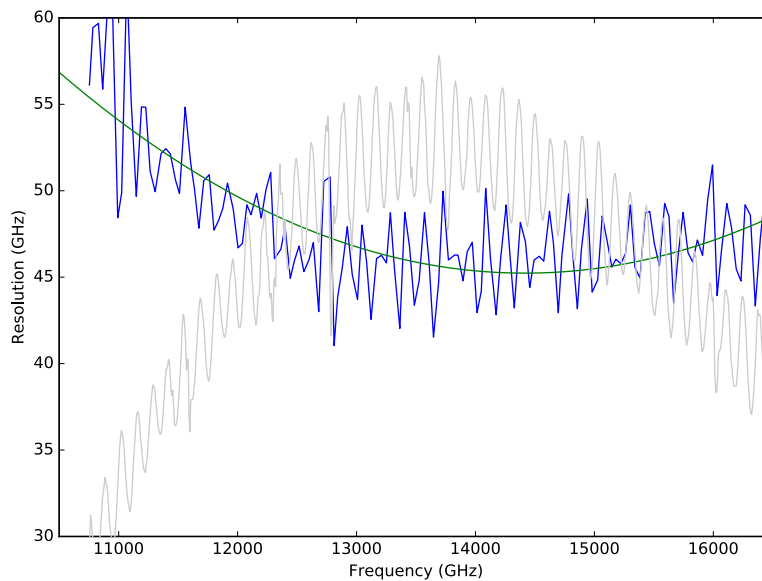


Figure 9.10. cutoff resolution versus different cutoff frequency.

We notice that the cutoff width varies rapidly across the laser spectrum, and the variation coincides with the spectral fringes from the unfiltered light, shown in the gray line. As we currently have no plausible explanation for the fringes, we cannot understand the correlation either. Regardless, by eye-averaging the result, we find the cutoff resolution is worsened by around 20% when away from the central wavelength, which can be attributed to the optical aberration.

9.5. Improvement

We have demonstrated that the focusing lens is the key component in both the spectrometer and the spectral filtering setup. In this project, we used standard optics components available from common vendors, which significantly limited the ability of aberration correction. The immediate also less expensive solution is to build a doublet lens with proper choices of lens materials and surface curvatures. By doing optical ray tracing

simulations, we, however, found that, for doublet lenses utilizing spherical surfaces, the largest clear aperture diameter is somehow around 20 mm. The performance seems to be limited by the number of tuning variables in lens design. That is, if one wants to work with larger input beam size, it is necessary to use aspheric optics.

The input beam shape is another factor that might need more studying. While SHG of a femtosecond laser is quite simple, we have observed evidence of beam shape degradation. The obvious one is astigmatism where the UV beam presents an elliptical shape. In addition, the UV beam is accompanied by a halo; it is not clear to us how this scattered light behaves in the pulse shaping setup and affects the filtering resolution.

To ultimately reach close to the diffraction limit, wavefront distortion caused by, e.g., optics surface irregularity, is yet another obstacle to be studied and overcome.

Finally, regarding the mask, a razor blade serves as an adequate bandpass filter for our molecular cooling experiment. For comprehensive modulation, a spatial light modulator (SLM) is a better option. SLMs with good resolution and dynamic range have become available in the UV band. Options to be considered for our future experiment include liquid crystal (Tanigawa *et al.*, 2009), acousto-optic modulator (Roth *et al.*, 2005; Pearson and Weinacht, 2007), and micro-mirror array (Rondi *et al.*, 2009).

References

- Agap'ev, B. D., M. B. Gornyi, B. G. Matisov, and Y. V. Rozhdestvenskiĭ (1993), *Physics-Uspekhi* **36** (9), 763.
- Appelhans, A. D., and D. A. Dahl (2002), *Int. J. Mass. Spectrom.* **216** (3), 269.
- Arnesen, A., A. Bengtsson, R. Hallin, S. Kandela, T. Noreland, and R. Lidholt (1975), *Phys. Lett. A* **53** (6), 459.
- Arroe, O. (1950), *Phys. Rev.* **79** (5), 836.
- Bahns, J., W. Stwalley, and P. Gould (1996), *J. Chem. Phys.* **104** (24), 9689.
- Berkeland, D. J., J. D. Miller, J. C. Bergquist, W. M. Itano, and D. J. Wineland (1998), *J. Appl. Phys.* **83** (10), 5025.
- Biercuk, M. J., H. Uys, J. W. Britton, A. P. VanDevender, and J. J. Bollinger (2010), *Nat. Nanotechnol.* **5** (9), 646.
- Bohme, D. K. (1990), *Int. J. Mass. Spectrom.* **100**, 719.
- Brown, J. M., and A. Carrington (2003), *Rotational Spectroscopy of Diatomic Molecules* (Cambridge University Press).
- Cai, Z. L., and J. P. Francois (1999), *J. Mol. Spectrosc.* **197** (1), 12.
- Cameron, R., T. Scholl, L. Zhang, R. Holt, and S. Rosner (1995a), *J. Mol. Spectrosc.* **169** (2), 352.
- Cameron, R., T. J. Scholl, L. Zhang, R. A. Holt, and S. D. Rosner (1995b), *J. Mol. Spectrosc.* **169** (2), 364.
- Chattopadhyaya, S., A. Chattopadhyay, and K. K. Das (2003), *J. Mol. Struc.-Theochem* **639** (1), 177.
- Chen, X., Y. Lin, and B. Odom (2015), *New J. Phys.* **17** (4), 043037.

- Chieda, M., and E. Eyler (2011), *Phys. Rev. A* **84** (6), 063401.
- Chou, C., D. Hume, J. Koelemeij, D. Wineland, and T. Rosenband (2010), *Phys. Rev. Lett.* **104** (7), 070802.
- Clark, C. R., J. E. Goeders, Y. K. Dodia, C. R. Viteri, and K. R. Brown (2010), *Phys. Rev. A* **81** (4), 043428.
- Colbourn, E., J. Dyke, E. Lee, A. Morris, and I. Trickle (1978), *Mol. Phys.* **35** (3), 873.
- Crawford, F. (1934), *Rev. Mod. Phys.* **6** (2), 90.
- Curry, J. (2004), *J. Phys. Chem. Ref. Data* **33** (3), 725.
- Davidson, M., L. Snoek, H. Volten, and A. Dönszelmann (1992), *Astron. Astrophys.* **255**, 457.
- Ding, S., and D. Matsukevich (2012), *New J. Phys.* **14** (2), 023028.
- Doroshenko, V. M., and R. J. Cotter (1997), *J. Mass. Spectrom.* **32** (6), 602.
- Drewsen, M., A. Mortensen, R. Martinussen, P. Staantum, and J. L. Sørensen (2004), *Phys. Rev. Lett.* **93** (24), 243201.
- Dzuba, V., and J. Ginges (2006), *Phys. Rev. A* **73** (3), 032503.
- Fahey, D., F. Fehsenfeld, E. Ferguson, and L. Viehland (1981), *J. Chem. Phys.* **75** (2), 669.
- Flambaum, V., and A. Tedesco (2006), *Phys. Rev. C* **73** (5), 055501.
- Ghosh, P. (1995), *Ion traps* (Clarendon Press; Oxford (United Kingdom)).
- Ghosh, S., J. V. der Linde, and R. Verma (1979), *J. Mol. Spectrosc.* **75** (2), 169 .
- Ghotbi, M., and M. Ebrahim-Zadeh (2004), *Opt. Express.* **12** (24), 6002.
- Ghotbi, M., M. Ebrahim-Zadeh, A. Majchrowski, E. Michalski, and I. Kityk (2004), *Opt. Lett.* **29** (21), 2530.
- Godun, R., P. Nisbet-Jones, J. Jones, S. King, L. Johnson, H. Margolis, K. Szymaniec, S. Lea, K. Bongs, and P. Gill (2014), *Phys. Rev. Lett.* **113** (21), 210801.
- Goldfarb, R. B., and H. E. Bussey (1987), *Rev. Sci. Instrum.* **58** (4), 624.

- Goswami, D. (2003), Phys. Rep. **374** (6), 385.
- Grimm, R., Y. B. Ovchinnikov, A. I. Sidorov, and V. S. Letokhov (1990), Phys. Rev. Lett. **65** (12), 1415.
- Gurell, J., E. Biémont, K. Blagoev, V. Fivet, P. Lundin, S. Mannervik, L.-O. Norlin, P. Quinet, D. Rostohar, P. Royen, *et al.* (2007), Phys. Rev. A **75** (5), 052506.
- Horowitz, P., W. Hill, and I. Robinson (1980), *The art of electronics*, Vol. 1989 (Cambridge university press Cambridge).
- Hume, D. B., C. W. Chou, D. R. Leibbrandt, M. J. Thorpe, D. J. Wineland, and T. Rosenband (2011), Phys. Rev. Lett. **107** (24), 10.1103/PhysRevLett.107.243902.
- Hunt, F. J. (1976), J. Phys. E **9** (11), 921.
- Ibaraki, Y., U. Tanaka, and S. Urabe (2011), Appl. Phys. B **105** (2), 219.
- Jadraque, M., M. Santos, L. Díaz, J. Álvarez-Ruiz, and M. Martín (2009), J. Phys. Chem. A **113** (41), 10880.
- Kaplan, A. E. (2009), Opt. Express. **17** (12), 10035.
- Knünz, S., M. Herrmann, V. Batteiger, G. Saathoff, T. Hänsch, K. Vahala, and T. Udem (2010), Phys. Rev. Lett. **105** (1), 013004.
- Kokish, M., M. Dietrich, and B. Odom (2016), J. Phys. B **49** (3), 035301.
- Lagerqvist, A., and I. Renhorn (1974), J. Mol. Spectrosc. **49** (1), 157.
- Latawiec, A., and G. Lockwood (1966), “Method of electropolishing tungsten wire,” US Patent 3,287,238.
- Lee, G.-H., S. Xiao, and A. M. Weiner (2006), IEEE Photonic Tech. L. **18** (17), 1819.
- Leibfried, D. (2012), New J. Phys. **14** (2), 023029.
- Leibfried, D., R. Blatt, C. Monroe, and D. Wineland (2003), Rev. Mod. Phys. **75** (1), 281.
- Lien, C.-Y., C. M. Seck, Y.-W. Lin, J. H. V. Nguyen, D. A. Tabor, and B. C. Odom (2014), Nat. Commun. **5**.

- Lien, C.-Y., S. R. Williams, and B. Odom (2011), *J. Chem. Phys.* **13** (42), 18825.
- Lin, Y.-W., S. Williams, and B. Odom (2013), *Phys. Rev. A* **87** (1), 011402.
- Lindberg, M., and J. Javanainen (1986), *JOSA B* **3** (7), 1008.
- Macalpine, W., and R. Schildknecht (1959), *Proceedings of the IRE* **47** (12), 2099.
- Marzoli, I., J. Cirac, R. Blatt, and P. Zoller (1994), *Phys. Rev. A* **49** (4), 2771.
- Matsuo, Y., T. Nakajima, T. Kobayashi, and M. Takami (1997), *Appl. Phys. Lett.* **71**, 996.
- Mogi, T., Y. Fukuyama, T. Kobayashi, I. Tanihata, K. Uehara, and Y. Matsuo (2002), *Appl. Surf. Sci.* **197**, 202.
- Monmayrant, A., and B. Chatel (2004), *Rev. Sci. Instrum.* **75**, 2668.
- Monmayrant, A., S. Weber, and B. Chatel (2010), *J. Phys. B* **43** (10), 103001.
- Müller, B., and C. Ottinger (1986), *J. Chem. Phys.* **85** (1), 232.
- Mur-Petit, J., J. J. García-Ripoll, J. Pérez-Ríos, J. Campos-Martínez, M. I. Hernández, and S. Willitsch (2012), *Phys. Rev. A* **85** (2), 022308.
- Nakamura, K. G., I. Kamioka, and M. Kitajima (1996), *J. Chem. Phys.* **104** (9), 3403.
- Nakamura, K. G., and M. Kitajima (1994), *Appl. Phys. Lett.* **65** (19), 2445.
- Nakamura, K. G., and M. Kitajima (1995), *J. Chem. Phys.* **102** (21), 8569.
- Nguyen, J., and B. Odom (2011), *Phys. Rev. A* **83** (5), 053404.
- Nguyen, J. H., C. R. Viteri, E. G. Hohenstein, C. D. Sherrill, K. R. Brown, and B. Odom (2011), *New J. Phys.* **13** (6), 063023.
- Oddershede, J., and N. Elander (1976), *J. Chem. Phys.* **65** (9), 3495.
- Ott, G., J. Wrba, and R. Lucke (2003), *J. Magn. Magn. Mater.* **254**, 535.
- Pankhurst, R. (1940), *P. Phys. Soc.* **52** (5), 707.
- Pastirk, I., B. Resan, A. Fry, J. MacKay, and M. Dantus (2006), *Opt. Express.* **14** (20), 9537.

- Paye, J., and A. Migus (1995), *JOSA B* **12** (8), 1480.
- Pearson, B. J., and T. C. Weinacht (2007), *Opt. Express*. **15** (7), 4385.
- Rondi, A., J. Extermann, L. Bonacina, S. Weber, and J.-P. Wolf (2009), *Appl. Phys. B* **96** (4), 757.
- Rosenband, T., D. Hume, P. Schmidt, C. Chou, A. Brusch, L. Lorini, W. Oskay, R. Drullinger, T. Fortier, J. Stalnaker, *et al.* (2008), *Science* **319** (5871), 1808.
- Rosner, S., R. Cameron, T. Scholl, and R. Holt (1998), *J. Mol. Spectrosc.* **189** (1), 83.
- Roth, M., M. Mehendale, A. Bartelt, and H. Rabitz (2005), *Appl. Phys. B* **80** (4-5), 441.
- Sardesai, H., C.-C. Chang, and A. Weiner (1998), *Journal of Lightwave Technology* **16** (11), 1953.
- Sauer, F., A. Merli, L. Wöste, and A. Lindinger (2007), *J. Chem. Phys.* **334** (1), 138.
- Schmidt, P. O., T. Rosenband, J. C. J. Koelemeij, D. B. Hume, W. M. Itano, J. C. Bergquist, and D. J. Wineland (2006), *Non-Neutral Plasma Physics VI*, Aip Conference Proceedings, **862**, 305.
- Schmidt, P. O., T. Rosenband, C. Langer, W. M. Itano, J. C. Bergquist, and D. J. Wineland (2005), *Science* **309** (5735), 749.
- Scholl, T., R. Cameron, S. Rosner, and R. Holt (1995), *Phys. Rev. A* **51** (3), 2014.
- Schuessler, H. A., and O. Chun-Sing (1981), *Nucl. Instrum. Methods* **186** (1), 219.
- Schwartz, J. C., M. W. Senko, and J. E. Syka (2002), *J. Am. Soc. Mass. Spectr.* **13** (6), 659.
- Seck, C. M., E. G. Hohenstein, C.-Y. Lien, P. R. Stollenwerk, and B. C. Odom (2014), *J. Mol. Spectrosc.* **300**, 108.
- Seck, C. M., M. G. Kokish, M. R. Dietrich, and B. C. Odom (2016), *Phys. Rev. A* **93** (5), 053415.
- Shelkovich, A., R. J. Butcher, C. Chardonnet, and A. Amy-Klein (2008), *Phys. Rev. Lett.* **100** (15), 150801.
- Sheridan, K., and M. Keller (2011), *New J. Phys.* **13** (12), 123002.

- Sheridan, K., N. Seymour-Smith, A. Gardner, and M. Keller (2012), *Eur. Phys. J. D* **66** (11), 1.
- Shi, D., W. Li, W. Xing, J. Sun, Z. Zhu, and Y. Liu (2012), *Computational and Theoretical Chemistry* **980**, 73.
- Shu, G., N. Kurz, M. Dietrich, and B. Blinov (2010), *Phys. Rev. A* **81** (4), 042321.
- Siverns, J., L. Simkins, S. Weidt, and W. Hensinger (2012), *Appl. Phys. B* **107** (4), 921.
- Staanum, P. F., K. Højbjerg, P. S. Skyt, A. K. Hansen, and M. Drewsen (2010), *Nat. Phys.* **6** (4), 271.
- Steele, A., L. Churchill, P. Griffin, and M. Chapman (2007), *Phys. Rev. A* **75** (5), 053404.
- Stenholm, S. (1986), *Rev. Mod. Phys.* **58** (3), 699.
- Stobrawa, G., M. Hacker, T. Feurer, D. Zeidler, M. Motzkus, and F. Reichel (2001), *Appl. Phys. B* **72** (5), 627.
- Stollenwerk, P. R., B. C. Odom, D. L. Kokkin, and T. Steimle (2016), *J. Mol. Spectrosc.*
- Streed, E. W., B. G. Norton, A. Jechow, T. J. Weinhold, and D. Kielpinski (2011), *Phys. Rev. Lett.* **106** (1), 010502.
- Sturm, S., F. Köhler, J. Zatorski, A. Wagner, Z. Harman, G. Werth, W. Quint, C. H. Keitel, and K. Blaum (2014), *Nature* **506** (7489), 467.
- Supradeepa, V., C.-B. Huang, D. E. Leaird, and A. M. Weiner (2008), *Opt. Express* **16** (16), 11878.
- Tabor, D. (2014), *Toward Rotational Cooling of Trapped SiO^+ by Optical Pumping*, Ph.D. thesis (Northwestern University).
- Tabor, D., V. Rajagopal, Y.-W. Lin, and B. Odom (2012), *Appl. Phys. B* **107** (4), 1097.
- Tanigawa, T., Y. Sakakibara, S. Fang, T. Sekikawa, and M. Yamashita (2009), *Opt. Lett.* **34** (11), 1696.
- Thurston, R., J. Heritage, A. Weiner, and W. Tomlinson (1986), *IEEE J. Quantum Elect.* **22** (5), 682.

- Torres, R., M. Jdraque, and M. Martin (2005), *Appl. Phys. A* **80** (8), 1671.
- Ubachs, W., J. Bagdonaite, E. J. Salumbides, M. T. Murphy, and L. Kaper (2016), *Rev. Mod. Phys.* **88**, 021003.
- Uzan, J.-P. (2011), *Living Rev. Relativity* **14** (2).
- Vahala, K., M. Herrmann, S. Knuenz, V. Batteiger, G. Saathoff, T. W. Haensch, and T. Udem (2009), *Nat. Phys.* **5** (9), 682.
- Vanhaecke, N., and O. Dulieu (2007), *Mol. Phys.* **105** (11-12), 1723.
- Villemoes, P., A. Arnesen, F. Heijkenskjold, and A. Wannstrom (1993), *J. Phys. B* **26** (22), 4289.
- Viteau, M., A. Chotia, M. Allegrini, N. Bouloufa, O. Dulieu, D. Comparat, and P. Pillet (2008), *Science* **321** (5886), 232.
- Vizmuller, P. (1995), *RF design guide: systems, circuits, and equations*, Vol. 1 (Artech House).
- Voitsekhovich, V. S., M. V. Danileiko, A. M. Negriiko, V. I. Romanenko, and L. P. Yatsenko (1989), *JETP Lett.* **49** (3), 161.
- Wang, B., J. Zhang, C. Gao, and L. Wang (2011), *Opt. Express.* **19** (17), 16438.
- Watson, J. K. (2008), *J. Mol. Spectrosc.* **252** (1), 5.
- Weber, S., M. Barthelemy, and B. Chatel (2010), *Appl. Phys. B* **98** (2-3), 323.
- Wefers, M. M., and K. A. Nelson (1996), *IEEE J. Quantum Elect.* **32** (1), 161.
- Weiner, A. M. (2011), *Opt. Commun.* **284** (15), 3669, special Issue on Optical Pulse Shaping, Arbitrary Waveform Generation, and Pulse Characterization.
- Welling, M., H. Schuessler, R. Thompson, and H. Walther (1998), *Int. J. Mass. Spectrom.* **172** (1), 95.
- Wendt, K., S. Ahmad, F. Buchinger, A. Mueller, R. Neugart, and E.-W. Otten (1984), *Zeitschrift für Physik A Atoms and Nuclei* **318** (2), 125.
- Wineland, D., W. M. Itano, J. Bergquist, and R. G. Hulet (1987), *Phys. Rev. A* **36** (5), 2220.

Wineland, D. J., and W. M. Itano (1979), Phys. Rev. A **20** (4), 1521.

Wineland, D. J., C. Monroe, W. M. Itano, D. Leibfried, B. E. King, and D. M. Meekhof (1997), arXiv preprint quant-ph/9710025 .

Woods, L. (1943), Phys. Rev. **63** (11-12), 426.

Zhang, C. B., D. Offenberg, B. Roth, M. Wilson, and S. Schiller (2007), Phys. Rev. A **76** (1), 012719.

Zhang, J.-y., J. Y. Huang, H. Wang, K. Wong, and G. Wong (1998), JOSA B **15** (1), 200.

Zverev, A. I. (1967), *Handbook of filter synthesis* (Wiley-Blackwell).

addtocontentslof

APPENDIX A

Fluorescence from a Three-level System

Here I consider the population cycling in a three-level system: a is the excitation, b and c are the two ground states. The $a \rightarrow c$ decay is assumed to be weaker than $a \rightarrow b$; therefore $a \rightarrow b$ is the fluorescing transition and $a \rightarrow c$ is the repumping transition. The Optical Bloch equation of the system is:

$$\rho'_{ab} = -\left(\frac{\Gamma_b + \Gamma_c}{2} - i\Delta_b\right)\rho_{ab} + i\frac{\Omega_b}{2}(\rho_a - \rho_b) - i\frac{\Omega_c}{2}\rho_{cb} \quad (\text{A.1a})$$

$$\rho'_{ba} = -\left(\frac{\Gamma_b + \Gamma_c}{2} + i\Delta_b\right)\rho_{ba} - i\frac{\Omega_b}{2}(\rho_a - \rho_b) + i\frac{\Omega_c}{2}\rho_{bc} \quad (\text{A.1b})$$

$$\rho'_{ac} = -\left(\frac{\Gamma_b + \Gamma_c}{2} - i\Delta_c\right)\rho_{ac} + i\frac{\Omega_c}{2}(\rho_a - \rho_c) - i\frac{\Omega_b}{2}\rho_{bc} \quad (\text{A.1c})$$

$$\rho'_{ca} = -\left(\frac{\Gamma_b + \Gamma_c}{2} + i\Delta_c\right)\rho_{ca} - i\frac{\Omega_c}{2}(\rho_a - \rho_c) + i\frac{\Omega_b}{2}\rho_{cb} \quad (\text{A.1d})$$

$$\rho'_{cb} = -i(\Delta_c - \Delta_b)\rho_{cb} + i\frac{\Omega_b}{2}\rho_{ca} - i\frac{\Omega_c}{2}\rho_{ab} \quad (\text{A.1e})$$

$$\rho'_{bc} = -i(\Delta_b - \Delta_c)\rho_{bc} - i\frac{\Omega_b}{2}\rho_{ac} + i\frac{\Omega_c}{2}\rho_{ba} \quad (\text{A.1f})$$

$$\rho'_b = -i\frac{\Omega_b}{2}(\rho_{ab} - \rho_{ba}) + \Gamma_b\rho_a \quad (\text{A.1g})$$

$$\rho'_c = -i\frac{\Omega_c}{2}(\rho_{ac} - \rho_{ca}) + \Gamma_c\rho_a \quad (\text{A.1h})$$

$$\rho_a + \rho_b + \rho_c = 1. \quad (\text{A.1i})$$

In these equations, $\Gamma_{b,c}$, $\Omega_{b,c}$, and $\Delta_{b,c}$ are the spontaneous emission rates, Rabi frequencies, and the detunings for the $a \leftrightarrow b$ and $a \leftrightarrow c$ transitions, respectively. Because the two

light sources are incoherent, coherence between b and c vanishes. By taking $\rho_{bc} = \rho_{cb} = 0$, we obtain the following equations for steady state:

$$-\left(\frac{\Gamma_b + \Gamma_c}{2} - i\Delta_b\right)\rho_{ab} + i\frac{\Omega_b}{2}(\rho_a - \rho_b) = 0 \quad (\text{A.2a})$$

$$-\left(\frac{\Gamma_b + \Gamma_c}{2} + i\Delta_b\right)\rho_{ba} - i\frac{\Omega_b}{2}(\rho_a - \rho_b) = 0 \quad (\text{A.2b})$$

$$-\left(\frac{\Gamma_b + \Gamma_c}{2} - i\Delta_c\right)\rho_{ac} + i\frac{\Omega_c}{2}(\rho_a - \rho_c) = 0 \quad (\text{A.2c})$$

$$-\left(\frac{\Gamma_b + \Gamma_c}{2} + i\Delta_c\right)\rho_{ca} - i\frac{\Omega_c}{2}(\rho_a - \rho_c) = 0 \quad (\text{A.2d})$$

$$-i\frac{\Omega_b}{2}(\rho_{ab} - \rho_{ba}) + \Gamma_b\rho_a = 0 \quad (\text{A.2e})$$

$$-i\frac{\Omega_c}{2}(\rho_{ac} - \rho_{ca}) + \Gamma_c\rho_a = 0 \quad (\text{A.2f})$$

$$\rho_a + \rho_b + \rho_c = 1. \quad (\text{A.2g})$$

To simplify the expression, introduce

$$F_{b,c} = \frac{(\Omega_{b,c}/\Gamma)^2}{(\Gamma_{b,c}/\Gamma)[1 + (2\Delta_{b,c}/\Gamma)^2] + (\Omega_{b,c}/\Gamma)^2} \quad (\text{A.3})$$

where $\Gamma = \Gamma_b + \Gamma_c$ is the total spontaneous emission rate. Note that the value of $F_{b,c}$ takes place between 0 and 1. The solution of the population terms is

$$\rho_a = F_b F_c / (F_b F_c + F_c + F_b) \quad (\text{A.4a})$$

$$\rho_b = F_c / (F_b F_c + F_c + F_b) \quad (\text{A.4b})$$

$$\rho_c = F_b / (F_b F_c + F_c + F_b) \quad (\text{A.4c})$$

and the solution of the coherence terms is

$$\rho_{ab} = \frac{-i(1 + 2i\Delta_b/\Gamma)(\Omega_b/\Gamma)}{(\Gamma_b/\Gamma)[1 + (2\Delta_b/\Gamma)^2] + (\Omega_b/\Gamma)^2} \times \rho_b \quad (\text{A.4d})$$

$$\rho_{ac} = \frac{-i(1 + 2i\Delta_c/\Gamma)(\Omega_c/\Gamma)}{(\Gamma_c/\Gamma)[1 + (2\Delta_c/\Gamma)^2] + (\Omega_c/\Gamma)^2} \times \rho_c. \quad (\text{A.4e})$$

The fluorescence rate is proportional to the excitation state population ρ_a . It is easy to see that ρ_a is monotonic in both F_b and F_c once we rearrange Eq. A.4b as

$$\rho_a = \frac{F_b F_c}{F_b + F_c + F_b F_c} = \frac{1}{1 + 1/F_b + 1/F_c}. \quad (\text{A.5})$$

The maximum value of ρ_a is $1/3$ when $F_b = F_c = 1$. Fig. A.1 upper plot shows F_c as a function of Ω_c/Γ_c for various Γ_c/Γ_b . The lower plot shows the dependence between the excitation state population ρ_a and the repumping intensity. For a weaker transition, we will need much stronger intensity to provide sufficient repumping.

Einstein's Rate Equation

It is interesting to study the rate equation formulation to model the population dynamics in the same three-level system as well:

$$\rho'_a = -(\Gamma_b + \Gamma_c)\rho_a + u_b B_b \rho_b - u_b B_b \rho_a + u_c B_c \rho_c - u_c B_c \rho_a \quad (\text{A.6a})$$

$$\rho'_b = \Gamma_b \rho_a - u_b B_b \rho_b + u_b B_b \rho_a \quad (\text{A.6b})$$

$$\rho'_c = \Gamma_c \rho_a - u_c B_c \rho_c + u_c B_c \rho_a \quad (\text{A.6c})$$

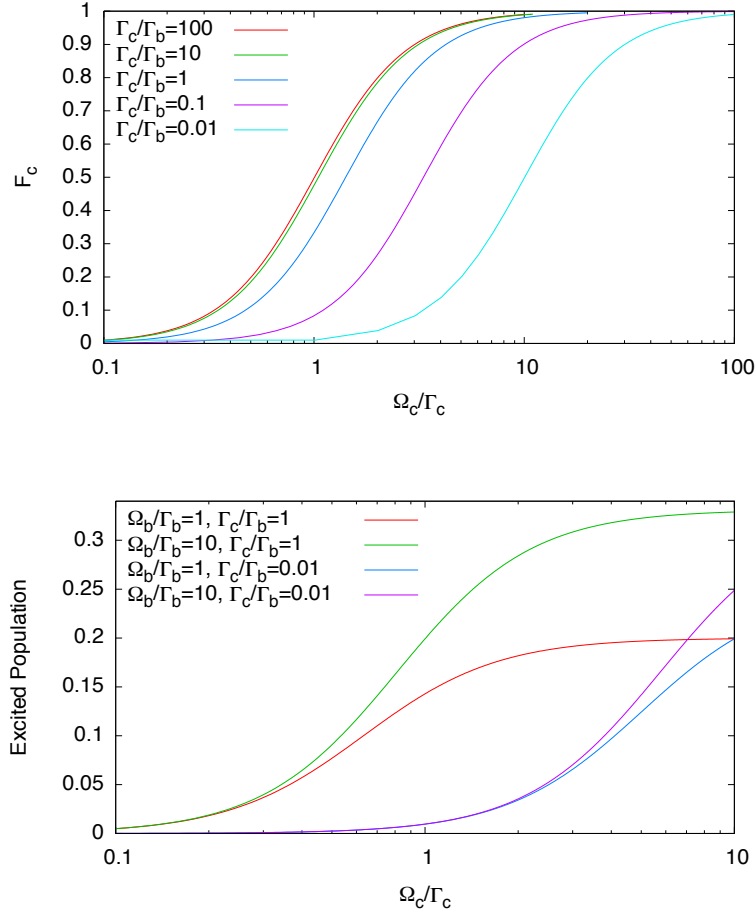


Figure A.1. (Upper plot) F_c versus laser intensity Ω_c/Γ_c . (Lower plot) Excitation state population versus laser intensity Ω_c/Γ_c . $\Delta_b = 0$ and $\Delta_c = 0$ in both plots.

where $B_{b,c}$ are the Einstein B coefficients and $u_{b,c}$ are the excitation energy spectra density.

The steady state, i.e. $\rho'_a = \rho'_b = \rho'_c = 0$, is

$$\rho_a = X_b X_c / (X_b + X_c + 3X_b X_c) \quad (\text{A.7a})$$

$$\rho_b = (X_c + X_b X_c) / (X_b + X_c + 3X_b X_c) \quad (\text{A.7b})$$

$$\rho_c = (X_b + X_b X_c) / (X_b + X_c + 3X_b X_c) \quad (\text{A.7c})$$

with $X_{b,c} = u_{b,c}B_{b,c}/\Gamma_{b,c}$. To relate the Einstein rate equation to Optical Bloch equation, we compare Eq. A.1g and A.1h to Eq. A.6b and A.6c. The A coefficients are just the spontaneous emission rate: $A_{b,c} = \Gamma_{b,c}$. The stimulated absorption/emission terms between state a and b (or c) in the Optical Bloch equations can be written as

$$-\frac{i\Omega_{b,c}}{2}(\rho_{a\{b,c\}} - \rho_{\{b,c\}a}) = \frac{1}{1 + (2\Delta_{b,c}/\Gamma)^2} \frac{\Omega_{b,c}^2}{\Gamma}(\rho_a - \rho_{b,c}). \quad (\text{A.8})$$

Compare to the corresponding terms in the rate equation we find the expression for stimulated transition rate with monochromatic drive to be

$$u_{b,c}B_{b,c} = \frac{1}{1 + (2\Delta_{b,c}/\Gamma)^2} \frac{\Omega_{b,c}^2}{\Gamma}. \quad (\text{A.9})$$

Furthermore, we find

$$F_{b,c} = \frac{X_{b,c}}{1 + X_{b,c}} \quad (\text{A.10})$$

and Eq. A.7a becomes

$$\begin{aligned} \rho_a &= \frac{X_b X_c}{X_b + X_c + 3X_b X_c} \\ &= \frac{1}{1/X_b + 1/X_c + 3} \\ &= \frac{1}{1 + 1/F_b + 1/F_c}, \end{aligned} \quad (\text{A.11})$$

which is identical to Eq. A.5.

How About the Broadband Source?

The expression in Eq. A.9 is for a monochromatic light source. The result can be rewritten as a function of laser intensity:

$$u_c B_c = \frac{1}{1 + (2\Delta_c/\Gamma)^2} \frac{\Gamma_c^2}{\Gamma} \frac{I}{2I_s} \quad (\text{A.12})$$

where $I_s = \pi hc\Gamma_c/3\lambda^3$ is the saturation intensity. We describe a broadband source with a normalized spectra function $g(\omega)$:

$$I(\Delta) \rightarrow \frac{P}{A} g(\Delta) d\Delta$$

where P is the total power and A is the beam size. The stimulated transition rate is then generalized as

$$u_c B_c = \int \frac{1}{1 + (2\Delta_c/\Gamma)^2} \frac{\Gamma_c^2}{\Gamma} \frac{P/A}{2I_s} g(\Delta_c) d\Delta_c. \quad (\text{A.13})$$

As an example, we consider a source with constant spectra density $g(\Delta) = 1/w$ over a bandwidth w . We then have

$$u_c B_c = \frac{\Gamma_c^2}{\Gamma} \frac{P/Aw}{2I_s} \int_{-w/2}^{w/2} \frac{d\Delta_c}{1 + (2\Delta_c/\Gamma)^2} = \frac{\Gamma_c^2 P}{2AI_s} \frac{\tan^{-1}(w/\Gamma)}{w}. \quad (\text{A.14})$$

The case of $w \rightarrow 0$ gives the result for a resonant monochromatic source. When $w \gg \Gamma$ the rate becomes

$$u_c B_c = \frac{\Gamma_c}{2I_s} \frac{\pi P \Gamma_c}{2Aw} = \Gamma_c \frac{3P\lambda^3}{4hcAw}. \quad (\text{A.15})$$

APPENDIX B

Finite Element Analysis of the Trap Potential

The appendix provides the technical supplementary to Section 2.2 by listing the simulation scripts.

Set up the Mesh

First, the geometry of the trap is scripted in a ".geo" file. Then Gmsh discretizes the geometry and creates a ".msh" mesh file by the following command.

```
gmsh -3 <input.geo> -o <output.msh>
```

FreeFem++

To solve the differential equation by FreeFem++, another script ".edp" files is created with information of the equation, boundaries, and solver options. A sample script is attached below.

```
1 // Load necessary packages
  load "gmsh"
  load "medit"
  load "MUMPS"
5
  // Load mesh file
  mesh3 Th = gmshload3 ("trap_single.msh");

  // Create the finite element space
10 fespace Vh(Th, P13d);
   Vh uh=x+y+z, vh;
```

```

// Define gradient
macro Grad(u) [dx(u),dy(u),dz(u)] //
15 // Allocate an array for boundary values
real[int] bc(4);

// Set up the Laplace equation as well as the boundary
  ↪ conditions
problem Lap(uh, vh) = int3d(Th)(Grad(uh)'*Grad(vh))
20   + on(800, uh=bc[0]) // container
   + on(801, uh=bc[1])   + on(802, uh=bc[2]) // rf
   ↪ rods
   + on(803, uh=bc[3]); // end caps

// Solve the problem and save the answer to a file
25 cout << "1: 801" << endl;
// One of the boundaries value is set to 1
bc = 0;
bc[1] = 1;
// Solve
30 Lap;
// Output to file
{
    ofstream ff("ans_ 801.txt");
    for (int i=0; i<Vh.ndof; i++) {
35         ff << Th(i).x << " " << Th(i).y << " " << Th
           ↪ (i).z << " " << uh[][i] << endl;
    }
}

```

To solve the problem, execute the following command.

```
FreeFem++ <script.edp>
```

Note that both Gmsh and FreeFem++ have a GUI interface and the job can certainly be done by using the GUI. However, be careful that the computer efficiency may quite reduced as visualization of the complex geometry would use lots of resource. Therefore, using GUI is not recommended.

Post-processing

A sample python script for the multipole expansion fitting is attached below.

```

1 import numpy as np
  import scipy.special

  import matplotlib
5 import matplotlib.mlab as mlab
  import matplotlib.cm as cm
  import matplotlib.pyplot as plt

  def yLegSphHarm(l, m):
10     q = np.power(r2, l/2)*scipy.special.lpmv(m, l, ct)
      if m==0:
          return q
      elif m>0:
          return q*np.cos(m*phi)
15     else :
          return q*np.sin(m*phi)

  def makeAMatrix(lmax):
20     A = np.ones(len(x))
      for l in range(2, lmax+1, 2):
          A = np.c_[A, yLegSphHarm(l, 0)]
          for m in range(2, l+1, 2):
              A = np.c_[A, yLegSphHarm(l, m),
25                 ↪ yLegSphHarm(l, -m)]
      return A

  data = np.loadtxt('ans_single_801.txt')
  x = data[:, 0]
30 y = data[:, 1]
  z = data[:, 2]
  v = data[:, 3]

  pIdx = np.flatnonzero(((x*x+y*y) < 0.2**2) & (abs(z) < 0.8))
35 x = x[pIdx]

```

```

y = y[pIdx]
z = z[pIdx]
v = v[pIdx]
40

r2 = x*x+y*y+z*z
r = np.sqrt(r2)
ct = [z1/r1 if r1>0 else 0.0 for z1,r1 in zip(z,r)]
45 phi = np.arctan2(y, x)

A = makeAMatrix(8)
(U, w, V) = np.linalg.svd(A, full_matrices=False)

50 b = np.dot((np.dot(U.T, v)/w), V)
s = np.sqrt(np.dot(V.T**2,1/w**2))

b1 = ['%.2e' % ele for ele in b]

55 # print(np.linalg.norm(A.dot(b)-v))

def legSphHarm(l, m, x, y, z):
    r2 = x*x+y*y+z*z
    60 ct = z/np.sqrt(r2) if r2!=0 else 0.0
    q = np.power(r2, l/2)*scipy.special.lpmv(m, l, ct)
    if m==0:
        return q
    elif m>0:
    65 return q*np.cos(m*np.arctan2(y, x))
    else :
        return q*np.sin(m*np.arctan2(y, x))

def comp(lMax, x, y, z):
    70 p = np.array([1])
    for l in range(2,lMax+1,2):
        p = np.append(p, legSphHarm(l, 0, x, y, z))
        for m in range(2,l+1,2):
            p = np.append(p, [legSphHarm(l, m, x
                ↪ , y, z), legSphHarm(l, -m, x,
                ↪ y, z)])
    75 return p

```

```
# np.dot(b, comp()) gives the fitting result
```

B.1. Single Ion Trap

Trap Geometry

```
1 Mesh.VolumeEdges = 0;

Macro yCircle
    p0 = newp; Point(p0) = {x0, y0, z0};
5    p1 = newp; Point(p1) = {x0+r, y0, z0};
    p2 = newp; Point(p2) = {x0, y0+r, z0};
    p3 = newp; Point(p3) = {x0-r, y0, z0};
    p4 = newp; Point(p4) = {x0, y0-r, z0};
    Characteristic Length {p1, p2, p3, p4} = lc;
10    c1 = newreg; Circle(c1) = {p1, p0, p2};
    c2 = newreg; Circle(c2) = {p2, p0, p3};
    c3 = newreg; Circle(c3) = {p3, p0, p4};
    c4 = newreg; Circle(c4) = {p4, p0, p1};
    l1 = newreg; Line Loop(l1) = {c1, c2, c3, c4};
15 Return

Macro Cylinder
    Call yCircle;
    s1 = newreg; Plane Surface(s1) = {l1};
20    out[] = Extrude {0, 0, L} { Surface{s1}; };
    Delete { Volume{out[1]}; }
    out[1] = out[0]; out[0] = s1;

Return

25 // parameters
    inch = 25.4;

// Container
30 x0 = 0; y0 = 0; z0 = -2.2;
    r = 2; L = 4.4; lc = 0.2;
    Call Cylinder;
```

```

container [] = out [];

35 //RF rods
r = 0.027/2*inch; L = 4; lc = r/10;
r0 = 0.8*0.7071;
// RF1, RF2
x0 = r0; y0 = r0; z0 = -L/2;
40 Call Cylinder;
rf1 [] = out [];
x0 = -r0; y0 = -r0; z0 = -L/2;
Call Cylinder;
rf2 [] = out [];
45 // RF3, RF4
x0 = -r0; y0 = r0; z0 = -L/2;
Call Cylinder;
rf3 [] = out [];
x0 = r0; y0 = -r0; z0 = -L/2;
50 Call Cylinder;
rf4 [] = out [];

// Endcaps
r = 0.018/2*inch;
55 L = 1; lc = r/10;
x0 = 0; y0 = 0; z0 = 1.9/2;
Call Cylinder;
ec1 [] = out [];
x0 = 0; y0 = 0; z0 = -1.9/2;
60 L = -1;
Call Cylinder;
ec2 [] = out [];

// Building everything
65 sh1 = newreg; Surface Loop(sh1) = container [];
sh2 = newreg; Surface Loop(sh2) = rf1 [];
sh3 = newreg; Surface Loop(sh3) = rf2 [];
sh4 = newreg; Surface Loop(sh4) = rf3 [];
sh5 = newreg; Surface Loop(sh5) = rf4 [];
70 sh6 = newreg; Surface Loop(sh6) = ec1 [];
sh7 = newreg; Surface Loop(sh7) = ec2 [];

Physical Surface(800) = container [];

```

```

75 Physical Surface(801) = {rf1 [], rf2 []};
Physical Surface(802) = {rf3 [], rf4 []};
Physical Surface(803) = {ec1 [], ec2 []};

Volume(900) = {sh1, sh2, sh3, sh4, sh5, sh6, sh7};
Physical Volume(900) = {900};

```

See Sections 2.2 and 3.1 for the result.

B.2. SiO⁺ trap

Trap Geometry

```

1 Mesh.VolumeEdges = 0;

Macro yCircle
5   p0 = newp; Point(p0) = {x0, y0, z0};
   p1 = newp; Point(p1) = {x0+r, y0, z0};
   p2 = newp; Point(p2) = {x0, y0+r, z0};
   p3 = newp; Point(p3) = {x0-r, y0, z0};
   p4 = newp; Point(p4) = {x0, y0-r, z0};
   Characteristic Length {p1, p2, p3, p4} = lc;
10  c1 = newreg; Circle(c1) = {p1, p0, p2};
   c2 = newreg; Circle(c2) = {p2, p0, p3};
   c3 = newreg; Circle(c3) = {p3, p0, p4};
   c4 = newreg; Circle(c4) = {p4, p0, p1};
   ll = newreg; Line Loop(ll) = {c1, c2, c3, c4};
15 Return

Macro Cylinder
   Call yCircle;
   s1 = newreg; Plane Surface(s1) = {ll};
20  out [] = Extrude {0, 0, L} { Surface{s1}; };
   Delete { Volume{out[1]}; }
   out[1] = out[0]; out[0] = s1;

Return

25 // ground can

```

```

x0 = 0; y0 = 0; z0 = -60;
r = 25; L = 120; lc = 2;
Call Cylinder;
30 container [] = out [];

// RF rods
r = 3.43; L = 101.6; lc = 0.5;
// RF1, RF2
35 x0 = 4.54; y0 = 4.54; z0 = -L/2;
Call Cylinder;
rf1 [] = out [];
x0 = -4.54; y0 = -4.54; z0 = -L/2;
Call Cylinder;
40 rf2 [] = out [];
// RF3, RF4
x0 = -4.54; y0 = 4.54; z0 = -L/2;
Call Cylinder;
rf3 [] = out [];
45 x0 = 4.54; y0 = -4.54; z0 = -L/2;
Call Cylinder;
rf4 [] = out [];

// End cap plate - 1
50 x0 = 0; y0 = 0; z0 = -14.6; lc = 2;
p1 = newp; Point(p1) = {11.4, 11.4, z0};
p2 = newp; Point(p2) = {-11.4, 11.4, z0};
p3 = newp; Point(p3) = {-11.4, -11.4, z0};
p4 = newp; Point(p4) = {11.4, -11.4, z0};
55 Characteristic Length {p1, p2, p3, p4} = lc;
l1 = newl; Line(l1) = {p1, p2};
l2 = newl; Line(l2) = {p2, p3};
l3 = newl; Line(l3) = {p3, p4};
l4 = newl; Line(l4) = {p4, p1};
60 l10 = newreg; Line Loop(l10) = {l1, l2, l3, l4};

r = 3.8; lc = 0.5;
x0 = 4.54; y0 = 4.54;
Call yCircle;
65 l11 = l1;
x0 = 4.54; y0 = -4.54;
Call yCircle;

```

```

112 = l1;
x0 = -4.54; y0 = -4.54;
70 Call yCircle;
l13 = l1;
x0 = -4.54; y0 = 4.54;
Call yCircle;
l14 = l1;
75 r = 1.27;
x0 = 0; y0 = 0;
Call yCircle;
l15 = l1;
s1 = newreg; Plane Surface(s1) = {l10 , l11 , l12 , l13 , l14 ,
  ↪ l15 };
80 out [] = Extrude {0, 0, -2.5} { Surface{s1}; };
Delete { Volume{out [1]}; }
out [1] = out [0]; out [0] = s1;
ec11 [] = out [];

85 // End cap tube - 1
x0 = 0; y0 = 0; z0 += 0.1; lc = 0.5;
r = 1.27;
Call yCircle;
l16 = l1;
90 r = 2.08;
Call yCircle;
l17 = l1;
s1 = newreg; Plane Surface(s1) = {l17 , l16 };
out [] = Extrude {0, 0, 4.4-0.1} { Surface{s1}; };
95 Delete { Volume{out [1]}; }
out [1] = out [0]; out [0] = s1;
ec12 [] = out [];

100 // End cap plate - 2
x0 = 0; y0 = 0; z0 = 14.6; lc = 2;
p1 = newp; Point(p1) = {11.4, 11.4, z0};
p2 = newp; Point(p2) = {-11.4, 11.4, z0};
p3 = newp; Point(p3) = {-11.4, -11.4, z0};
105 p4 = newp; Point(p4) = {11.4, -11.4, z0};
Characteristic Length {p1, p2, p3, p4} = lc;
l1 = newl; Line(l1) = {p1, p2};

```

```

110 | 12 = newl; Line(12) = {p2, p3};
    | 13 = newl; Line(13) = {p3, p4};
    | 14 = newl; Line(14) = {p4, p1};
    | 110 = newreg; Line Loop(110) = {11, 12, 13, 14};
    |
    | r = 3.8; lc = 0.5;
    | x0 = 4.54; y0 = 4.54;
115 | Call yCircle;
    | 111 = 11;
    | x0 = 4.54; y0 = -4.54;
    | Call yCircle;
    | 112 = 11;
120 | x0 = -4.54; y0 = -4.54;
    | Call yCircle;
    | 113 = 11;
    | x0 = -4.54; y0 = 4.54;
    | Call yCircle;
125 | 114 = 11;
    | r = 1.27;
    | x0 = 0; y0 = 0;
    | Call yCircle;
    | 115 = 11;
130 | s1 = newreg; Plane Surface(s1) = {110, 111, 112, 113, 114,
    | ↪ 115};
    | out[] = Extrude {0, 0, 2.5} { Surface{s1}; };
    | Delete { Volume{out[1]}; }
    | out[1] = out[0]; out[0] = s1;
    | ec21[] = out[];
135 | // End cap tube - 1
    | x0 = 0; y0 = 0; z0 -= 0.1; lc = 0.5;
    | r = 1.27;
    | Call yCircle;
140 | 116 = 11;
    | r = 2.08;
    | Call yCircle;
    | 117 = 11;
    | s1 = newreg; Plane Surface(s1) = {117, 116};
145 | out[] = Extrude {0, 0, -4.4+0.1} { Surface{s1}; };
    | Delete { Volume{out[1]}; }
    | out[1] = out[0]; out[0] = s1;

```

```
ec22 [] = out [];  
  
150 // build everything  
sh1 = newreg; Surface Loop(sh1) = container [];  
sh2 = newreg; Surface Loop(sh2) = rf1 [];  
sh3 = newreg; Surface Loop(sh3) = rf2 [];  
155 sh4 = newreg; Surface Loop(sh4) = rf3 [];  
sh5 = newreg; Surface Loop(sh5) = rf4 [];  
sh6 = newreg; Surface Loop(sh6) = ec11 [];  
sh7 = newreg; Surface Loop(sh7) = ec12 [];  
sh8 = newreg; Surface Loop(sh8) = ec21 [];  
160 sh9 = newreg; Surface Loop(sh9) = ec22 [];  
  
Physical Surface(800) = container [];  
Physical Surface(801) = {rf1 [], rf2 []};  
165 Physical Surface(802) = {rf3 [], rf4 []};  
Physical Surface(803) = {ec11 [], ec12 []};  
Physical Surface(804) = {ec21 [], ec22 []};  
  
170 Volume(900) = {sh1, sh2, sh3, sh4, sh5, sh6, sh7, sh8, sh9};  
Physical Volume(900) = {900};
```

Table B.1. Fitting region $\{(x, y, z) \mid \sqrt{x^2 + y^2} < 1.5, |z| < 5\}$

l	m	RF-1	RF-2	Endcap
0	0	4.92×10^{-1}	4.92×10^{-1}	1.59×10^{-2}
2	0	-2.00×10^{-3}	-2.18×10^{-3}	3.97×10^{-3}
2	2	-1.12×10^{-4}	7.65×10^{-5}	-3.28×10^{-5}
2	-2	-4.50×10^{-1}	4.50×10^{-1}	1.61×10^{-4}
4	0	-6.51×10^{-5}	-4.62×10^{-5}	1.47×10^{-4}
4	2	5.12×10^{-6}	-3.15×10^{-6}	1.34×10^{-6}
4	-2	-2.02×10^{-4}	2.89×10^{-4}	-1.32×10^{-4}
4	4	-1.13×10^{-6}	3.74×10^{-7}	4.19×10^{-7}
4	-4	-1.65×10^{-2}	4.56×10^{-2}	-5.96×10^{-3}
6	0	-2.49×10^{-6}	-3.25×10^{-6}	3.84×10^{-6}
6	2	-1.17×10^{-7}	5.61×10^{-8}	-2.45×10^{-8}
6	-2	-2.97×10^{-5}	2.89×10^{-5}	2.06×10^{-5}
6	4	3.17×10^{-9}	-7.82×10^{-10}	5.50×10^{-10}
6	-4	-1.03×10^{-2}	5.97×10^{-3}	2.04×10^{-3}
6	6	4.61×10^{-9}	-6.11×10^{-9}	1.39×10^{-9}
6	-6	-1.65	1.20	-8.79×10^{-2}
8	0	2.02×10^{-8}	3.35×10^{-8}	-2.38×10^{-8}
8	2	1.14×10^{-9}	-4.08×10^{-10}	1.74×10^{-10}
8	-2	2.91×10^{-6}	-3.04×10^{-6}	-1.03×10^{-6}
8	4	-9.61×10^{-12}	-1.84×10^{-11}	9.08×10^{-12}
8	-4	3.35×10^{-4}	-3.29×10^{-4}	-6.98×10^{-5}
8	6	-2.30×10^{-13}	7.19×10^{-13}	-3.11×10^{-12}
8	-6	3.78×10^{-1}	-2.70×10^{-1}	3.58×10^{-2}
8	8	1.09×10^{-11}	-6.40×10^{-12}	3.04×10^{-13}
8	-8	-1.75×10^2	3.37×10^2	3.25×10^1

B.3. AIH⁺ trap

Trap Geometry

```

1 Mesh.VolumeEdges = 0;

Macro yCircle
    p0 = newp; Point(p0) = {x0, y0, z0};
5    p1 = newp; Point(p1) = {x0+r, y0, z0};
    p2 = newp; Point(p2) = {x0, y0+r, z0};
    p3 = newp; Point(p3) = {x0-r, y0, z0};
    p4 = newp; Point(p4) = {x0, y0-r, z0};
    Characteristic Length {p1, p2, p3, p4} = lc;
10    c1 = newreg; Circle(c1) = {p1, p0, p2};
    c2 = newreg; Circle(c2) = {p2, p0, p3};
    c3 = newreg; Circle(c3) = {p3, p0, p4};
    c4 = newreg; Circle(c4) = {p4, p0, p1};
    ll = newreg; Line Loop(ll) = {c1, c2, c3, c4};
15 Return

Macro Cylinder
    Call yCircle;
    s1 = newreg; Plane Surface(s1) = {ll};
20    out [] = Extrude {0, 0, L} { Surface{s1}; };
    Delete { Volume{out [1]}; }
    out [1] = out [0]; out [0] = s1;

Return

25 // ground can
x0 = 0; y0 = 0; z0 = -40;
r = 20; L = 70; lc = 2;
Call Cylinder;
30 container [] = out [];

// RF rods
r = 3.43; L = -51.6; lc = 0.5; z0 = 17.1;
// RF1, RF2
35 x0 = 4.54; y0 = 4.54;
Call Cylinder;

```

```

rf1 [] = out [];
x0 = -4.54; y0 = -4.54;
Call Cylinder;
40 rf2 [] = out [];
// RF3, RF4
x0 = -4.54; y0 = 4.54;
Call Cylinder;
rf3 [] = out [];
45 x0 = 4.54; y0 = -4.54;
Call Cylinder;
rf4 [] = out [];

// End cap plate - 1
50 x0 = 0; y0 = 0; z0 = -14.6; lc = 1;
p1 = newp; Point(p1) = {11.4, 11.4, z0};
p2 = newp; Point(p2) = {-11.4, 11.4, z0};
p3 = newp; Point(p3) = {-11.4, -11.4, z0};
p4 = newp; Point(p4) = {11.4, -11.4, z0};
55 Characteristic Length {p1, p2, p3, p4} = lc;
l1 = newl; Line(l1) = {p1, p2};
l2 = newl; Line(l2) = {p2, p3};
l3 = newl; Line(l3) = {p3, p4};
l4 = newl; Line(l4) = {p4, p1};
60 ll0 = newreg; Line Loop(ll0) = {l1, l2, l3, l4};

r = 3.8; lc = 0.5;
x0 = 4.54; y0 = 4.54;
Call yCircle;
65 ll1 = ll;
x0 = 4.54; y0 = -4.54;
Call yCircle;
ll2 = ll;
x0 = -4.54; y0 = -4.54;
70 Call yCircle;
ll3 = ll;
x0 = -4.54; y0 = 4.54;
Call yCircle;
ll4 = ll;
75 r = 1.27;
x0 = 0; y0 = 0;
Call yCircle;

```

```

l15 = l1;
s1 = newreg; Plane Surface(s1) = {l10 , l11 , l12 , l13 , l14 ,
  ↪ l15 };
80 out [] = Extrude {0, 0, -2.5} { Surface{s1}; };
Delete { Volume{out [1]}; }
out [1] = out [0]; out [0] = s1;
ec1 [] = out [];

85 // End cap plate - 2
x0 = 0; y0 = 0; z0 = 14.6; lc = 1;
p1 = newp; Point(p1) = {11.4, 11.4, z0};
p2 = newp; Point(p2) = {-11.4, 11.4, z0};
p3 = newp; Point(p3) = {-11.4, -11.4, z0};
90 p4 = newp; Point(p4) = {11.4, -11.4, z0};
Characteristic Length {p1, p2, p3, p4} = lc;
l1 = newl; Line(l1) = {p1, p2};
l2 = newl; Line(l2) = {p2, p3};
l3 = newl; Line(l3) = {p3, p4};
95 l4 = newl; Line(l4) = {p4, p1};
l10 = newreg; Line Loop(l10) = {l1, l2, l3, l4};

r = 3.8; lc = 0.5;
x0 = 4.54; y0 = 4.54;
100 Call yCircle;
l11 = l1;
x0 = 4.54; y0 = -4.54;
Call yCircle;
l12 = l1;
105 x0 = -4.54; y0 = -4.54;
Call yCircle;
l13 = l1;
x0 = -4.54; y0 = 4.54;
Call yCircle;
110 l14 = l1;
r = 1.27;
x0 = 0; y0 = 0;
Call yCircle;
l15 = l1;
115 s1 = newreg; Plane Surface(s1) = {l10 , l11 , l12 , l13 , l14 ,
  ↪ l15 };
out [] = Extrude {0, 0, 2.5} { Surface{s1}; };

```

```
Delete { Volume{out[1]}; }
out[1] = out[0]; out[0] = s1;
ec2 [] = out [];
120

// build everything
sh1 = newreg; Surface Loop(sh1) = container [];
125 sh2 = newreg; Surface Loop(sh2) = rf1 [];
sh3 = newreg; Surface Loop(sh3) = rf2 [];
sh4 = newreg; Surface Loop(sh4) = rf3 [];
sh5 = newreg; Surface Loop(sh5) = rf4 [];
sh6 = newreg; Surface Loop(sh6) = ec1 [];
130 sh7 = newreg; Surface Loop(sh7) = ec2 [];

Physical Surface(800) = container [];
Physical Surface(801) = {rf1 [], rf2 []};
135 Physical Surface(802) = {rf3 [], rf4 []};
Physical Surface(803) = {ec1 [], ec2 []};

Volume(900) = {sh1, sh2, sh3, sh4, sh5, sh6, sh7};
Physical Volume(900) = {900};
```

Table B.2. Fitting region $\{(x, y, z) \mid \sqrt{x^2 + y^2} < 1.6, |z| < 9\}$

l	m	RF-1	RF-2	Endcap
0	0	5.00×10^{-1}	5.00×10^{-1}	1.54×10^{-4}
2	0	-5.82×10^{-5}	2.93×10^{-5}	2.97×10^{-5}
2	2	4.40×10^{-5}	-4.43×10^{-5}	2.21×10^{-7}
2	-2	-4.48×10^{-1}	4.48×10^{-1}	-1.69×10^{-6}
4	0	6.93×10^{-6}	-8.29×10^{-6}	1.33×10^{-6}
4	2	1.85×10^{-7}	-1.70×10^{-7}	-1.11×10^{-8}
4	-2	-1.54×10^{-4}	1.53×10^{-4}	2.58×10^{-6}
4	4	-5.44×10^{-7}	5.11×10^{-7}	2.10×10^{-9}
4	-4	-2.72×10^{-2}	2.72×10^{-2}	2.57×10^{-6}
6	0	-3.40×10^{-7}	3.29×10^{-7}	1.16×10^{-8}
6	2	-1.36×10^{-8}	1.34×10^{-8}	2.26×10^{-10}
6	-2	-4.62×10^{-6}	4.86×10^{-6}	-2.98×10^{-7}
6	4	-2.25×10^{-9}	2.19×10^{-9}	5.63×10^{-11}
6	-4	-6.69×10^{-3}	6.68×10^{-3}	2.38×10^{-5}
6	6	4.16×10^{-9}	-4.16×10^{-9}	-1.33×10^{-11}
6	-6	-1.63×10^{-1}	1.61×10^{-1}	3.95×10^{-3}
8	0	4.97×10^{-9}	-5.36×10^{-9}	3.69×10^{-10}
8	2	1.55×10^{-10}	-1.53×10^{-10}	-1.69×10^{-12}
8	-2	-8.91×10^{-8}	8.25×10^{-8}	7.75×10^{-9}
8	4	7.13×10^{-12}	-7.03×10^{-12}	-8.35×10^{-14}
8	-4	2.34×10^{-4}	-2.34×10^{-4}	-7.21×10^{-7}
8	6	-6.30×10^{-13}	5.77×10^{-13}	5.44×10^{-14}
8	-6	4.01×10^{-2}	-3.86×10^{-2}	-1.70×10^{-3}
8	8	-3.88×10^{-12}	3.80×10^{-12}	6.86×10^{-14}
8	-8	-5.65×10^1	5.67×10^1	-5.84×10^{-2}

APPENDIX C

Drawings

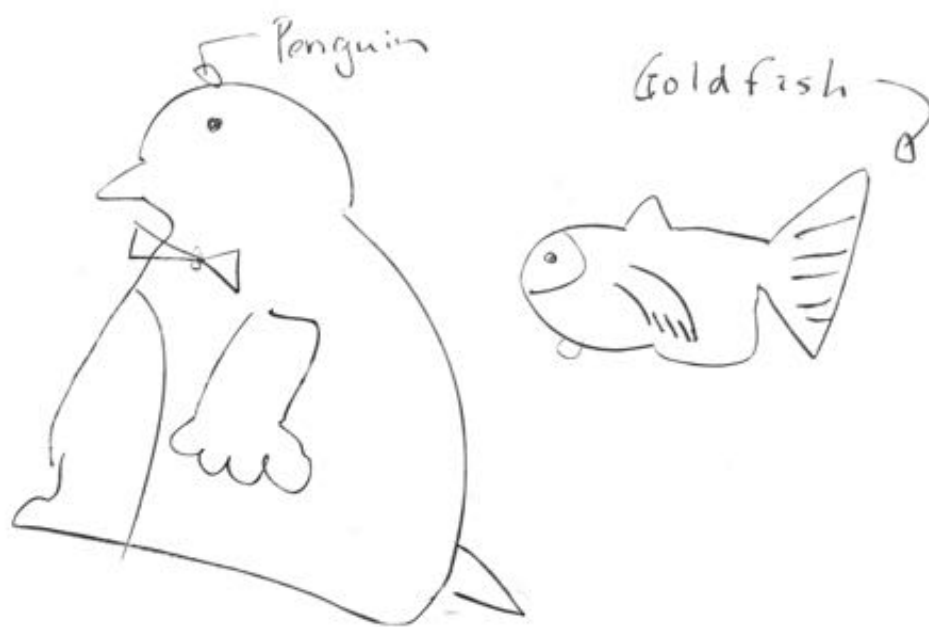


Figure C.1. Macro stand for RF electrodes - sheet 1

Units: inches/degree. Tolerance: ± 0.005 ". Material: Macro

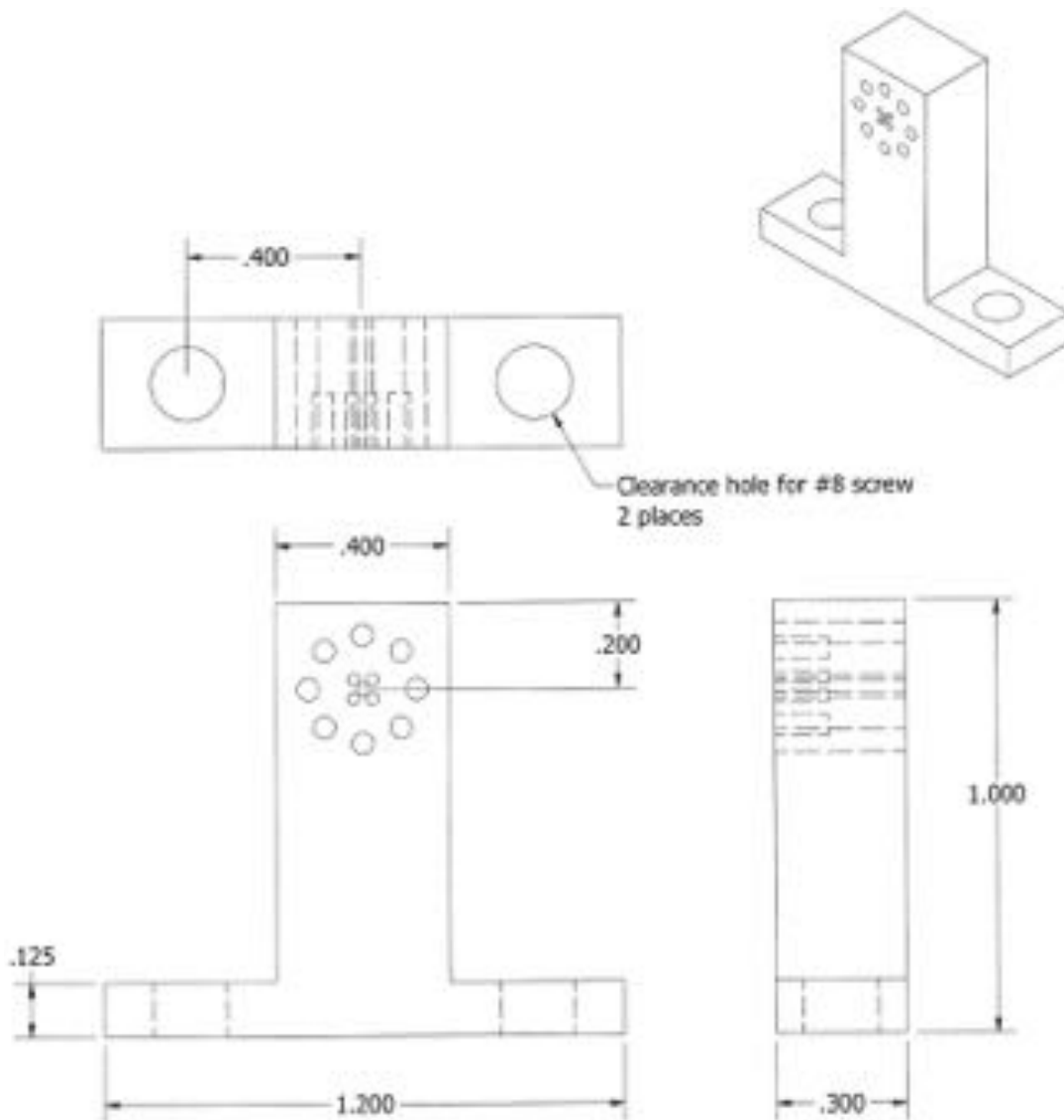


Figure C.2. Macro stand - sheet 2

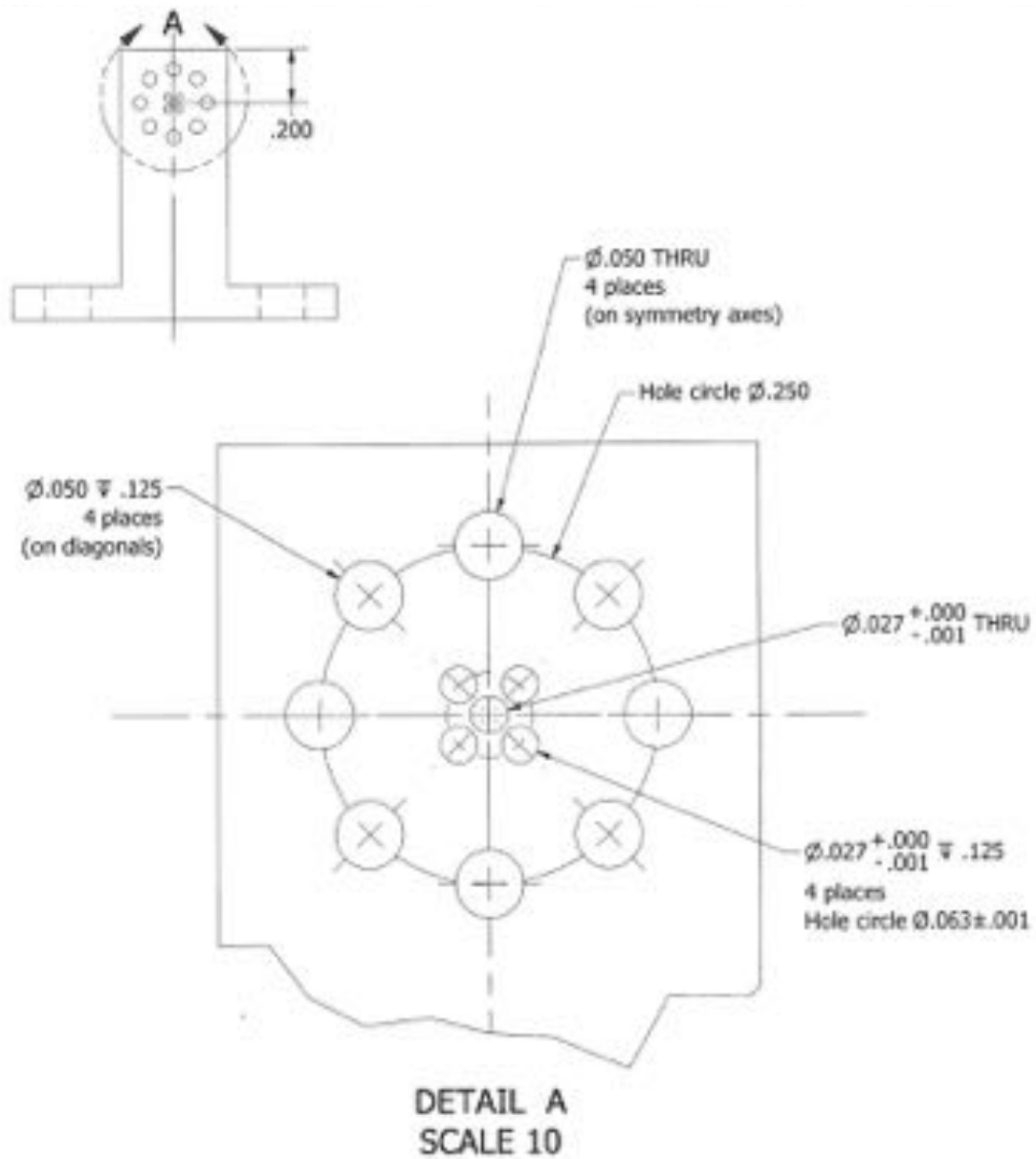


Figure C.3. Macro stand for endcap electrodes

Units: inches/degree. Tolerance: $\pm 0.005''$. Material: Macro

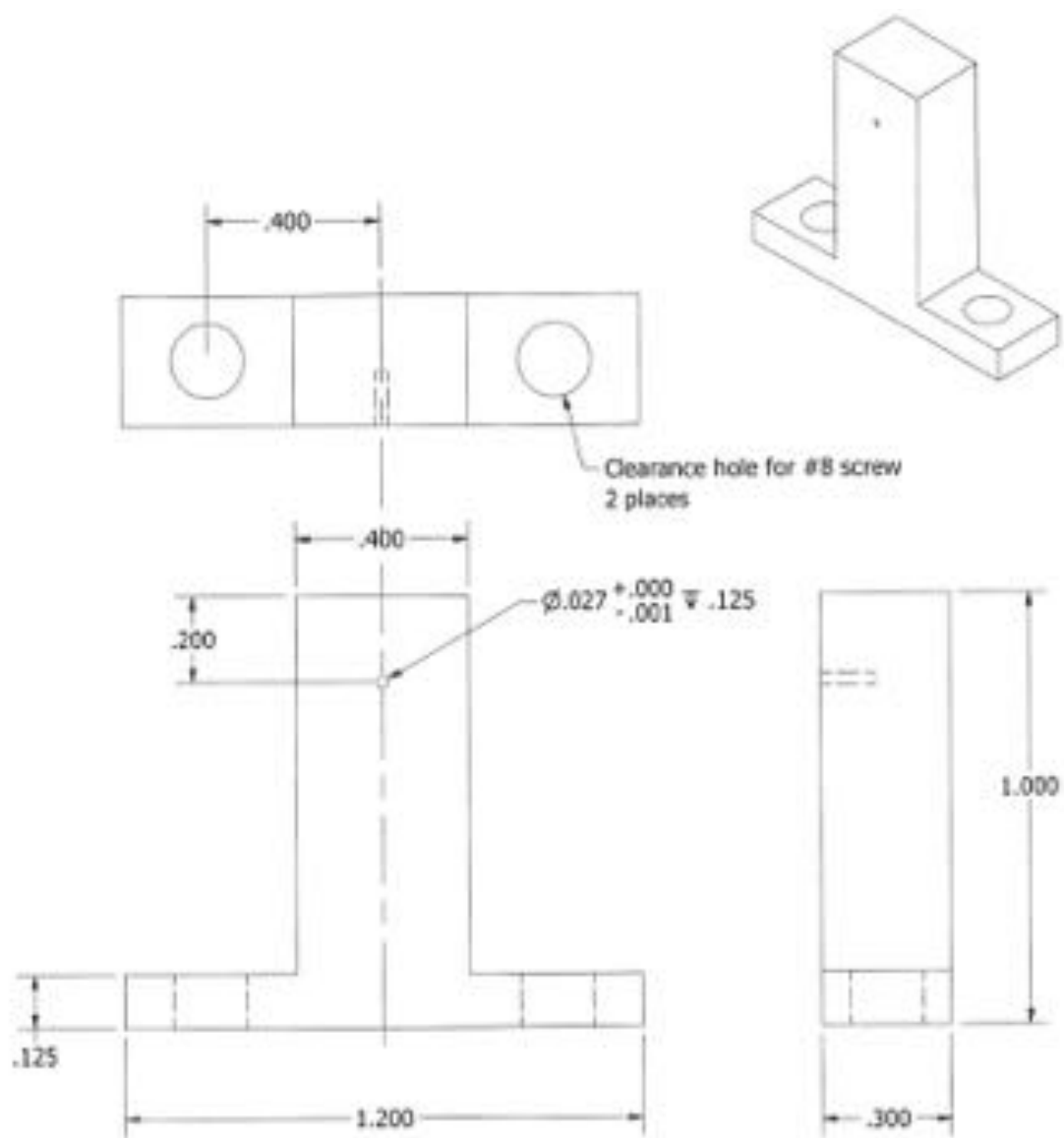


Figure C.4. Trap base plate

Units: inches/degree. Tolerance: $\pm 0.01''$. Material: stainless steel 316

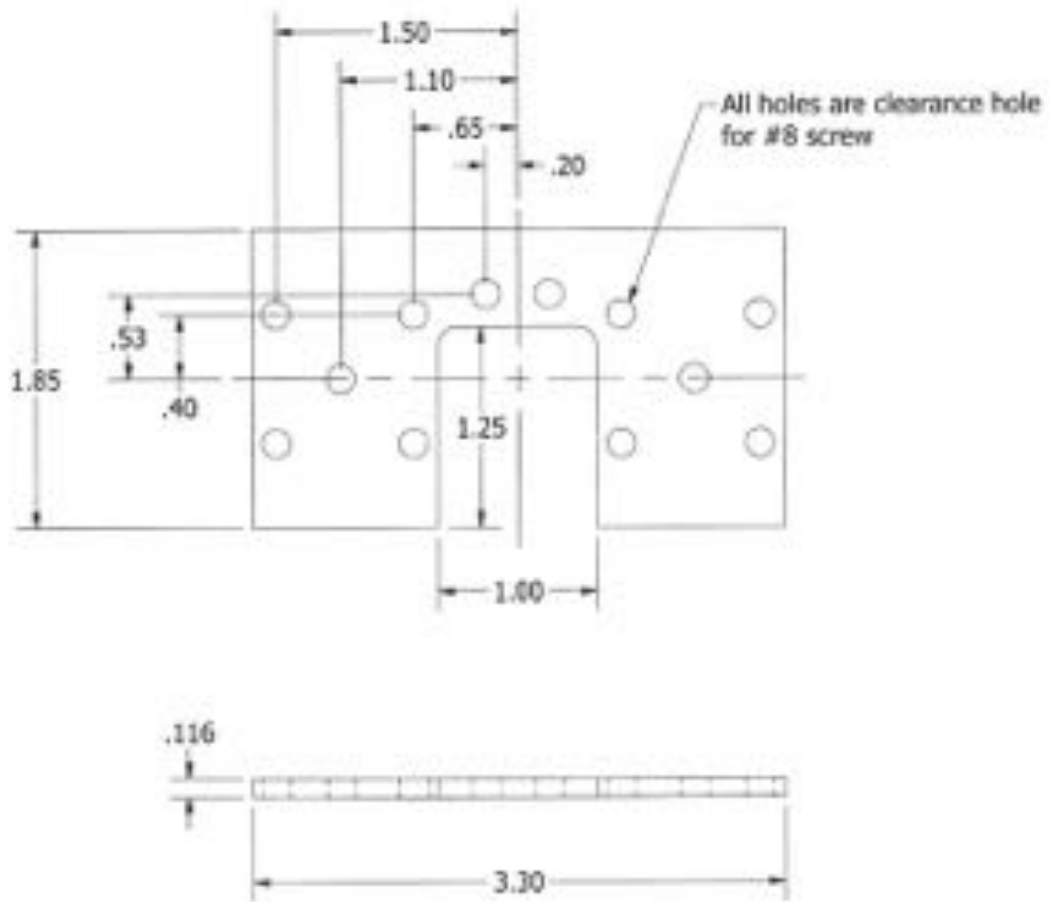


Figure C.5. Single ion trap assembly - sheet 1

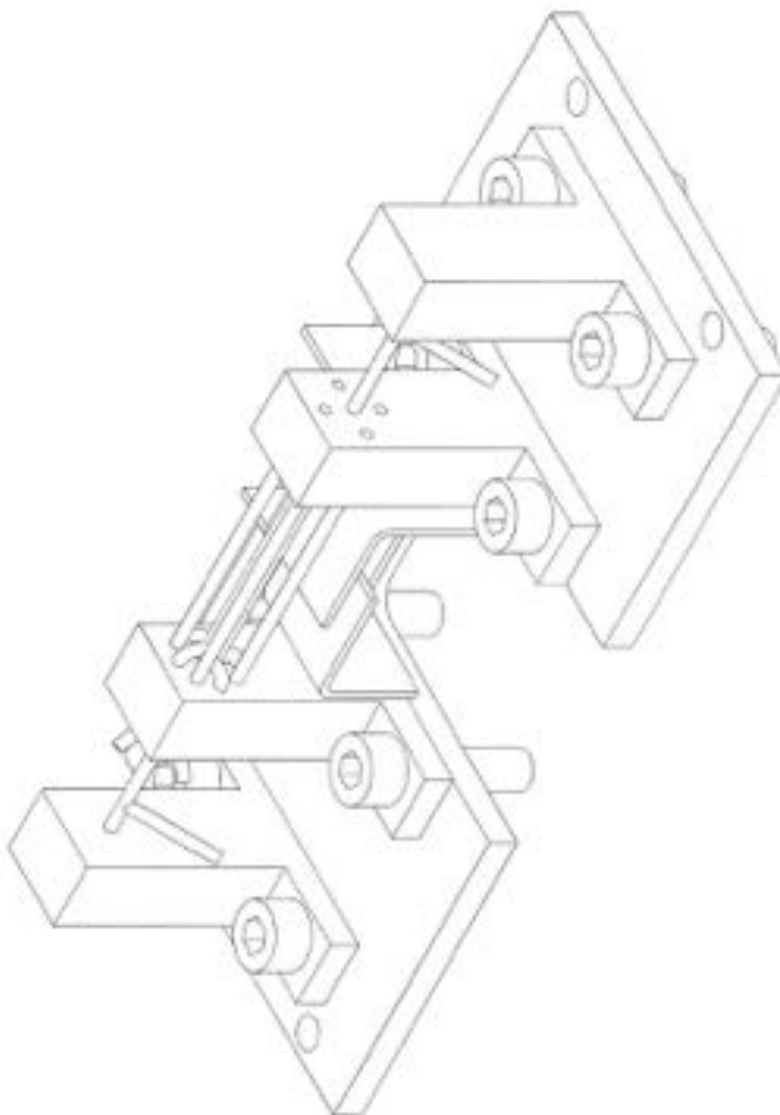


Figure C.6. Single ion trap assembly - sheet 2

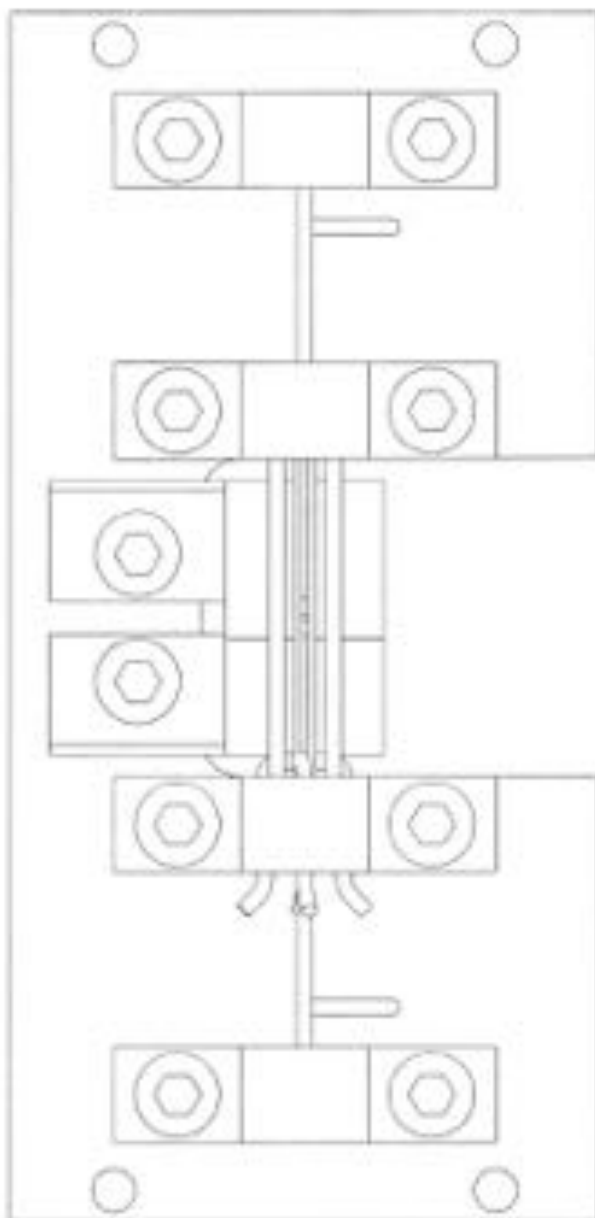


Figure C.7. Single ion trap assembly - sheet 3

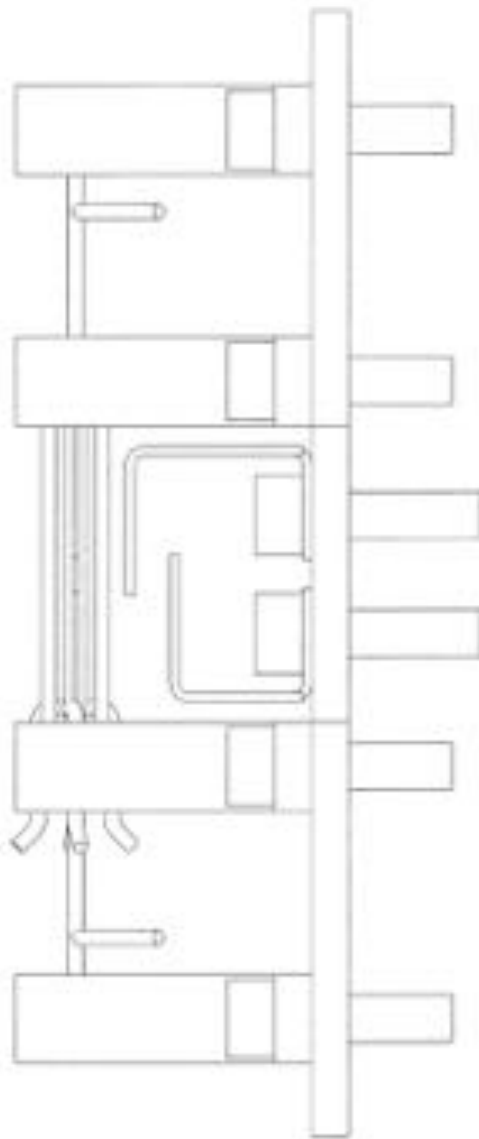


Figure C.8. Single ion trap assembly - sheet 4

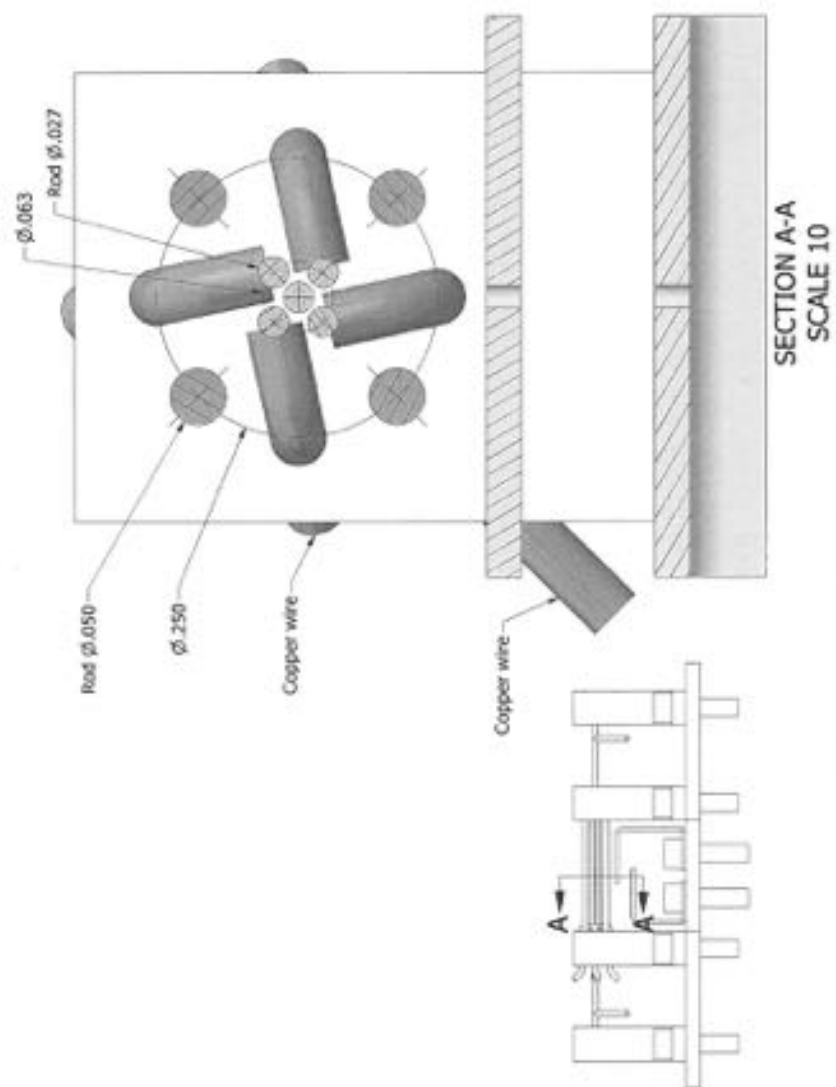


Figure C.9. Trap stand

Units: inches/degree. Tolerance: ± 0.01 ". Material: stainless steel 316

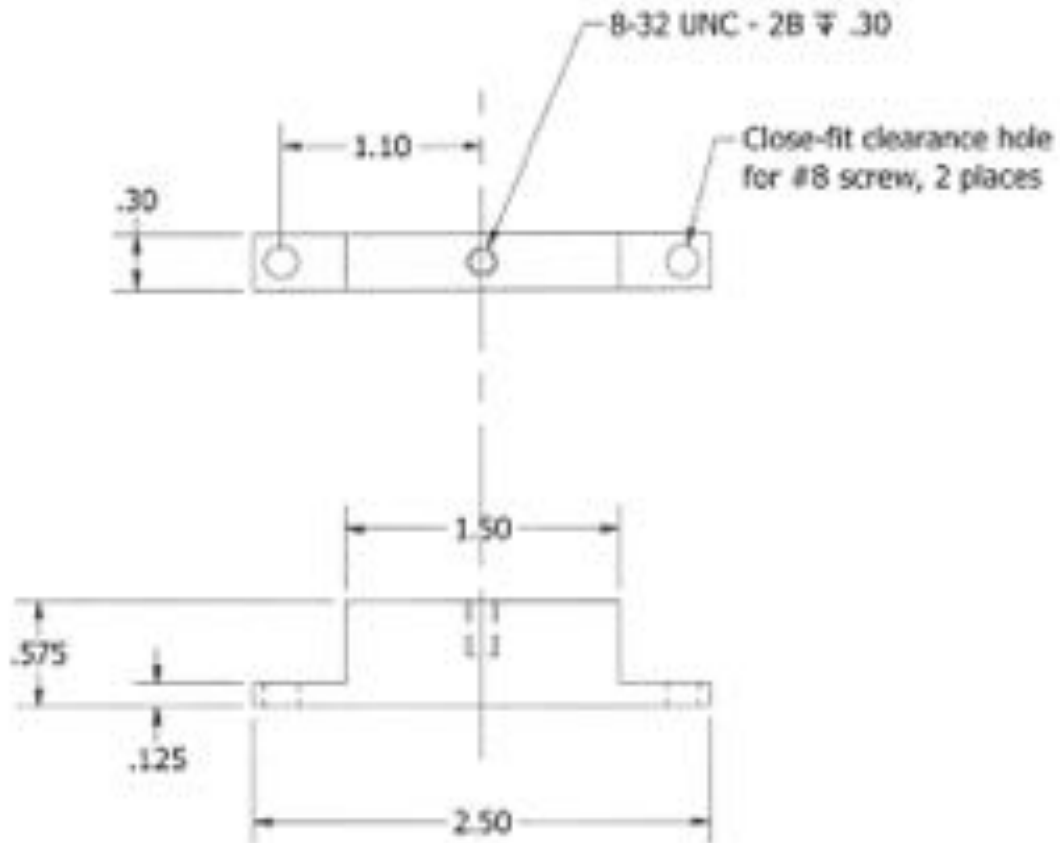


Figure C.10. 6CF flange

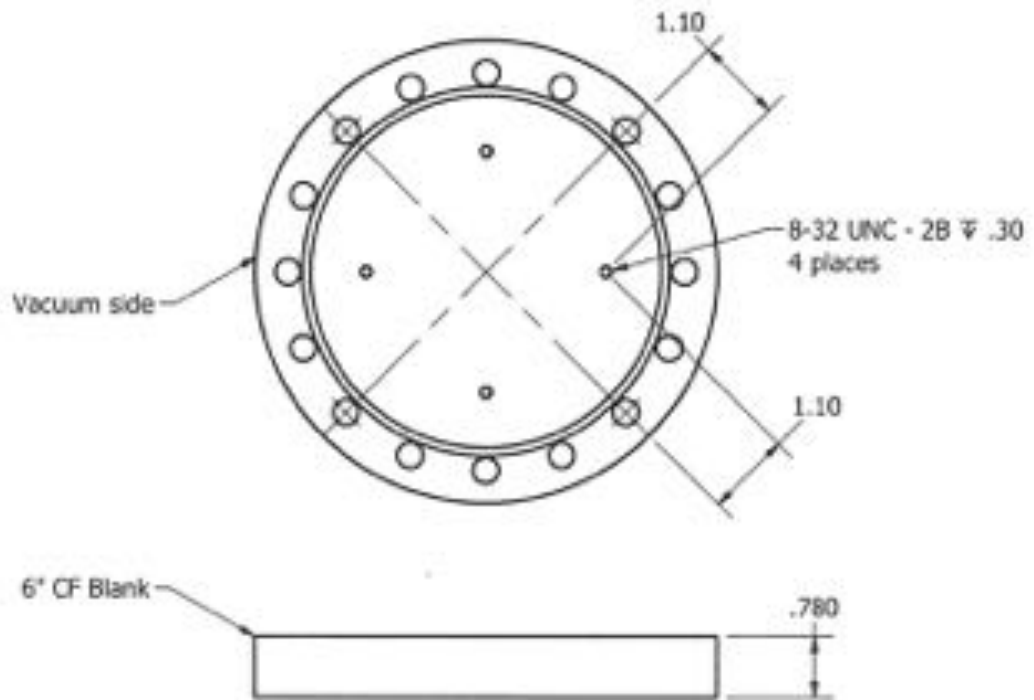


Figure C.11. Doubler - sheet 1

Units: inches/degree. Tolerance: $\pm 0.01''$. Material: aluminum

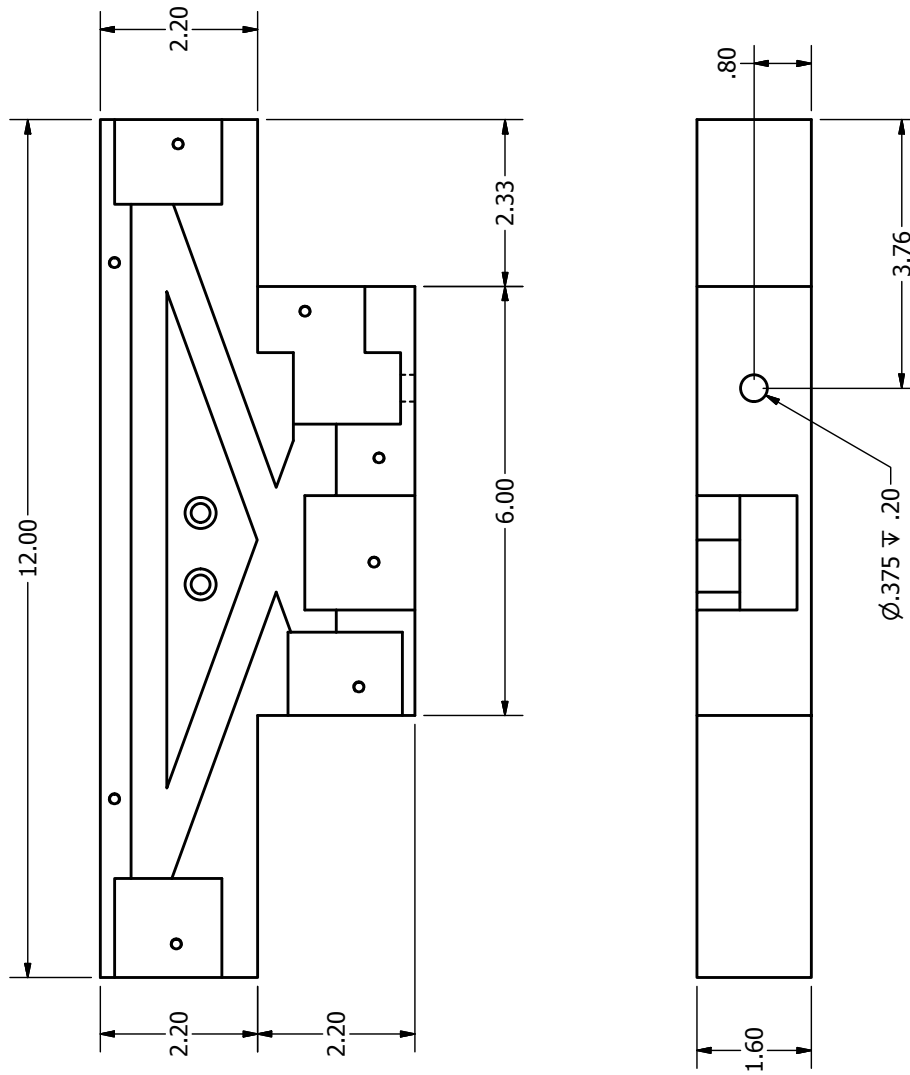


Figure C.13. Doubler - sheet 3

Units: inches/degree. Tolerance: $\pm 0.01''$. Material: aluminum

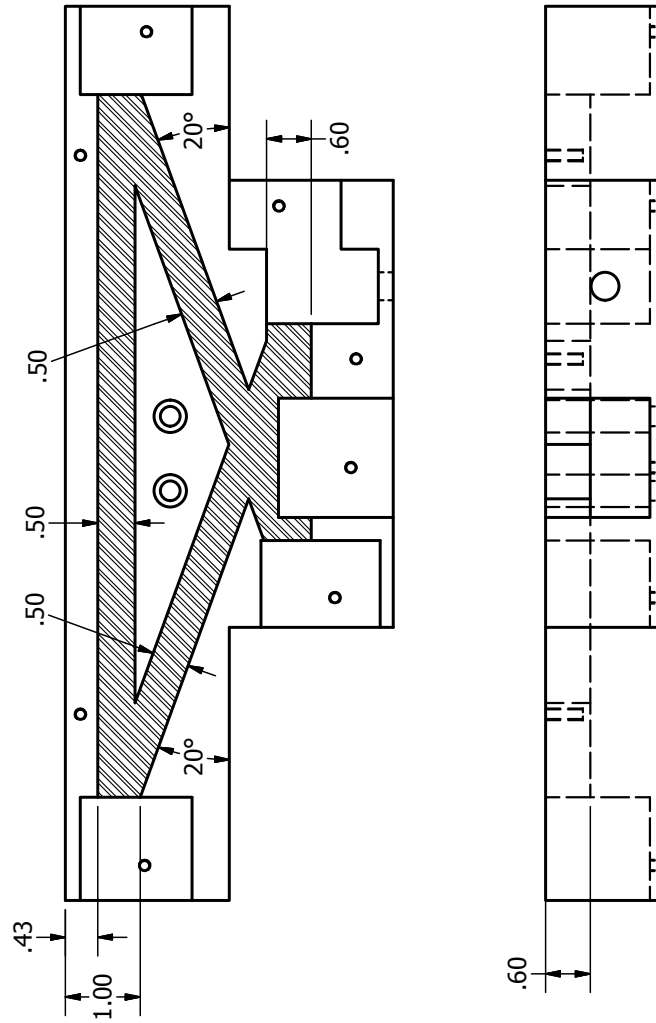
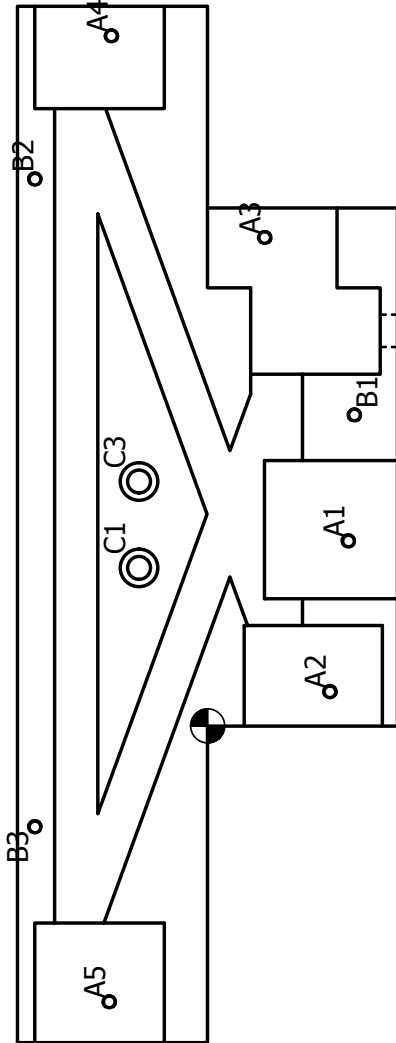


Figure C.14. Doubler - sheet 4

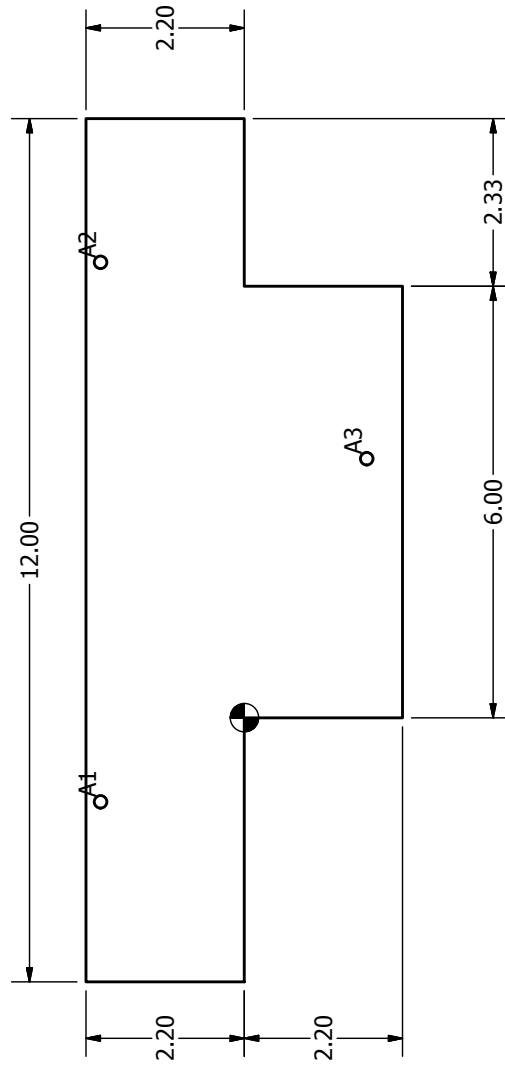
Units: inches/degree. Tolerance: $\pm 0.01''$. Material: aluminum



HOLE TABLE		
HOLE	XDIM	YDIM DESCRIPTION
A1	2.14	-1.63 8-32 UNC - 2B
A2	.40	-1.42 8-32 UNC - 2B
A3	5.65	-.66 8-32 UNC - 2B
A4	7.99	1.11 8-32 UNC - 2B
A5	-3.20	1.14 8-32 UNC - 2B
B1	3.60	-1.70 8-32 UNC - 2B ∇ .50
B3	-1.17	2.00 8-32 UNC - 2B ∇ .50
B2	6.33	2.00 8-32 UNC - 2B ∇ .50
C1	1.83	.79 \varnothing .27 THRU \sqsubset \varnothing .44 ∇ 1.40
C3	2.83	.79 \varnothing .27 THRU \sqsubset \varnothing .44 ∇ 1.40

Figure C.15. Cover for the doubler

Units: inches/degree. Tolerance: $\pm 0.01''$. Material: aluminum



HOLE TABLE			
HOLE	XDIM	YDIM	DESCRIPTION
A1	-1.17	2.00	Ø.18 THRU
A2	6.33	2.00	Ø.18 THRU
A3	3.60	-1.70	Ø.18 THRU

Figure C.16. Crystal holder

Units: inches/degree. Tolerance: $\pm 0.01''$. Material: aluminum

